Surface chemistry of model electrodes under electrocatalytic conditions

Developing Total Reflection X-ray Absorption Spectroscopy for operando studies

Grespi, Andrea

2026

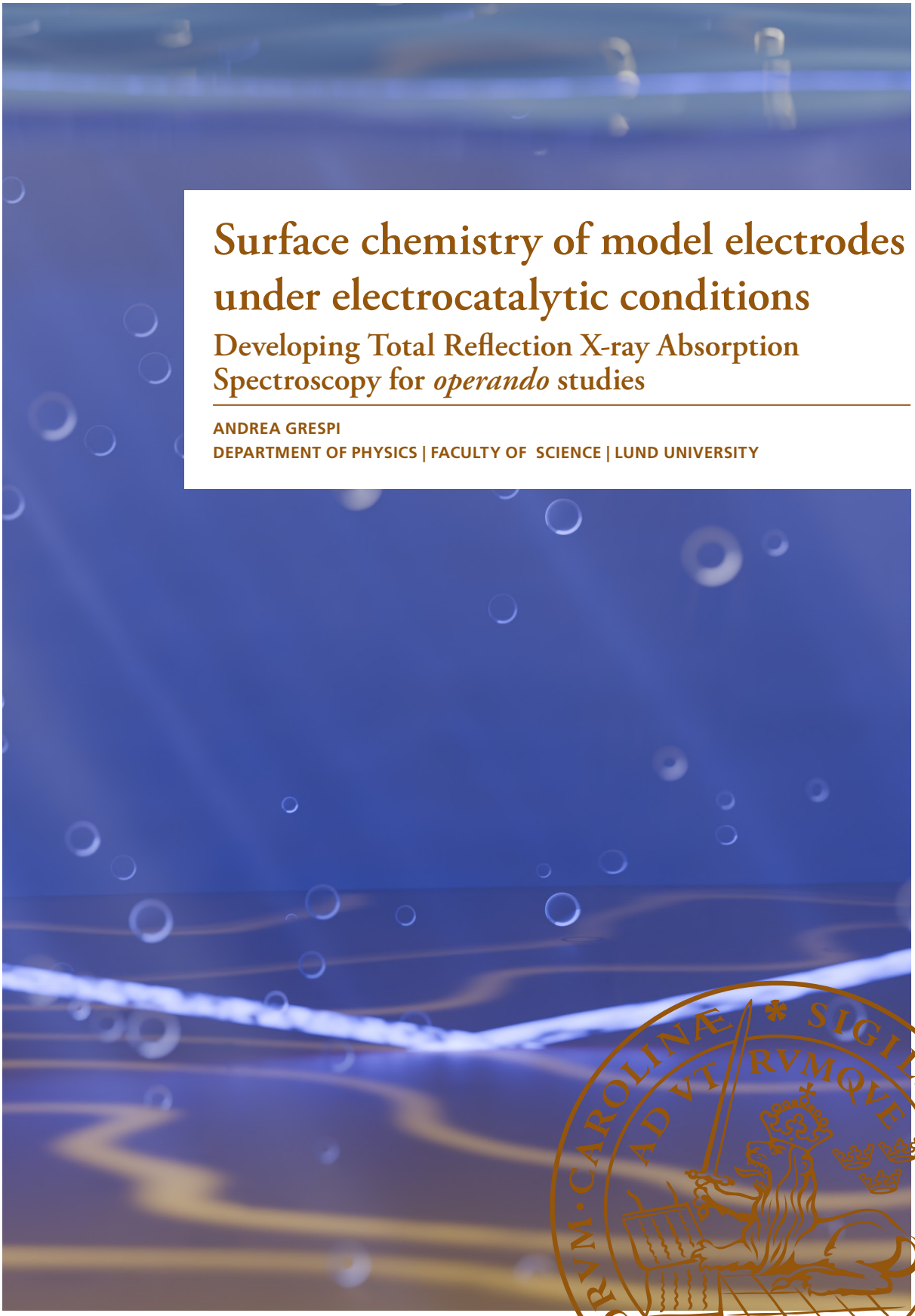

Surface chemistry of model electrodes under electrocatalytic conditions

Developing Total Reflection X-ray Absorption Spectroscopy for *operando* studies

ANDREA GRESPI
DEPARTMENT OF PHYSICS | FACULTY OF SCIENCE | LUND UNIVERSITY

Surface chemistry of model electrodes under electrocatalytic conditions

Developing Total Reflection X-ray Absorption Spectroscopy for *operando* studies

Andrea Grespi

LUND
UNIVERSITY

DOCTORAL DISSERTATION

Doctoral dissertation for the degree of Doctor of Philosophy (PhD)
at the Faculty of Science at Lund University, Sweden, to be publicly defended on the 29th
of May 2026 at 9:15 in the Rydberg Lecture Hall, Department of Physics.

Faculty opponent: Prof. Markus Valtiner, TU Wien

Thesis advisors: Prof. Edvin Lundgren, Dr. Lindsay R. Merte,
Prof. Jinshan Pan, Dr. Filip Lenrick

Organization: LUND UNIVERSITY

Document name: Doctoral Thesis **Date of issue:** 2026-05-05

Author(s): Andrea Grespi

Title and subtitle: Surface chemistry of model electrodes under electrocatalytic conditions: developing Total Reflection X-ray Absorption Spectroscopy for *operando* studies

Abstract:

Electrochemical reactions like water-splitting or corrosion initiate at electrode-electrolyte interface, and in some cases can also be closely linked. In particular, the oxygen evolution reaction (OER) in electrolyzers and the oxygen reduction reaction (ORR) in fuel cells are not only sluggish but can also lead to severe catalyst degradation. A fundamental understanding of these processes is therefore essential for developing more stable and efficient electrocatalysts for green hydrogen technologies. However, probing the structure and chemistry of the electrode surface remains challenging, because these species are ultrathin, amorphous, unstable and buried beneath a thick dense electrolyte.

This thesis applies a range of *ex situ*, *in situ* and *operando* methods based on synchrotron X-rays, electrons and visible light to understand the surface chemistry of gold, platinum and nickel alloy 59 model electrodes under electrocatalytic conditions. Emphasis is placed on developing total reflection X-ray absorption spectroscopy (RefleXAFS) in real operando conditions, which is an underexplored approach. The main model system studied in this thesis is gold, used to compare all the techniques and to understand its stability and surface evolution during OER. Nickel alloy 59, a corrosion-resistant material catalytically active towards OER, serves especially as a secondary model system to validate and further investigate the capabilities of RefleXAFS. Finally, the role of electrochemical oxidation of platinum during ORR is investigated.

Overall, this work shows that ultrathin (hydr)oxide films control the stability and activity of noble metals and corrosion-resistant alloys under electrocatalytic conditions. These findings highlight the link between surface oxidation, electrocatalysis and metal dissolution, and underscore the necessity of operando studies and multimodal approaches to understand electrochemical interfaces.

Key words: surface oxidation, electrocatalysis, corrosion, X-rays, spectroscopy, reflectance, *operando*, *in situ*, electrochemistry.

Language: English

ISBN:

978-91-8104-963-3 (print)

978-91-8104-964-0 (electronic)

Recipient's notes

Signature Date 2026-04-16

Surface chemistry of model electrodes under electrocatalytic conditions

Developing Total Reflection X-ray Absorption Spectroscopy for *operando* studies

Andrea Grespi

LUND
UNIVERSITY

Front cover image by Ulrike Küst (licensed under CC BY 4.0): Cartoon of an X-ray beam reflecting at a shallow incident angle on a golden surface under water.

Back cover image by Andrea Grespi (licensed under CC BY 4.0): 500x500 nm^2 STM image of the Au(111) surface after 5 oxidation-reduction cycles in 0.05 M H_2SO_4.

Published by:

Department of Physics

Faculty of Science

Lund University

Lund, 2026

ISBN 978-91-8104-963-3 (print)

ISBN 978-91-8104-964-0 (electronic)

Printed in Sweden by Media-Tryck, Lund University,
Lund, 2026

Media-Tryck is a Nordic Swan Ecolabel certified provider of printed material. Read more about our environmental work at www.mediatryck.lu.se

MADE IN SWEDEN

Table of Contents

List of publications

The papers included in this thesis are reported below, along with a description of my contributions. For a detailed summary of these papers, please see **Chapter 6**.

I. Probing the electrode-liquid interface using operando total-reflection X-ray absorption spectroscopy

A. Grespi, A. Larsson, G. Abbondanza, J. Eidhagen, D. Gajdek, J. Manidi, A. Tayal, J. Pan, L. R. Merte, E. Lundgren

Surface Science, 748, 122538 (2024)

I took part in planning and performing the experiments, I analyzed the data and wrote the manuscript.

II. Following the electrochemical oxidation of Au(111) in real-time using surface optical reflectance and total-reflection X-ray absorption spectroscopy

A. Grespi, A. Larsson, G. Abbondanza, J. Manidi, J. Eidhagen, E. Lira, A. Ti, M. Ramakrishnan, J. Just, J. Pan, L. R. Merte, E. Lundgren

Journal of The Electrochemical Society, 173, 076502 (2026)

I was the main responsible for planning, leading and performing the experiments. I analyzed the data and wrote the manuscript.

III. A transfer cell for ultra-high vacuum surface analysis of samples exposed to electrochemical environments

E. Lira, **A. Grespi**, N. Paoletti, A. Ti, A. M. Rodriguez, A. Larsson, L. R. Merte, E. Lundgren

Review of Scientific Instruments, 97, 033903 (2026)

I took part in the development of the final setup, planning and performing the experiments, data analysis and writing of the manuscript.

IV. Thickness and chemistry of electrochemically formed oxide films on Au(111) probed with ambient pressure X-ray photoelectron spectroscopy

A. Ti, **A. Grespi**, A. Larsson, U. Küst, N. Paoletti, M. Scardamaglia, A. Shavorskiy, E. Lira, L. R. Merte, E. Lundgren

Submitted

I took part in planning, leading and performing the experiments, the discussion of the data and writing of the manuscript.

V. Surface orientation-dependent electro-oxidation of a polycrystalline gold electrode

A. Ti, H. Sjö, **A. Grespi**, E. Lira, A. Larsson, U. Küst, C. Berschauer, J. Gustafson, L. R. Merte, J. Knudsen, E. Lundgren

Faraday Discussions, in press (2026)

I took part in planning, leading and performing the experiments, discussion of the data and editing of the manuscript.

VI. 2D surface optical reflectance for use in harsh reactive environments

J. Zetterberg, A. Larsson, **A. Grespi**, S. Pfaff, L. Rämisch, L. R. Merte, E. Lundgren

Journal of Physics: Condensed Matter, 37, 133003 (2025)

I measured and analyzed the combined 2D-SOR and RefleXAFS data and contributed to the editing of the manuscript.

VII. An ultrathin hydroxide film governs the stability and reactivity of gold for the oxygen evolution reaction

A. Grespi, A. Larsson, A. Ti, V. Briega-Martos, E. Lira, U. Küst, G. Abbondanza, J. Manidi, S. Cherevko, A. Shavorskiy, M. Scardamaglia, M. Ramakrishnan, J. Just, L. R. Merte, E. Lundgren

Submitted

I was the main responsible for planning, leading and performing the experiments. I analyzed the data and drafted the manuscript. I started and led a collaboration for the dissolution measurements independently.

VIII. Linking surface chemistry and dissolution of Au(111) in H_2SO_4 and NaOH electrolytes: pH and scan rate effects

A. Grespi, A. Larsson, V. Briega-Martos, E. Lira, G. Abbondanza, J. Manidi, M. Ramakrishnan, J. Just, S. Cherevko, L. R. Merte, E. Lundgren

Manuscript

I was the main responsible for planning, leading and performing the synchrotron experiments. I analyzed the data and wrote the manuscript. I started and led a collaboration for the dissolution measurements independently.

IX. The oxygen evolution reaction drives passivity breakdown for Ni-Cr-Mo alloys

A. Larsson, **A. Grespi**, G. Abbondanza, J. Eidhagen, D. Gajdek, K. Simonov, X. Yue, U. Lienert, Z. Hegedüs, A. Jeromin, T. F. Keller, M. Scardamaglia, A. Shavorskiy, L. R. Merte, J. Pan, E. Lundgren

Advanced Materials, 35, 39, 2304621 (2023)

I took part in all the experiments, and I was the main responsible for the XAS measurements. I took part in the analysis of the XAS data and editing of the manuscript.

X. Platinum surface oxides govern the cathodic overpotential of the oxygen reduction reaction

A. Larsson, **A. Grespi**, O. Vodeb, K. van den Akker, A. Ti, C. Berschauer, A. Imre, P. M. Kofoed, E. Lira, M. Ramakrishnan, S. Ansell, J. Just, H. Grönbeck, U. Diebold, E. Lundgren, L. R. Merte, D. Strmcnik, R. Mom, M. Koper

EES Catalysis, in press (2026)

I took part in the synchrotron measurements, discussion of the data and editing of the manuscript.

Papers to which I have contributed but not included in this thesis.

XI. Passive film evolution on Ni-Cr-Mo alloys in acidic chloride solution during anodic polarization

J. Eidhagen, M. Hättestrand, U. Kivisäkk, J. Andersson, L. Lautrup, X. Yue, A. Larsson, **A. Grespi**, M. Scardamaglia, A. Shavorskiy, E. Lundgren, J. Pan

Corrosion Communications, 21, 14-25 (2026)

XII. Transpassive-repassivation process of Ni-base superalloys: The role of hidden subsurface alloy layer

X. Yue, A. Larsson, D. Chen, **A. Grespi**, G. Abbondanza, U. Lienert, Z. Hegedüs, A. Jeromin, T. F. Keller, M. Scardamaglia, A. Shavorskiy, C. Dong, E. Lundgren, J. Pan

Corrosion Science, 257, 113321 (2025)

XIII. In Situ Grazing Incidence X-ray Total Scattering Reveals the Effect of the "Two-Step" Method for the Anodization of Aluminum Surfaces

N. P. L. Magnard, G. Abbondanza, L. S. Junkers, L. Glatthaar, **A. Grespi**, A. Spriewald-Luciano, F. Igoa Saldaña, A.C. Dippel, N. Vinogradov, H. Over, K. M. Ø. Jensen, E. Lundgren

ACS Appl. Mater. Interfaces, 17, 33, 46887–46898 (2025)

XIV. Self-Stabilized Heterometallic Pair Sites for Selective Ethanol Dehydrogenation on Pt–Cr–Ag Alloy Catalysts

J. F. Weaver, S. Xiang, J. Jamir, U. Küst, L. Rämisch, **A. Grespi**, H. Wallander, J. Zetterberg, S. Arias, E. L. Fornero, P. K. Routh, S. Zhang, J. S. Miller, R. K. Rai, E. A. Stach, J. A. Boscoboinik, M. M. Montemore, E. C. H. Sykes, J. Knudsen, J. Biener, L. R. Merte, A. I. Frenkel

Angew. Chem. Int. Ed., e202513844 (2025)

XV. Au–Pd Barcode Nanowires with Tailored Lattice Parameters and Segment Lengths for Catalytic Applications

G. Abbondanza, **A. Grespi**, A. Larsson, C. Hetherington, M. Snelgrove, F. Carlá, N. Vinogradov, R. Felici, E. Lundgren

ACS Appl. Nano Mater., 7, 4, 3861–3872 (2024)

XVI. Dynamics of early-stage oxide formation on a Ni-Cr-Mo alloy

A. Larsson, S. Gericke, **A. Grespi**, V. Koller, J. Eidhagen, X. Yue, E. Frampton, S. Appelfeller, A. Generalov, A. Preobrajenski, J. Pan, H. Over, E. Lundgren

npj Materials Degradation, 8, 39 (2024)

XVII. Anisotropic strain variations during the confined growth of Au nanowires

G. Abbondanza, **A. Grespi**, A. Larsson, L. Glatthaar, T. Weber, M. Blankenburg, Z. Hegedüs, U. Lienert, H. Over, E. Lundgren

Applied Physics Letters, 122, 123101 (2023)

XVIII. Hydride formation and dynamic phase changes during template-assisted Pd electrodeposition

G. Abbondanza, **A. Grespi**, A. Larsson, D. Dzhigaev, L. Glatthaar, T. Weber, M. Blankenburg, Z. Hegedüs, U. Lienert, H. Over, G. S. Harlow, E. Lundgren

Nanotechnology, 34, 505605 (2023)

XIX. Synchrotron-based near ambient-pressure X-ray photoelectron spectroscopy and electrochemical studies of passivation behavior of N- and V-containing martensitic stainless steel

X. Yue, A. Larsson, H. Tang, **A. Grespi**, M. Scardamaglia, A. Shavorskiy, A. Krishnan, E. Lundgren, J. Pan

Corrosion Science, 214, 111018 (2023)

XX. In situ quantitative analysis of electrochemical oxide film development on metal surfaces using ambient pressure X-ray photoelectron spectroscopy: Industrial alloys

A. Larsson, K. Simonov, J. Eidhagen, **A. Grespi**, X. Yue, H. Tang, A. Delblanc, M. Scardamaglia, A. Shavorskiy, J. Pan, E. Lundgren.

Applied Surface Science, 611, A, 155714 (2023)

Abstract

Electrochemical reactions like water-splitting or corrosion initiate at electrode-electrolyte interface, and in some cases can also be closely linked. In particular, the oxygen evolution reaction (OER) in electrolyzers and the oxygen reduction reaction (ORR) in fuel cells are not only sluggish but can also lead to severe catalyst degradation. A fundamental understanding of these processes is therefore essential for developing more stable and efficient electrocatalysts for green hydrogen technologies. However, probing the structure and chemistry of the electrode surface remains challenging, because these species are ultrathin, amorphous, unstable and buried beneath a thick dense electrolyte.

This thesis applies a range of *ex situ*, *in situ* and *operando* methods based on synchrotron X-rays, electrons and visible light to understand the surface chemistry of gold, platinum and nickel alloy 59 model electrodes under electrocatalytic conditions. Emphasis is placed on developing total reflection X-ray absorption spectroscopy (RefleXAFS) in real *operando* conditions, which is an underexplored approach. The main model system studied in this thesis is gold, used to compare all the techniques and to understand its stability and surface evolution during OER. Nickel alloy 59, a corrosion-resistant material catalytically active towards OER, serves especially as a secondary model system to validate and further investigate the capabilities of RefleXAFS. Finally, the role of electrochemical oxidation of platinum during ORR is investigated.

Overall, this work shows that ultrathin (hydr)oxide films control the stability and activity of noble metals and corrosion-resistant alloys under electrocatalytic conditions. These findings highlight the link between surface oxidation, electrocatalysis and metal dissolution, and underscore the necessity of *operando* studies and multimodal approaches to understand electrochemical interfaces.

Popular summary

This thesis focuses on developing and using characterization methods, to understand the behavior of materials during the electrochemical reactions involved in electrolyzers, fuel cells and corrosion.

Electrochemistry studies chemical reactions where electrons move and generate electricity, or *vice versa* where electricity causes a chemical reaction. Technologies like batteries and phenomena like corrosion rely on these processes, and understanding how they work at the atomic scale can help to design better devices and materials for future technologies. For example, significant efforts are currently underway to develop more efficient electrolyzers and fuel cells for green hydrogen production and usage, which could help replace fossil-fuel-based energy. Electrolyzers can use electricity from renewable sources to split water into oxygen and hydrogen, whilst fuel cells can use hydrogen and oxygen to generate electricity and water when the wind is not blowing and the sun is not shining. These reactions, which can also involve corrosion phenomena, take place at the interface between a catalytic material, called electrocatalysts, and a liquid, mostly made of water, called electrolyte.

To understand what is happening at the interface between the electrocatalyst and the electrolyte, it is necessary to use characterization techniques that can probe the interfacial atoms while the reaction is happening, which is not trivial. Synchrotron radiation facilities, like MAX IV at Lund (Sweden), can generate an extremely intense X-ray beam that can penetrate through gases, liquids and solids, carrying information about their atomic structure and chemistry. Using dedicated experimental setups and configurations, X-rays can be focused on the surface of a material while it is splitting water, corroding, etc., revealing details of the electrochemical reaction and the material's properties. In this context, the main technique used in this thesis is “RefleXAFS”, an approach originally developed in the 1980s that, however, has so far remained underexplored for this type of application. Recent advances in synchrotron radiation sources and instrumentation, and in electrochemical methodologies have opened new opportunities to fully exploit the potential of RefleXAFS, as explored in this thesis (**Papers I, II, VII, VIII, and X**). Additionally, complementary surface characterization techniques, including 2D-SOR (**Papers II, V, and VI**), AP-XPS (**Papers IV, VII, and IX**), STM (**Papers III and VII**), and SXRD (**Paper V**), were used.

Besides the development of surface characterization methods, this thesis aims to improve our fundamental understanding of the electrochemical behavior of gold (**Papers I-VIII**), nickel alloy 59 (**Papers I and IX**), and platinum (**Paper X**). Across these studies, a consistent picture emerges: a few atomic layers of oxide or hydroxide form at the surface of these materials and play a decisive role in governing their catalytic activity and stability.

Sommario divulgativo

Questa tesi si concentra sullo sviluppo e sull'utilizzo di metodi di caratterizzazione per studiare il comportamento dei materiali durante le reazioni elettrochimiche coinvolte in elettrolizzatori, celle a combustibile e nei processi di corrosione.

L'elettrochimica studia reazioni chimiche in cui gli elettroni si muovono generando elettricità oppure, viceversa, in cui l'elettricità induce una reazione chimica. Tecnologie come le batterie e fenomeni come la corrosione si basano su questi processi, e comprenderne il meccanismo a livello atomico può contribuire alla progettazione di dispositivi e materiali piu efficienti e performanti. Ad esempio, attualmente molta ricerca è incentrata sullo sviluppo di elettrolizzatori e celle a combustibile più efficienti per la produzione e l'utilizzo di idrogeno verde, come alternativa ai combustibili fossili. Gli elettrolizzatori possono utilizzare elettricità da fonti rinnovabili per scindere l'acqua in ossigeno e idrogeno, mentre le celle a combustibile possono riconvertire idrogeno e ossigeno in elettricità e acqua quando l'energia rinnovabile non é momentaneamente disponibile. Queste reazioni, che possono anche coinvolgere fenomeni di corrosione, avvengono al confine (interfaccia) tra un materiale catalitico, chiamato elettrocatalizzatore, e un liquido, per lo più costituito da acqua, chiamato elettrolita.

Per comprendere cosa accade a livello atomico, servono tecniche di caratterizzazione in grado di sondare gli atomi presenti all'interfaccia mentre la reazione è in corso. Le sorgenti di radiazione di sincrotrone, come MAX IV a Lund (Svezia), generano raggi-X estremamente intensi, capaci di penetrare gas, liquidi e solidi, trasportando informazioni sulla loro struttura atomica e chimica. Utilizzando apparati sperimentali dedicati, i raggi X possono essere focalizzati sulla superficie di un materiale mentre esso scinde l'acqua, si corrode, ecc., rivelando dettagli sulla reazione elettrochimica e sulle proprietà del materiale. In questo contesto, la tecnica di caratterizzazione principale di questa tesi si chiama "RefleXAFS", un approccio sviluppato originariamente negli anni '80 ma finora poco esplorato per questo tipo di applicazioni. I recenti progressi tecnologici per la radiazione di sincrotrone e nelle metodologie elettrochimiche hanno aperto nuove opportunità per sfruttarne appieno il potenziale, come esplorato in questa tesi (**Articoli I, II, VII, VIII e X**). Inoltre, sono state utilizzate tecniche di caratterizzazione superficiale complementari, tra cui 2D-SOR (**Articoli II, V e VI**), AP-XPS (**Articoli IV, VII e IX**), STM (**Articoli III e VII**) e SXRD (**Articolo V**).

Oltre allo sviluppo di metodi di caratterizzazione, questa tesi mira a migliorare la nostra comprensione su scala atomica del comportamento elettrochimico dell'oro (**Articoli I-VIII**), della lega nichel 59 (**Articoli I e IX**) e del platino (**Articolo X**). Da questi studi emerge un quadro coerente: pochi strati atomici di ossido o idrossido si formano sulla superficie di questi materiali e svolgono un ruolo determinante nel governarne l'attività catalitica e la stabilità.

Acknowledgements

If I am here today, as a scientist and as a person, it is thanks to all the people and experiences that shaped me and brought me to write this thesis. In principle, I should acknowledge an almost infinite number of contributors, perhaps the entire universe that conspired to bring me to this moment. So, if you are reading this, whoever you are, thank you! I will now do my best to acknowledge those who have directly contributed to this journey.

First of all, I am thankful to my main supervisor and mentor, **Edvin Lundgren**, who taught me a lot of things about science, research and academia, and who showed me what it means to be a great leader. Thanks for always being present and for creating such a pleasant working environment, where I never felt alone. Thanks for the freedom you gave me to try and explore, to take the initiative and the responsibilities, to fail and succeed, while always being there behind the scenes, keeping an eye on the bigger picture and guiding me back on track when needed. Under your care, positivity, and creativity, I really had the chance to do my best and grow from all the opportunities you provided. Thanks for all the fun, experiments, discussions, conferences all around the world, dinners, beers, deadlines, and endless support.

I am so lucky to say that there is another very important supervisor that I would like to acknowledge, **Lindsay Merte**, who believed in my capabilities well before I did. This journey really started during my master's thesis in your lab, where I got enthusiastic about Surface Science and gained some confidence as a scientist. Thanks for always being up to discuss and answering all my questions with patience and passion. Somehow, you always get what I am asking, even when the question is unclear. Thanks for everything you taught me, your mentorship and supervision, for your very honest comments, your attention to details, your hard work, and all the fun we had during experiments, conferences, BBQs, beers and dinners.

I would also like to acknowledge the support from my co-supervisor, **Jinshan Pan**, especially at the beginning of my PhD when we had several beamtimes together. During one of those early days, you reminded me that if something was easy, someone else would have already done it. Sometimes that is a very good reminder! Thanks for the contagious passion and motivation you showed during the experiments, and for teaching me about electrochemistry and corrosion in your lectures and on several occasions during beamtimes or dinners.

Finally, my co-supervisor **Filip Lenrick**, although we have not done much together, thanks for always being nice to me and for the occasional chats we had. You deserve a special shout-out for taking great photos!

The round of supervisors is finished, but there is still a long list to go through… I will start with **Alfred Larsson**, an outstanding colleague and friend, a brother,

sometimes even an extra supervisor. I feel so lucky to have found all this on my first day of PhD. You have always been ready to motivate me, to listen to me, and to discuss experiments, results, papers, and more. Thanks for all we shared, for the fun we had during travels, conferences, BBQs, hiking, climbing, parties, etc. and for all the chats we had about science and life, I really felt understood and I learned a lot. My PhD would have been much less fun and much more difficult without all this.

Giuseppe Abbondanza, an amazing colleague and friend, who was often my Italian reference and InfoPoint in Lund when I started. I was asking you countless questions at the beginning of my PhD, especially since it started with a two-weeks night shift with you in Hamburg. Thanks for always trying to answer my questions, for motivating me, for believing in my ideas, and for the laughs we have had since then. Also, thanks to both you and **Monica** for all the fun during vacations, BBQs, dinners, beers and hikes!

Estephania Lira, thank you for your hard work, patience, and support, especially in the UHV lab and STM. Working together every day, all day, for weeks, was for sure intense sometimes, but all the laughs, chatting, and genuine moments we shared made me feel at home. Thanks also for all the fun during lunch, BBQs, parties and afterworks!

Auden Ti, thanks for bringing a very positive and chill vibe to the group! We learned a lot together, and your Python and IT skills were really helpful throughout my PhD. Thanks for the hard work with the XPS analysis and all the experiments, for the laughs and chats in the office, at lunch, in the lab, and for all the fun we had during travels, beers, and parties.

Thanks to **Ulrike Küst** and **Hanna Sjö** for the hard work during beamtimes, for all the fun we had during game nights, travels, dinners, and beers, and for the support you gave me throughout the PhD. It was great to share these years with you. From you, I learned more than "just" XPS and XRD; I learned something about discipline, the importance of rules, values, and punctuality…! Thanks also to the latest member, **Claire Berschauer**, a fresh, sharp, and creative mind joining the group! Thanks for the fun and for helping over the last year of my PhD.

Jacopo Manidi, a great friend from my bachelor's and master's studies, I am so happy that you joined my beamtimes and contributed to this thesis. Those days are memorable, and we got the most important results of my PhD. Thanks for putting all your heart into everything you do and for helping and supporting me since the day we met.

Thanks a lot to all the beamline scientists at MAX IV and PETRA III for the outstanding work and dedication put into each synchrotron experiment. Special thanks go to **Justus Just** and **Mahesh Ramakrishnan**, from Balder, who did an amazing job setting up the beamline and supporting several experiments.

Niccoló Paoletti, it was great to have you in Lund for your thesis! Siiiiiiiuuuuuuuu!!

Josefin Eidhagen, from KTH and Alleima AB, thanks for the hard work during beamtimes, for showing us the company, and for polishing the samples to perfection!

Serhiy Cherevko and **Valentín Briega Martos**, from FAU, Erlangen-Nürnberg, thanks for the fruitful collaboration! It was a pleasure.

Harald, **Dora**, **Andrea**, **Miguel**, from Malmö, thanks for the nice discussion, chats, and hard work during the experiments!

SLJUS always felt like home because of all the amazing people I met at the division and nearby during these years. I am thankful to **Jan Knudsen** and **Johan Gustafson**, for teaching me about Surface Science, XRD, XPS, for the fun and the nice chats, and for being very athletic…! Thanks also to all the other professors I met during these years at Lund! **Rainer**, **Anders**, **Jesper**, **Pablo**, **Matias** (who is TOO athletic!), **Mathieu**, **Elizabeth**, **Joachim**, **Stacey**, **Rasmus**, **Ian**, **Sara**, **Johan Z.**, and many more. Thanks to **Patrik,** for his jokes and the nice chats, and together with **Anne** and **Josefine**, for the great help with the administrative work. Thanks to all the amazing students and postdocs, **Rohit**, **Hari**, **Nishant**, **Ahmed**, **Nelia**, **Emilia**, **Vidar**, **Julia**, **Ajsa**, **Eleni**, **Zephyr**, **Oskar**, **Thomas**, **Mehran**, **Ata**, **Hajar**, **Chris, Gustavo, Huaiyu, Giulio, Stefano, Yen-Po, Ekaterina**, **Klara**, **Megan, Filip, Lisa, Sabrina, Sebastian, Alexandra**, **Nicola**, **Audunn**, **Dima**, **Rosie, Max**, **Sina**, and many others. Special thanks to my office mate, **Zisheng**, for sharing this journey with me every day, or at least when we were not away for beamtime.

Thanks to **Martino**, **Gigi, Fabio**, and the rest of the party team for not making me miss home with all the fun we had in Lund, Malmö, and Copenhagen. “Daje Forte, sempre!” cit.

Thanks to all the amazing friends I have back home from Opera and Milano, **Willy**, **Raffa**, **Penna**, **Tia**, **Clod**, **Ale**, **Dave**, **Albo**, **Frenk**, **Fra**, **Alice**, **Fabi**, **Gilly**, **Laura**, **Caro**, **Sare**, **Nico**, **Beppe**, **Sammi**, **Giamma**, **Fajo**, **Lenny**, **Capo**, **Nik**, **Mery**, **Zaffa**, **Ciotti**, and many others. Maintaining all these friendships when leaving abroad is not easy, but somehow, when I meet you, it still feels like home.

Finally, it is time to acknowledge the most important people in my life. **Mamma** and **Papá**, thank you for giving me the freedom and the opportunity to fly away to discover my own path. Thanks for all your endless efforts, support, and unconditional love, which are my strength and motivation. To my extended family, **Nonno**, **Nonna**, **Zia, Zio**, and my cousin **Fabio**, thanks for your genuine love and for believing in my capabilities since I was a kid. To **Martina**, who makes me feel like a better person since the day we met, thanks for your support, kindness, respect, and love.

Take care,
Andrea.

List of abbreviations

OER	Oxygen Evolution Reaction
ORR	Oxygen Reduction Reaction
RefleXAFS	Total Reflection X-ray Absorption Spectroscopy
UHV	Ultra-High Vacuum
EC-STM	Electrochemical Scanning Tunneling Microscopy
SXRD	Surface X-ray Diffraction
3D	Three-Dimensional
sc	Simple Cubic
bcc	Body Centered Cubic
fcc	Face Centered Cubic
2D	Two-Dimensional
hcp	Hexagonal Closed Packed
STM	Scanning Tunneling Microscopy
E-field	Electric Field
DFT	Density Functional Theory
HER	Hydrogen Evolution Reaction
WE	Working Electrode
CE	Counter Electrode
LUMO	Lowest Unoccupied Molecular Orbital
HOMO	Highest Occupied Molecular Orbital
OCP	Open Circuit Potential
redox	Reduction-oxidation
EDL	Electrical Double Layer
IHP	Inner Helmholtz Plane
OHP	Outer Helmholtz Plane
PZC	Potential of Zero Charge
RE	Reference Electrode
RHE	Reversible Hydrogen Electrode

SHE	Standard Hydrogen Electrode
PEEK	Polyetheretherketone
2D-SOR	Two-Dimensional Surface Optical Reflectance
AP-XPS	Ambient Pressure X-ray Photoelectron Spectroscopy
CA	Chronoamperometry
LSV	Linear Sweep Voltammetry
CV	Cyclic Voltammetry
UPL	Upper Potential Limit
PDM	Point Defect Model
DLSR	Diffraction-Limited Storage Ring
XAS	X-ray Absorption Spectroscopy
XAFS	X-ray Absorption Fine Structure
XANES	X-ray Absorption Near Edge Structure
EXAFS	Extended X-ray Absorption Fine Structure
XRF	X-ray Fluorescence
GI	Grazing Incidence
SEM	Scanning Electron Microscopy
XPS	X-ray Photoelectron Spectroscopy
AES	Auger Electron Spectroscopy
LEED	Low Energy Electron Diffraction
BE	Binding Energy
PE	Photon Energy
IMFP	Inelastic Mean Free Path
XRD	X-ray Diffraction
CTR	Crystal Truncation Rod
SLR	Superlattice Rod
TSXRD	Tomographic Surface X-ray Diffraction

1. Introduction

1.1 Motivation and background

For the past two centuries, electrochemistry has played an important role in the scientific and technological advancement of our society. From batteries to corrosion-resistant materials, electrochemical processes span a large range of applications that power, protect, and sustain our everyday life[1]. Nowadays, many technologies focused on reducing greenhouse gas emissions are based on electrochemistry, e.g. batteries, green hydrogen production, direct air capture technologies, etc.[2,3] Green hydrogen production is related to this thesis and can be achieved *via* electrolyzers that split water electrochemically using electrical energy from renewable sources such as wind or solar power. This approach can be used to cope with the natural fluctuations in renewable sources by converting electrical energy into chemical energy, stored in hydrogen bonds[4]. When needed, this chemical energy can be exploited using fuel cells, which operate on the opposite process: hydrogen is recombined with oxygen, releasing electrical energy and water as the only by-product[5]. However, there are still many issues limiting the efficiency and the spread of these technologies. A crucial factor is the choice of electrocatalyst materials, i.e. the active material that enables these reactions[3,4,6]. Currently, expensive noble metals such as Pt, Ru, and Ir are commonly used in many electrocatalysts for electrolyzer and fuel cell applications due to their high activity and stability under these conditions[4,5,7]. However, even noble metals are not entirely inert in these harsh environments, measurements suggest that oxidation and dissolution can take place and drastically reduce their lifetime and performance[8–12]. The current lack of fundamental understanding of these phenomena hampers the development of more robust electrocatalysts and electrochemical devices[3,13]. Part of this thesis aims to contribute to this understanding, providing insights into the electrochemical behavior of model electrocatalysts at the atomic scale.

The key processes described above occur at buried, electrified interfaces between solid electrodes and water-based electrolytes, where chemical and structural changes occur[14–16]. The nature of these interfacial transformations are not directly revealed by electrochemical measurements and detecting them *ex situ* raises fundamental questions about whether the observed chemistry and structure truly reflect the state of the electrified interface under operating conditions[17,18]. Hence, *in situ* and *operando* surface-sensitive studies, complemented by electrochemical

measurements, are indispensable for revealing the behavior of such complex interfaces at the atomic scale. However, this is not trivial to achieve. Traditional Ultra-High Vacuum (UHV, < 10^{-6} mbar) techniques can provide atomic-scale surface sensitivity, through the detection of electrons, but the instability of the electrolyte in UHV limits these studies to *ex situ* conditions[17,18]. On the other hand, if the electrolyte can be kept stable in UHV, it would hinder the detection of electrons due to high attenuation of the signal. An ideal characterization technique for electrochemical systems should provide comparable surface sensitivity to UHV electron-based methods, yet without signal attenuation from the electrolyte. Synchrotron X-rays are one of the best candidates for this purpose, thanks to their high penetration power, tunable wavelengths and beam focus[17,18]. This applies especially to grazing-incidence photon-in/photon-out techniques based on hard X-rays (~10-100 keV), since the penetration power of photons is much higher than that of electrons and increases with photon energy, while a grazing-incidence geometry enables surface sensitivity[19]. Another essential requirement in surface science to establish structure-performance relationships of electrocatalysts is to use well-defined model systems such as single-crystals and planar surfaces[15,20,21]. Lack of clarity can arise from poorly defined electrode materials, e.g. nanoparticles on carbon substrates or porous electrodes, which are typically used in electrocatalysis. There are not many surface-sensitive techniques that can work under true *operando* conditions using well-defined model systems, the most common are electrochemical scanning tunneling microscopy (EC-STM)[22] and surface X-ray diffraction (SXRD)[18]. Although these techniques provide very useful insights on the structural evolution of the electrode/electrolyte interface, less information can be obtained from disordered phases, which are commonly formed at the electrode surface. In this context, total reflection X-ray absorption spectroscopy (RefleXAFS) is a powerful complementary approach[23–26]. First developed in the 1980s[27,28], this technique remains underexplored for *operando* studies on electrochemical systems[29]. By measuring the totally reflected X-ray intensity as a function of incident photon energy, surface-sensitive X-ray Absorption Spectra can be obtained to monitor both chemical and structural changes at the electrode surface, independent of its crystallinity. Over the past decade, the emergence of 4th generation synchrotron light sources[30], together with advances in beamline instrumentation and experimental methodologies[17,19,20,31], has opened new opportunities for RefleXAFS studies to investigate electrochemical interfaces under real *operando* conditions. Developing methods like RefleXAFS to reveal the chemistry and structure of the electrode-electrolyte interface while the reaction is happening is the key to understand the mechanisms that govern the electrochemical performance of electrocatalysts. Hence, addressing this need is the main motivation of this thesis.

1.2 This thesis

The focus of this thesis can be divided into two connected themes: I) the development of *operando* RefleXAFS to investigate the electrode-electrolyte interface. II) The application of RefleXAFS and complementary techniques to characterize model electrodes in electrocatalytic environments, with a particular emphasis on the electrochemical oxidation of single- and poly-crystalline gold electrodes during the oxygen evolution reaction (OER), i.e. the main reaction limiting the efficiency of electrolyzers. Additionally, this thesis addresses the behavior of polycrystalline nickel alloy 59 during OER and of polycrystalline platinum during the oxygen reduction reaction (ORR), i.e. the main reaction limiting the efficiency of fuel cells. Since the OER is shown to involve electrocatalyst degradation in a manner similar to corrosion, and since nickel alloy 59 is a corrosion-resistant material, some of these findings are also linked to corrosion science. **Chapter 2** provides a brief introduction to the fundamentals of materials science and surface science. **Chapter 3** provides the basic concepts of electrochemistry, with a focus on electrocatalysis and corrosion. **Chapters 4 and 5** summarize the techniques employed to characterize these systems, while **Chapters 6 and 7** briefly summarize the results and outlook of this thesis, respectively. A collection of publications and manuscripts related to these findings is enclosed in the thesis.

2. Materials

This chapter introduces the basic concepts of material science and surface science, with a focus on the surface processes relevant for this thesis, in particular surface oxidation. A brief description of gold (Au), studied in **Papers I-VIII**, platinum (Pt), studied in **Paper X**, and nickel (Ni) alloy 59, studied in **Papers I and IX**, and their most common oxides and hydroxides structures is given at the end of the chapter.

2.1 Crystals, metals, oxides

This thesis revolves around the electrified interface between solids and liquids, with a focus on the solid surfaces. In solids, the constituents (atoms, ions or molecules) are tightly packed and held in fixed positions, giving the material a definite shape and volume[32]. Here, it is very useful to think of an atom simply as a sphere. When these spheres are arranged in periodic arrays, we call it a "crystalline" solid. Thus, a single crystal consists of a perfect solid lattice of particles with ideally infinite long-range periodicity, in all directions of space (Fig. 1a)[33].

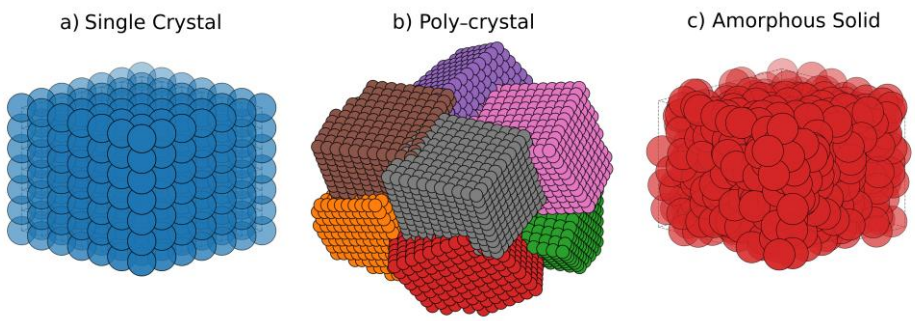

Figure 1
a) Example of a single crystal, an ideally perfectly ordered material where atoms are periodically arranged in three dimensions. b) Example of a polycrystalline material made of many randomly oriented crystalline domains, called crystallites or grains. c) Example of an amorphous solid, completely lacking long-range structural periodicity.

The samples studied in this thesis (Au, Pt and Ni alloy 59) can be classified as metals or as mixture of different metals (metallic alloys), which are naturally found as

"polycrystalline", i.e. solids composed of many small crystalline domains, each with a different orientation in space or even a different atomic structure (Fig. 1b). In some other cases, however, there are solids that even completely lack crystallinity, i.e. atomic-scale periodicity, like glass, which are called "amorphous" (Fig. 1c)[33].

Thanks to their periodic structures, single crystal lattices can be classified by their translational and rotational symmetries. In a three-dimensional (3D) space there are only 14 distinct types of lattices, called Bravais lattices, each of them characterized by a primitive unit cell, which is the smallest repeating building block of a lattice[33]. A primitive unit cell always contains one lattice point, which is decorated with one or more atoms, ions or molecules, called basis of the crystal. Sometimes it is useful to describe a lattice using a conventional unit cell that contains more than one lattice point. Cubic cells define the most common Bravais lattices found in nature and can be easily described by a single length 'a', equal for all the edges of the cube, and 90° angle between them. There are three main forms of cubic structures (Fig. 2): simple cubic (sc), body centered cubic (bcc) and face centered cubic (fcc)[33]. Sc exhibits the most straightforward unit cell, with one lattice point at each corner of the cube. Assuming a basis of one atom and considering that each lattice point is shared with 7 other neighboring cells, it can be seen that the sc is a primitive unit cell containing one single atom. On the other hand, bcc and fcc are conventional cells that can be built starting from the sc: bcc contains one extra atom in the center of the cube, i.e. having a total of 2 atoms per cell, while fcc contains one extra atom on each face of the cube, i.e. having a total of 4 atoms per cell.

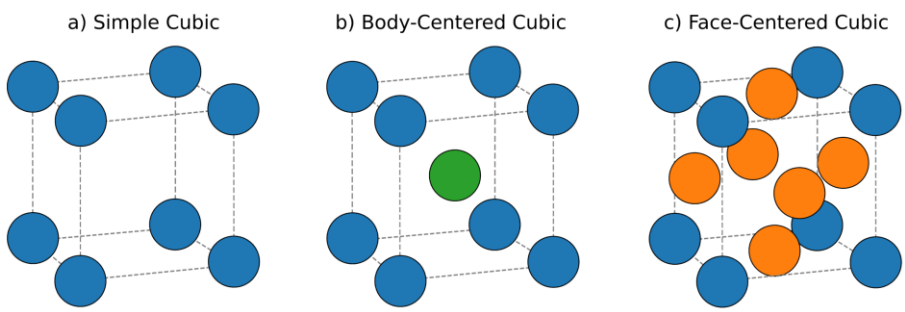

Figure 2
Cubic crystal lattices are defined by three types of unit cells: a) simple cubic, b) body-centered cubic, and c) face-centered cubic.

Besides pure metals, another class of materials crucial for this thesis and very common in our everyday life are metal-oxides, i.e. the chemical compounds formed upon reaction of a metal with oxygen. Differently from a metal, which is pictured as a structure of positive ions held together in a "sea" of delocalized electrons, a metal-oxide is predominantly characterized by stronger and more stable ionic bonds

with more localized electrons, leading to very different material properties[32]. In fact, oxygen is quite electronegative and will likely "steal" an electron from the metal atom to fill up its outer shell. This electron transfer introduces the concept of oxidation state, a formalism used to describe the effective charge of an atom within a compound, indicating how many electrons the atom has lost or gained relative to its elemental form. Oxygen in the oxide will be negatively charged (O^{2-}), while the metal ions will be positively charged (M^{n+}). The opposite reaction to oxidation is reduction, where the metal ion is supposed to re-gain the electron from the oxygen to re-store its metallic state. In environments like water where not only oxygen but also hydrogen is present, hydroxides or oxy-hydroxides can form, characterized by the presence of additional hydroxyl groups (OH^-) in the lattice.

In general, most metals tend to react quite easily with oxygen and water, for example iron is well known to naturally form rust due to corrosion. However, many metals or alloys, e.g. silicon, nickel, aluminum, etc. can spontaneously form a thin native passive oxide that prevents bulk oxidation and rapid degradation[34]. Finally, there is a class of metals that does not spontaneously oxidize in ambient conditions, called noble metals, e.g. palladium, silver, iridium, platinum, gold, etc. A very stable electronic structure makes these materials inert in many environments[33], but not always. This thesis will address how the noble metals Au and Pt may be electrochemically oxidized into their respective (hydr)oxides, and how the native passive (hydr)oxides of Ni alloy 59 evolve under electrochemical polarization. The most established bulk structures of Au, Pt and Ni alloy 59 oxides and hydroxides are shown and discussed in **Sections 2.3, 2.4 and 2.5**, respectively.

2.2 Surfaces

So far, only 3D structures that ideally extend infinitely in space, called "bulk", have been discussed. However, real objects are finite in space and thus exhibit a surface and an interface, i.e., the two-dimensional (2D) boundary between the bulk solid and its surroundings, which often controls how the material interacts with the environment. For example, a material can be made completely impermeable by making its surface hydrophobic[35]; the color and optical properties of a material can be modified by changing the surface capability to absorb light[36]; a coating or thin film can provide new mechanical properties such as toughness[37], erosion resistance[38], etc. Without ever modifying the bulk material, surface functionalization at the micro- and nanoscale can completely transform an object into something else. This concept is extremely powerful and has many applications[6,34,39–41], including electrocatalysis and corrosion.

In this context, it is necessary to describe surfaces in detail. When cutting a bulk polycrystal along a random plane, its surface would show different crystalline domains called grains, separated by grain boundaries. Assuming that all the domains share the same crystalline structure but are differently oriented in space, each grain will show a different surface orientation (Fig. 3). Hence, due to the presence of multiple surface orientations, it is more complicated to establish structure-performance relationships of polycrystalline materials. To fundamentally understand the behavior of different surface structures, which is a central purpose in surface science studies, well-defined model systems such as single crystals become extremely useful.

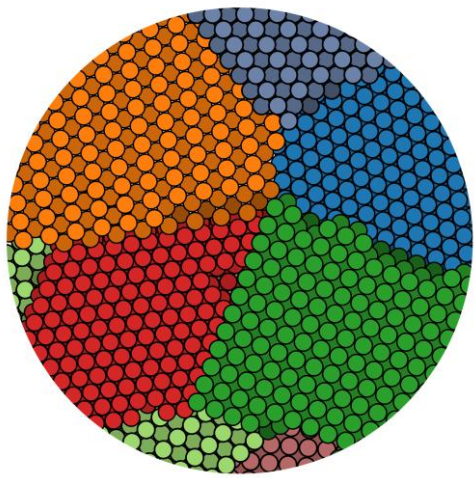

Figure 3
Schematic drawing of a polycrystalline surface exhibiting grains with different orientations.

2.2.1 Atomic planes

As for bulk structures in 3D space, surface structures can be periodic in a 2D space and can be described by 7 Bravais surface lattices, arising from the truncation of 3D crystals[33,42]. A 3D crystal can be cut along a specific plane, labelled with Miller indices h, k, l, resulting from the position of the atoms in the lattice and their distances[33,42]. The most relevant and common fcc planes are shown in Fig. 4. The differences between surface structures directly affect properties like surface energy, amount of undercoordinated atoms, adsorption sites, movement of dislocations etc. which can be crucial in determining the material properties, from their catalytic behavior to their stability.

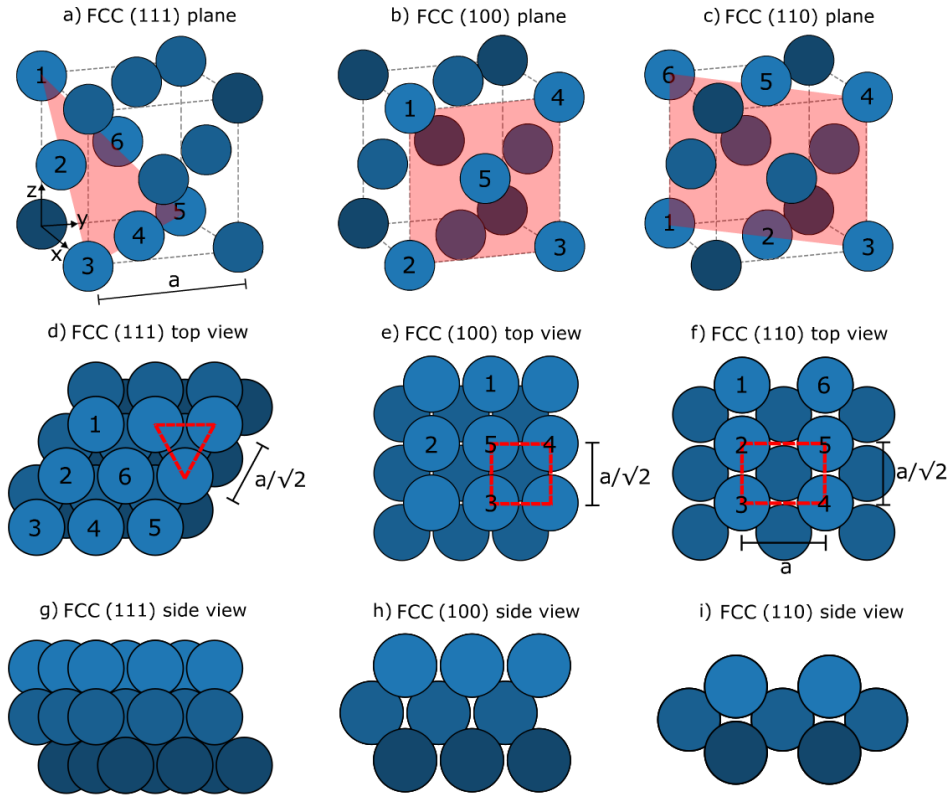

Figure 4

Main atomic planes of fcc cubic lattices. a,d,g) cutting the lattice along the (111) plane leads to an hexagonal unit cell with 6 in-plane nearest neighbors and in-plane lattice spacing $a/\sqrt{2}$. b,e,h) The (100) plane is less densely packed than the (111) surface, with 4 in-plane nearest neighbors and a squared unit cell with in-plane lattice spacing $a/\sqrt{2}$. c,f,i) The fcc(110) plane is the least densely packed surface presented here, with 2 in-plane nearest neighbors and a rectangular unit cell of lattice spacing a and $a/\sqrt{2}$.

The first explanation for the appearance of specific geometries like triangles and squares within the atomic planes finds its origins in 1611, when Johannes Kepler proposed that equal spheres naturally pack most densely in triangular arrangements, leading to 3D close-packed structures[43]. This "Kepler conjecture," proven in 1998[44], explains why efficient packings like fcc are so common in nature. A second structure that can achieve a close-packing density of ~74% in volume, exactly as much as for the fcc, is called hexagonal close-packed (hcp) (Fig. 5)[42].

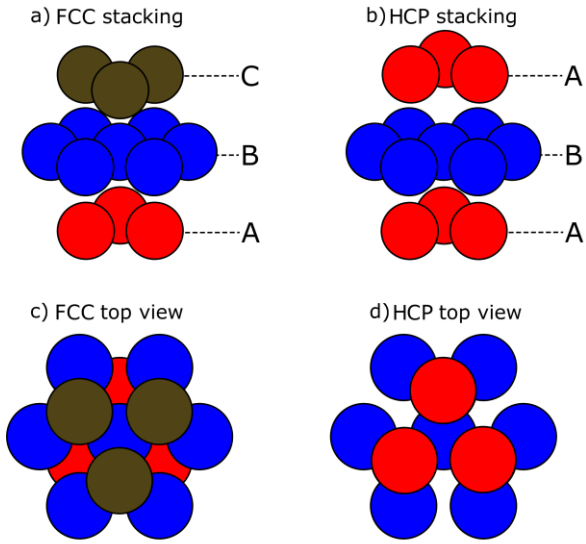

Figure 5
Schematic drawing of: a,c) fcc(111) planes stacking in an ABC sequence and b,c) hcp(0001) planes stacking in an AB sequence. Both structures present an hexagonal 2D-lattice.

2.2.2 Surface reconstruction

The surface atoms are at the interface with the surrounding environment, they are intrinsically under-coordinated with respect to the bulk atoms, and they can experience surface stress[42,45]. Therefore, they might tend to lower their surface free energy and stress by rearranging themself to form a new periodic structure that differs from that of the ideal bulk-terminated lattice. This action will be countered by the mismatch between bulk and surface atoms occurring due to reconstruction, leading to a minimum surface energy configuration that results from the balance between these two contributions[42,45]. The Au(111) reconstructed surface is also known as "Herringbone" reconstruction (Fig 6), its unit cell is denoted as $22x\sqrt{3}$[46]. The top layer densifies into a stripe pattern by insertion of an extra Au atom every 22 atoms along the [110] surface direction, causing a surface corrugation of 0.2 Å. The formation of this stripe pattern mainly releases the tensile stress in the top layer along the [110], inducing a compression of ~4% with respect to the bulk lattice. This mismatch along the [110] direction induces a periodic shift of the topmost atoms between fcc and hcp sites. Only a few atoms per unit cell are aligned with the bulk positions, and the atoms in between the fcc and hcp domains will occupy bridge-sites. The stripe pattern is, however, not entirely stable and will be rotated by 120° against each other to further reconstruct into a herringbone-like superstructure.

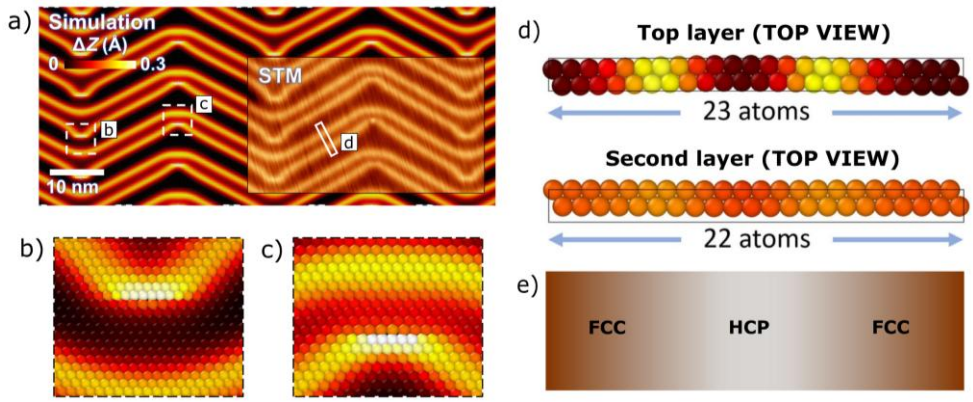

Figure 6
a) Simulated and STM images of the Au(111) reconstructed surface, also known as Herringbone reconstruction. b,c) Atomic details of the elbows. d) Top views of the first and second layers of the unit cell. e) Simplified top view highlighting the fcc and hcp domains in the unit cell. This figure is adapted from ref. [46], licensed under CC BY 4.0.

2.2.3 Adsorption and surface oxidation

There are other phenomena closely linked to surface reconstruction, such as surface adsorption and oxidation. In heterogeneous catalysis, electro-catalysis, corrosion etc. adsorption and surface oxidation are fundamental processes that govern the (electro)chemical behavior and stability of solid surfaces[42,45]. In this context, single-crystal surfaces provide well-defined, reproducible systems allowing us to correlate the atomic-scale structure to the material properties. In particular, the surface structure can directly dictate how adsorption and surface oxidation processes take place during a chemical or electro-chemical reaction. *Vice versa*, adsorption and oxidation can induce changes in the surface structure.

Adsorption is the attachment of atoms, ions, or molecules from a surrounding environment onto a solid surface affecting how the surface interacts chemically with its environment, controlling reaction rates, selectivity, and overall efficiency. As an example, the adsorption of atomic oxygen on Pt(111) forming an hypothetical p(3x3) superstructure is shown in Fig. 7a,c, where the oxygen atoms occupy discrete adsorption sites forming a surface lattice unit cell 3x larger than the Pt(111) unit cell.

There are two types of adsorption mechanisms: physisorption and chemisorption, depending on the strength of the bond between adsorbate and substrate[42,45]. Physisorption is relatively weak, based on interactions such as Van der Waals forces. Chemisorption is associated to a stronger chemical bonding and can be more heavily affected by the specific adsorption sites, i.e. the structure of the surface. At

a higher oxygen chemical potential, surface oxidation can take place, leading to the formation of a distinct surface phase with new properties, such as structure, stability and stoichiometry. Oxygen atoms can occupy several sites and layers in the surface oxide, leading to a clear change in surface periodicity and bonding environment, for example expanding the (111) lattice. An example of an hypothetical PtO_2 surface oxide formed on Pt(111) is shown in Fig. 7b,d.

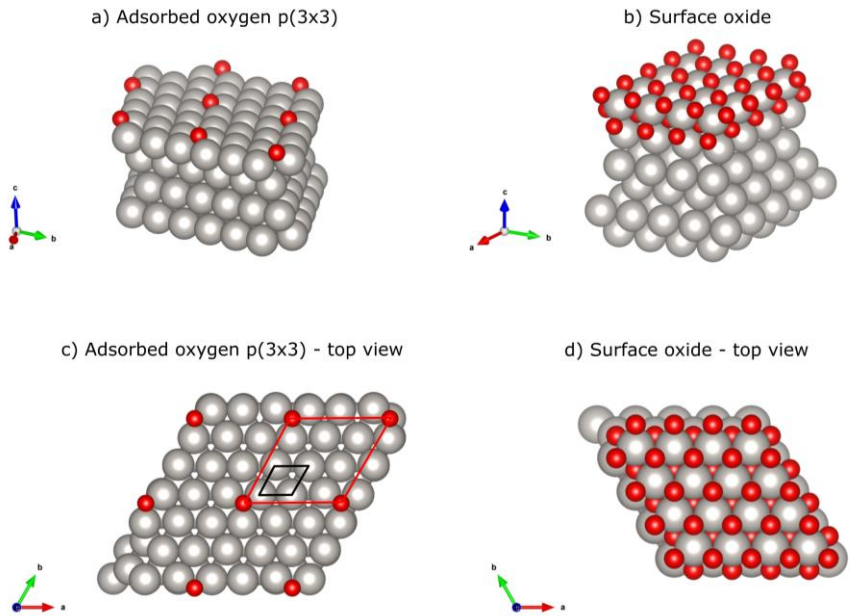

Figure 7
a,c) Example of an hypothetical p(3x3) overlayer of adsorbed oxygen on Pt(111). b,d) Example of an hypothetical PtO_2 surface oxide formed on Pt(111). The structures are drawn using VESTA[47].

For all the aforementioned phenomena, surface defects and surface diffusion play a key role. For example, in heterogeneous catalysis and electro-catalysis, adsorbed species usually diffuse on the surface between available adsorption sites before a product is formed. These adsorption sites are typically separated by energy barriers being smaller than the energy barrier for desorption[45]. Similarly, the surface morphology resulting from oxidation and reduction cycles depends on the mobility of the atoms during oxide formation and decomposition[48–50]. In these cases the surface might show defects such as vacancies, islands, steps or kinks which are generally more reactive and mobile than flat terraces[45]. These processes have a certain degree of reversibility and probability to occur, in particular the diffusion coefficients of e.g. surface adatoms and vacancies are shown to increase exponentially with temperature and surface charge[42,45], having thus crucial effects on the material and device properties. The most relevant surface defects and transport processes are summarized in Fig. 8.

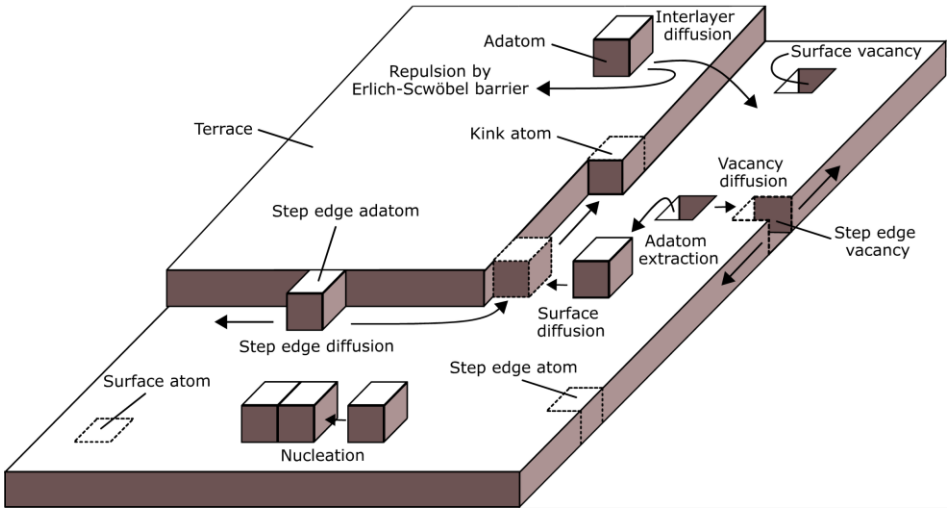

Figure 8
Schematic of elementary transport processes and surface defects, inspired by ref. [51].

Although surface diffusion processes can help describing the kinetics of adsorption/desorption, dissociation of a molecule and onset of oxidation, an explanation on the mass transfer during oxide growth at room-temperature cannot be solely based on temperature driven diffusion. After a monolayer of oxide is formed, what is the force that drives further oxidation? In the late 1940s Cabrera and Mott proposed a theory to explain metal oxidation and oxide growth at temperatures typically below ~300°C[52,53]. As shown in Fig. 9, the Cabrera-Mott model postulates that upon adsorption and dissociation of oxygen molecules on the metal surface, a charge transfer between metal and oxygen ions occurs, leading to a strong electric field (E-field) built up across the metal-oxide interface. This E-field is expected to be sufficiently high to drive the migration of ions through the interface, which determines the rate of oxide growth. This theory has also been demonstrated experimentally in a recent study[54]. As the oxide film grows thicker, the E-field strength decreases, slowing down the transport of ions and thus the oxide growth. As a result, the model predicts logarithmic growth kinetics which explains why many metals in air form surface oxides of only a few nm that essentially become self-limiting, observed in many studies[34,55–57]. Note that this model assumes a steady supply of oxygen, while ion migration through the oxide is the rate limiting step. However, especially as the oxide gets thicker, adsorption and electron transfer kinetics can change significantly, affecting the oxygen supply, hence, the oxide growth[58].

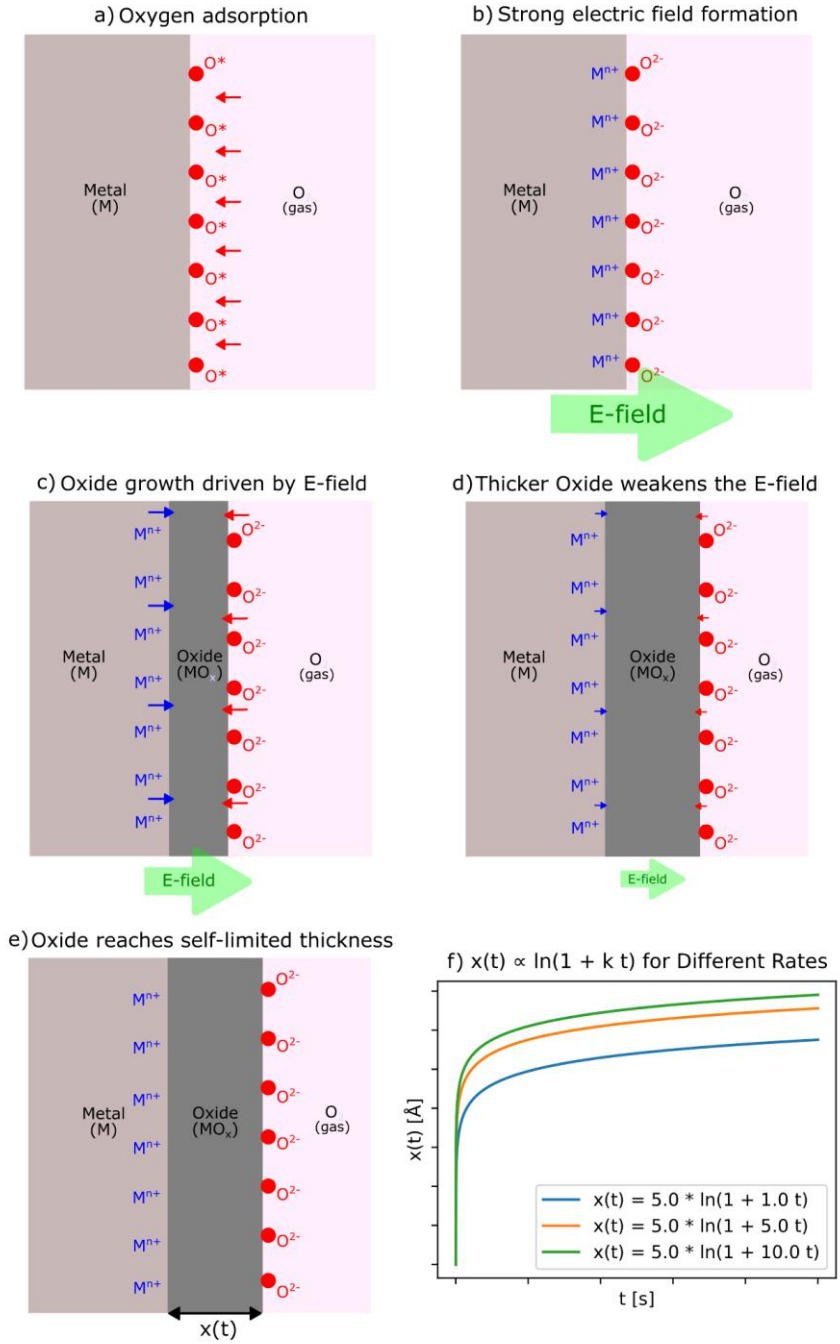

Figure 9
a-e) Schematics of the steps involved in the Cabrera-Mott model of self-limiting oxide growth.
d) Logarithmic growth kinetics of the oxide thickness over time x(t) for different growth rates k.

2.3 Gold

Au is a noble transition metal with a fcc crystal structure (a ~ 4.08 Å), often referred as the "noblest of all metals" thanks to its remarkable chemical and structural stability in a large range of conditions[59]. These properties make gold a fundamentally interesting material, which often serves as a model system in surface science and (electro)catalysis. Its plasmonic and surface-functionalization properties further extend its relevance as a substrate in nanoscience and spectroscopy. Among its crystallographic facets, Au(111) is particularly well known for its herringbone reconstruction, which influences surface diffusion, adsorption energetics, and reactivity. In electrocatalysis, gold is relevant for industrial applications involving the conversion of chemicals[60,61], oxidation of CO[62], alcohols[63], sugars[64] and for the ORR[65,66], and has served for fundamental studies on noble metals surface oxidation[67–69], dissolution[11,70], OER mechanism[71–73] and other electrocatalytic reactions[74,75]. Although gold electrochemical oxidation has been studied for many decades and it is expected to take place in many of these processes, uncertainties remain about the (hydr)oxide structures involved, the oxidation kinetics, the link between activity and stability, etc. This lack of clarity is largely due to the difficulties of probing these ultrathin, amorphous, and unstable phases.

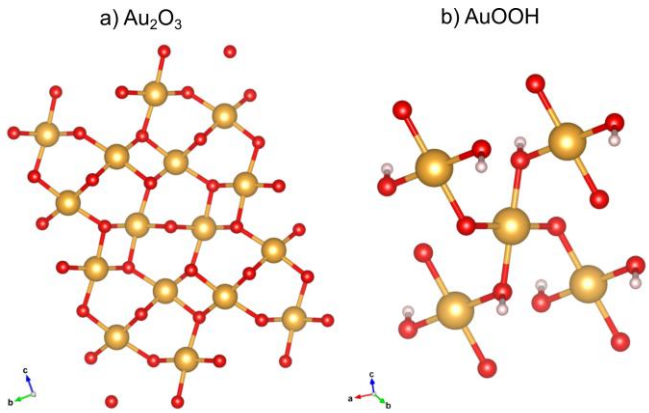

Figure 10
a) Structure of bulk Au_2O_3 and b) DFT calculated structure of AuOOH, not proven experimentally. The structures are drawn using VESTA[47] with atomic coordinates from ref. [76,77]. The arrows denote the crystallographic axes of the unit cells.

The most well-known and stable oxidation state of gold observed in the presence of oxygenated species is Au^{3+} forming an oxide Au_2O_3 (Fig. 10a)[71,78,79], but under certain conditions, surface oxidation was also proposed to take the form of an hydrous oxide $Au_2O_3 \cdot (H_2O)_n$[80,81], an hydroxide $Au(OH)_3$[82], or an oxy-hydroxide AuOOH[72] or other less common and unstable oxidation states[80,83]. Except for Au_2O_3, the bulk structures of the hydroxylated or hydrated Au^{3+} compounds remain

substantially unknown. An example of a proposed structure of AuOOH calculated with density functional theory (DFT) is shown in Fig. 10b. In general, it is expected that most of the Au^{3+} compounds hold a square planar geometry with a bond length around 2 Å[84].

2.4 Platinum

Pt is a noble transition metal with a face-centered cubic (fcc) crystal structure (a ~3.92 Å), renowned for its exceptional catalytic activity and chemical robustness under a broad range of conditions. Unlike Au, Pt is less inert, showing an intermediate binding strength toward adsorbates, making it one of the most extensively studied materials in surface science, heterogeneous catalysis, and electrocatalysis[6,85–88]. As such, Pt is often found in real-world applications, including electrolyzers and fuel cells. In particular, platinum is the state-of-art catalyst for key reactions like the hydrogen evolution reaction (HER) and the ORR[6,88]. Processes like ORR often occur at potentials and conditions where surface oxides and hydroxides can form, leading to dynamic surface restructuring and changes in catalytic activity. Thus, understanding the electrochemical behavior of Pt is essential not only for fundamental electrochemistry but also for improving the performance and durability of fuel cells and electrolyzers. The precise nature, structure, and stability of several oxidized surface species remain subjects of debate[51,89,90], the most established reported bulk oxides structures include PtO and PtO_2, shown in Fig. 11.

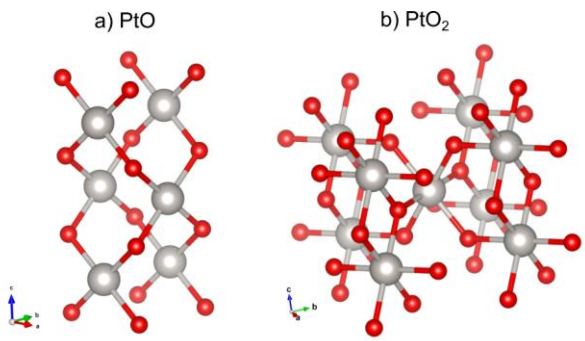

Figure 11
a) Structure of bulk PtO and b) structure of Bulk PtO_2. The structures are drawn using VESTA with atomic coordinates from ref. [91,92]. The arrows denote the crystallographic axes of the unit cells.

2.5 Nickel alloy 59

Thanks to the excellent mechanical and corrosion properties, Ni alloy 59 is used in gas turbines, oil & gas, nuclear and chemical industries, for demanding applications and harsh environments, such as high temperatures, corrosive media and high mechanical strain conditions[93–95]. Although the bulk composition of Ni alloy 59 is 60.07% Ni, 22.7% Cr, 15.4% Mo, and 0.8% Fe, the native passive film protecting the material is enriched in Cr and Mo. Due to the presence of Mo- and Ni-oxides and hydroxides in the passive film, the material is found active towards OER. The most relevant oxide and hydroxide bulk structures are shown in Fig. 12.

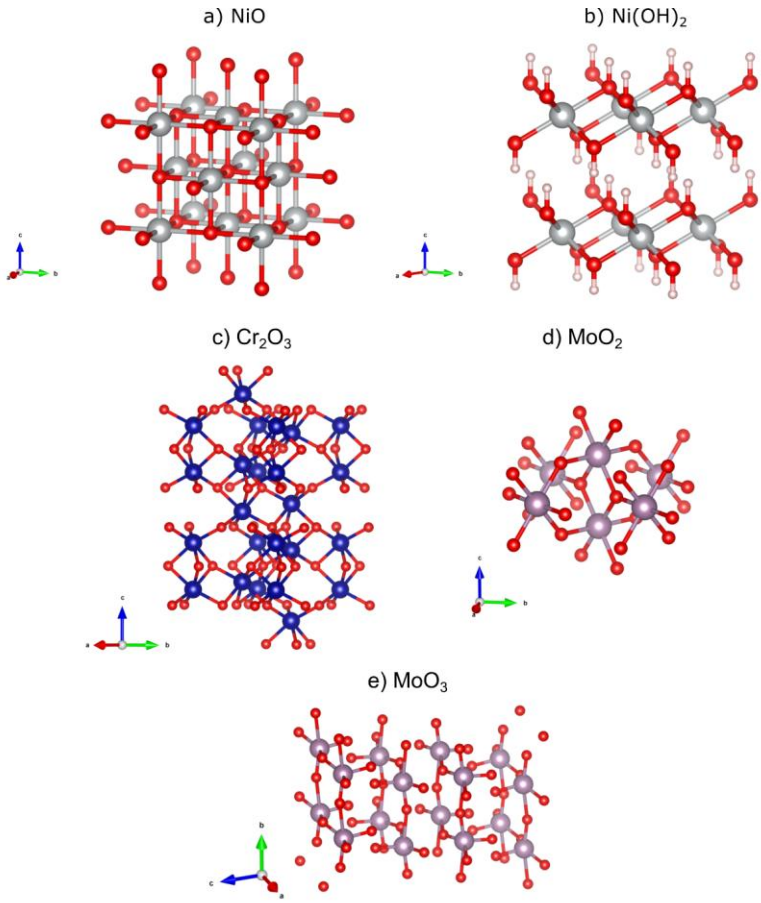

Figure 12
Bulk structures of a) NiO, b) $Ni(OH)_2$, c) Cr_2O_3, d) MoO_2, e) MoO_3 The structures are drawn using VESTA[47] with atomic coordinates from ref. [96–100]. The arrows denote the crystallographic axes of the unit cells.

3. Electrocatalysis and corrosion

This chapter provides the basics of electrochemical measurements and processes, with a focus on water electrocatalysis and corrosion, which are both related to the performance of electrolyzers and fuel cells. In particular, the electrocatalytic reactions discussed in this chapter are the OER, coupled with the electrochemical oxidation and degradation of Au (**Papers I-VIII**), and with the corrosion of Ni alloy 59 (**Papers I and IX**); and the ORR, coupled with the electrochemical oxidation and degradation of polycrystalline Pt (**Paper X)**.

3.1 Fundamentals of electrochemistry

Electrochemistry is a branch of physical chemistry that studies the relationships between chemical changes and charge transfers at the electrode-electrolyte interface, processes in which electrical energy can be used to drive a non-spontaneous chemical reaction or to exploit a spontaneous chemical reaction to generate electrical energy. This is possible to achieve using an electrochemical cell[1], for example the two-electrodes setup shown in Fig. 13a which is typically used at the industrial level in electrolyzers, fuel cells, batteries etc.

The term “electrode” represents an electrical conductor or semiconductor in an electrochemical cell and is the conductive material in contact with the electrolyte. In a two-electrodes setup, two electrodes are partially submerged in the electrolyte and are placed in electrical contact externally through a metallic wire. In “aqueous electrochemistry”, the electrolyte is always a water-based solution that serves as an ionic conductor completing the electrical circuit. The working electrode (WE) is a term used in scientific investigations to denote the sample under study, while the counter electrode (CE) serves as a sink or source of electrons. As shown and described in **Section 3.2.1**, a more sophisticated three-electrodes setup is typically used for research studies.

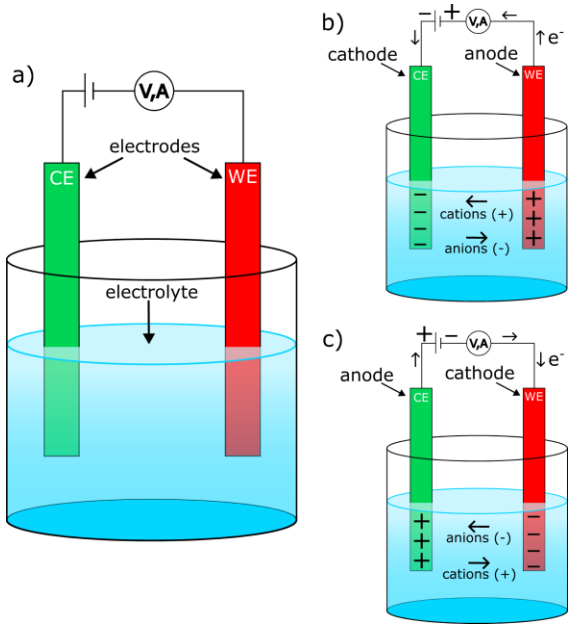

Figure 13
a) Schematic of a two-electrodes electrochemical cell. Using a potentiostat or a power supply, an external potential can be applied between counter electrode (CE) and working electrode (WE) to drive a non-spontaneous reaction. b,c) Depending on the sign of the applied potential, one electrode will be the anode, where an oxidation reaction takes place, and the other will be the cathode, where a reduction reaction takes place.

If an electrical potential is applied between WE and CE, using a potentiostat or a power supply, the electrons will be forced to move through the wire from one electrode (anode) to the other (cathode). This will result in an excess of either negative or positive charges at the electrode surfaces, leading to ion movement in the electrolyte (Fig. 13b,c). Moreover, as shown in Fig. 14a, the excess of electrons at the cathode will raise the energies of all electronic states, while the lack of electrons at the anode will lower their energy[1,101]. The suitable alignment of electronic states allows for tunnelling of one electron from the cathode to the lowest unoccupied molecular orbital (LUMO) of an atom/molecule in the solution, inducing a reduction reaction (Fig. 14b), or from the highest occupied molecular orbital (HOMO) atom/molecule in the solution to the anode, inducing an oxidation reaction (Fig. 14c)[1,101]. However, it is not always necessary to apply an external potential to observe an electrochemical reaction; depending on the electrode material and the electrolyte solution, electron transfer can occur spontaneously. As an example, anodic and cathodic reactions can take place when the electrons can flow spontaneously from a less noble (more prone to oxidation) to a more noble (less prone to oxidation) electrode, producing a current (see, for example, the

Voltaic pile in 1799 and the Daniell's cell in 1836[102,103] or more in general the galvanic corrosion process[104]).

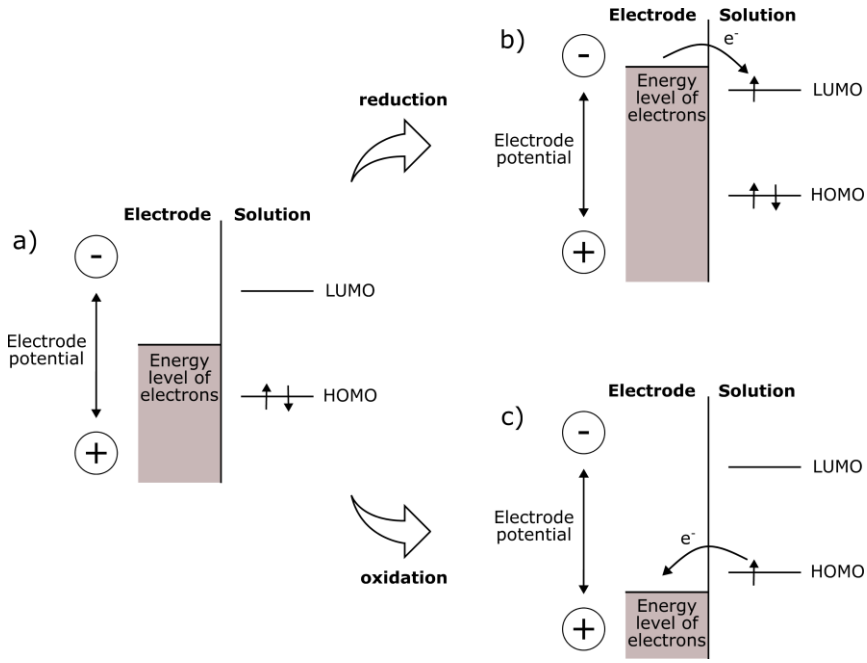

Figure 14
a) Schematic of the energy level alignments modified by the applied potential, which drive electrochemical reactions. b) At a sufficiently negative electrode potential, an atom or molecule in the solution can be reduced. c) At a sufficiently positive electrode potential, an atom or molecule in the solution can be oxidized. Adapted from ref. [1].

Through an electrochemical cell like the one shown in Fig. 13 it is then possible to physically separate a single redox (reduction-oxidation) reaction into two separate half-reactions, one taking place at the anode and one taking place at the cathode. A redox reaction is a chemical reaction where one species is oxidized and one is reduced, as in the water-splitting reaction:

$$2H_2O \rightarrow 2H_2 + O_2 \qquad (1)$$

The oxidation state of H and O in H_2O is formally +1 and -2, respectively, while the oxidation state of molecular hydrogen and oxygen is 0. Hence, the overall water-splitting reaction is a redox reaction where hydrogen gets reduced and oxygen gets oxidized. This reaction can be split into two half-reactions, which in the case of acidic water-splitting are the following:

$$2H^+ + 2e^- \rightarrow H_2 \qquad (2)$$

$$2H_2O \rightarrow O_2 + 4e^- + 4H^+ \qquad (3)$$

Reaction (2) is a reduction reaction representing the evolution of hydrogen gas (HER) while reaction (3) is an oxidation reaction representing the evolution of oxygen (OER). At the cathode, HER will take place, involving a charge transfer from the electrode to the hydrogen ions. On the other side of the electrochemical cell, OER will take place at the anode, where charge transfer occurs from the electrolyte to the electrode.

The possible processes involved in an electrode reaction are summarized in Fig. 15. There are four major contributions governing the reaction rate and thus the current at the electrodes[102]: I) mass transfer of species to/from the electrode surface; II) preceding and ensuing reactions, e.g., dissociation, solvent reorganization or other reactions with the surrounding environment; III) surface reactions (adsorption/desorption); and IV) kinetics of electron transfer. The slowest process will be the bottleneck of the electrode reaction, i.e. the rate-determining step. The findings of this thesis are mainly related to contributions (III) and (IV), i.e. surface reactions and electron transfer kinetics, where surface oxidation may be involved and can change the reaction path and energy landscape.

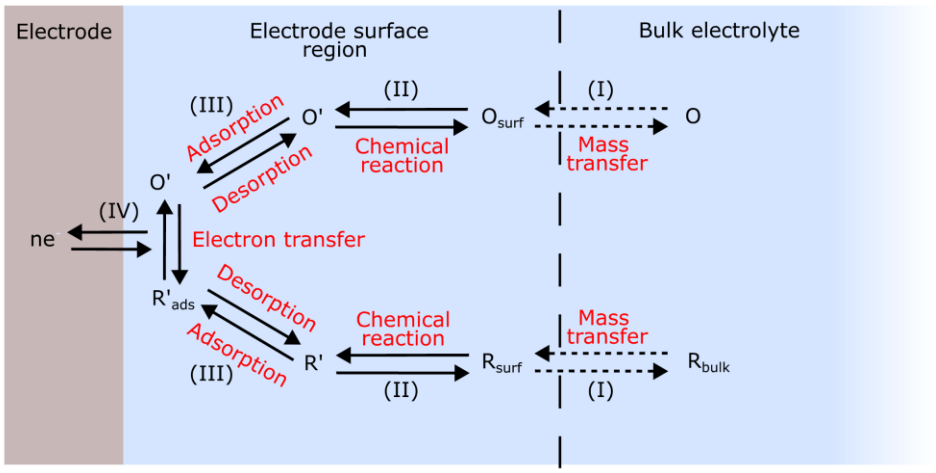

Figure 15
Possible processes/paths influencing an electrode reaction. Note that the "chemical reaction" step consists of additional reactions with the environment, which may take place at the electrode surface region or in the bulk electrolyte. Adapted from ref. [102].

However, even without electron transfer, depending on the charge of the electrode, there will be attraction and adsorption of some counterions to balance the excess of charge, as well as some preferential orientation of the polar water molecules in proximity of the surface of the electrode. The accumulation of charges on the surface driven by electrostatic forces can be seen as the behavior of a capacitor. This charge re-distribution is referred to as the formation of the electrical double layer (EDL)[102]

(Fig. 16a), initially proposed by Helmholtz in 1853. The overall result is two layers of charge, called inner and outer Helmholtz planes (IHP and OHP), and a potential drop confined in this region (Fig. 16b). The IHP is characterized by specifically adsorbed ions, dehydrated ions and dipoles. The OHP is characterized by non-specifically adsorbed ions which remain fully solvated (Fig. 16a). From the OHP, the diffuse layer begins, where a concentration gradient of ions is expected until the bulk concentration is reached. Depending on the extent of the potential drop in the IHP, which is the strongest drop predicted across the interface in these conditions (Fig. 16b), co-ions could also be found in the diffuse layer.

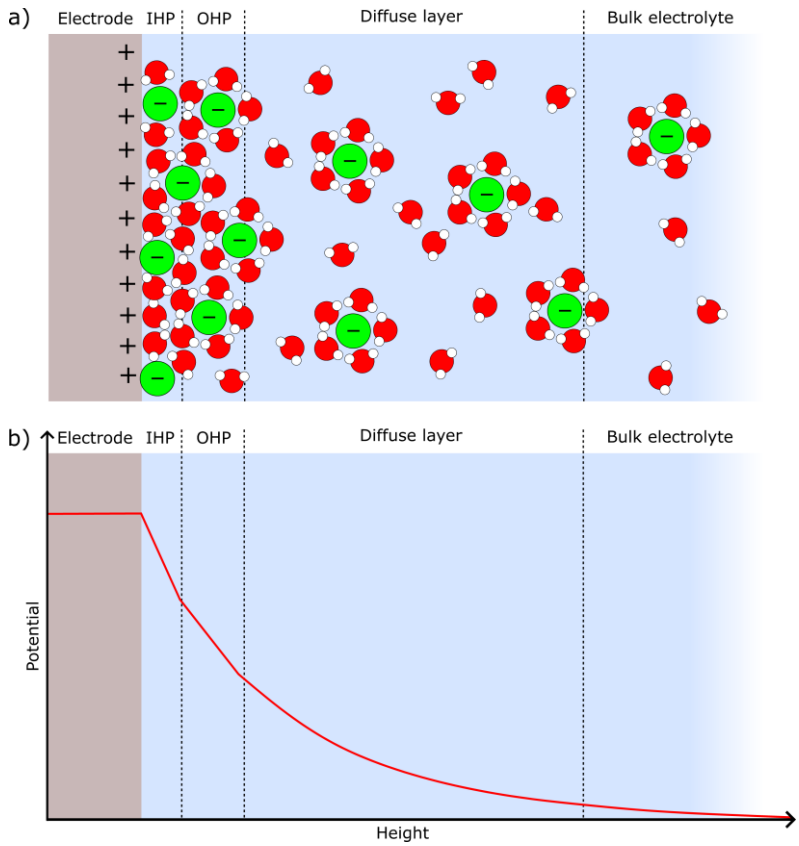

Figure 16
Example of (a) the EDL, adapted from ref. [102], and (b) potential drop across the interface.

As mentioned before, the surface charge can be either positive or negative, depending on the external potential applied as well as on the spontaneous interaction between electrode and solution. A surface charge can indeed spontaneously build up even without applying an external potential, at the open circuit potential (OCP). Thus, there has to be a potential where the surface charge goes from positive to

negative values and *vice versa*. This is called potential of zero charge (PZC)[1]. At this potential, the surface charge is zero, there is no preferential accumulation of ions and the water dipoles exhibit random orientation.

Fundamentally understanding the EDL and the electrode surface chemistry can help to rationalize the potential drop across the interface between electrode and reactant in solution. Redox species in the EDL might not directly experience the metal's Fermi level, but they will feel the local potential at their position, which can be shifted with respect to the bulk. This, together with possible reorganization of the EDL and the electrode surface, will affect the effective driving force for electron transfer, and consequently the electron transfer kinetics.

The process of electron transfer was previously illustrated in Fig. 14 as a simple tunnelling of electrons from one phase to another. The details of electron transfer were rationalized by the 1992 Nobel Prize winner Rudolph A. Marcus, who developed the theory of electron transfer in the 1950s[105,106]. In Fig. 17a, the free energy of the reactant state (R) and the product state (P) are plotted along the reaction coordinate, which represents the collective motions of nuclei and solvent molecules that respond to charge redistribution as we go from reactants to products. Briefly, the theory is based on the fact that electrons motions are much faster than nuclei motions, such that electron transfer, assumed to be radiationless, takes place while molecules and solvent cannot rearrange. Therefore, there is an activation free energy (ΔG*) for this process, corresponding to the Gibbs free energy barrier required to reorganize the system into a transition state, where the free energies of donor and acceptor states are equal (Fig. 17a)[101]. In heterogeneous catalysis and electro-catalysis, the rate of electron transfer is often the key rate-determining step and depends exponentially on ΔG*. The role of a catalyst is indeed to reduce the activation energy by providing more favorable reaction paths (Fig. 17b), thereby increasing the reaction rate.

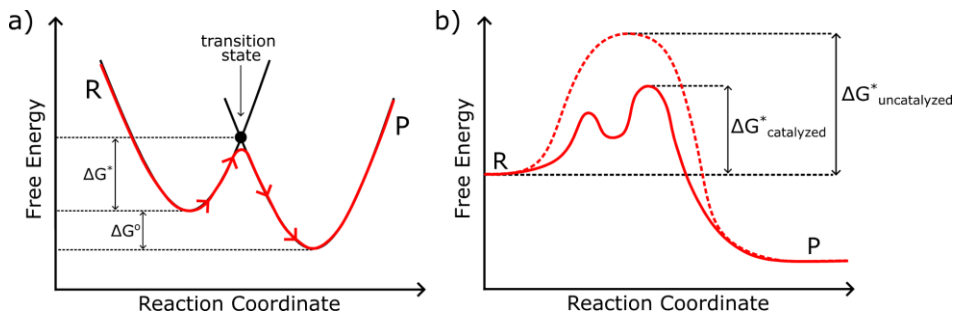

Figure 17
a) Schematics of the energy diagram to illustrate Marcus' theory for electron transfer. ΔG* is the Gibbs free energy required to reach the transition state, where electron transfer becomes energetically feasible. The reaction free energy (ΔG°) is the overall thermodynamic driving force between R a P at their equilibrium states. Adapted from ref. [101]. b) Schematic example of the effect of a catalyst on the activation barrier for electron transfer.

3.2 Electrochemical methods

3.2.1 Electrochemical cells

To conduct fundamental studies on the electrode-electrolyte interface, it is necessary to have control of the energy of the electrons within the WE, i.e., of the WE potential. This is impossible in a two-electrodes setup, where only the potential difference between WE and CE can be measured and controlled. To control the WE potential, a three-electrodes setup is required (Fig. 18), where the potential of the WE is measured against a reference electrode (RE).

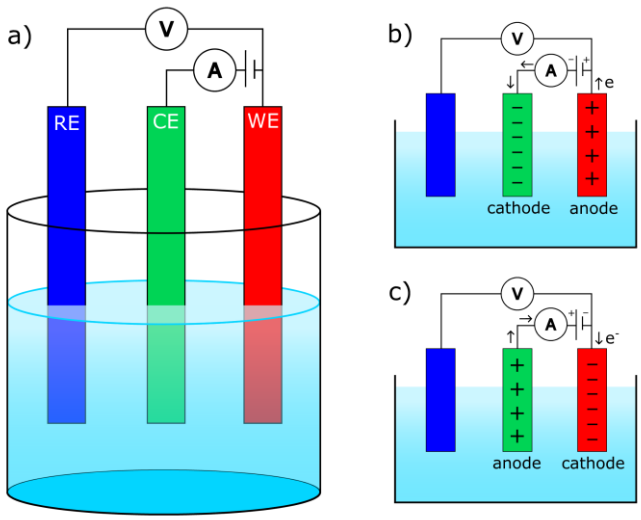

Figure 18
a) Three-electrodes electrochemical cell, b,c) the potentiostat measures the potential difference between WE and RE, while the CE acts only as a sink or source of electrons. As a result, WE and CE will still be the cathode or anode as for the two-electrode setup, but the RE has a stable and well-defined potential for reference.

Inside the RE, a fast and reversible reaction takes place, providing a stable and reproducible electrode potential, against which the potential of the WE is measured. There should not be any current disturbing the RE, which is close to an ideally non-polarizable electrode, i.e. it should resist potential changes under small current loads. In this configuration, the CE acts only as sink or source of electrons, but the potential difference is now measured between an electrode with a known potential (RE), and the sample (WE). As a result, it is possible to measure and thus control the WE potential accurately[101]. This is why in industry it is common to find two-electrodes setups, where the main interest is in the overall cell performance, while three-electrodes setups are widespread in research studies.

There are many types of RE. Depending on the reaction they are based on, they can be more or less suitable for certain types of electrolytes and for specific types of experiments. In this thesis, a saturated silver/silver-chloride electrode (Ag/AgCl) or a Reversible Hydrogen Electrode (RHE) were used, while it comes in handy to also introduce the Standard Hydrogen Electrode (SHE). Starting from the latter one, the SHE is based on the following reversible redox reaction of hydrogen protons to molecular hydrogen:

$$2H^+(aq) + 2e^- \rightleftharpoons H_2(g) \qquad (4)$$

The standard potential of this reaction at pH 0 (corresponding to a H^+ concentration of 1 M) is typically declared to be the zero point on the electrochemical potential scale, making this electrode the universal reference in electrochemistry. Every other RE potential is reported against SHE. However, it is rather complicated to maintain standard conditions for the hydrogen reaction in a RE, the SHE potential will shift with pH according to the Nernst equation (eq. 1), which describes the electrode potential (E) under non-standard conditions[102]:

$$E = E^o - \frac{RT}{2F}\ln\left(\frac{p_{H_2}}{(a_{H^+})^2}\right) \qquad (1)$$

$$E_{SHE} = 0 - \frac{0.059}{2} log\left(\frac{1}{(a_{H^+})^2}\right) = -0.059 * pH \qquad (2)$$

Where E^o is the potential in standard conditions (0 V in the case of SHE), R is the universal gas constant, T is the temperature, F is the Faraday constant (here multiplied by a factor of 2 since two electrons are involved to generate one H_2 molecule), p_{H2} is the partial pressure of hydrogen gas (1 bar in standard conditions) and a_{H^+} is the activity of hydrogen ions (related to pH by $a_{H^+} = 10^{-pH}$ in dilute aqueous solutions).

Therefore, it is more convenient to work with the RHE, which operates based on the same reaction of the SHE but at the actual pH of the test solution. The RHE is considered pH-independent because its potential is defined to be 0 V at any given pH, the RHE automatically adjusts to compensate the Nernst shift. The relationship between RHE and SHE scales is:

$$E_{RHE} = E_{SHE} + 0.059 * pH \qquad (3)$$

The saturated Ag/AgCl RE operates based on the following reversible redox reaction[102]:

$$AgCl(s) + e^- \rightleftharpoons Ag(s) + Cl^-(aq) \qquad (5)$$

The potential of this reaction against SHE is ~0.197 V, and it can be converted into RHE as follows:

$$E_{RHE} = E_{Ag/AgCl} + 0.059 * pH \qquad (4)$$

Where $E_{Ag/AgCl}$ corresponds to 0.197 V.

The choice and design of the most suitable RE typically depends on their stability and the cell design, but in general, there are plenty of optimization strategies that can be done on an electrochemical cell or device: from the choice of RE and CE, to the entire electrochemical cell geometry optimized to minimize ohmic drops and mass transfer limitations, to accommodate bubble evolution, avoid contaminations, etc. In this thesis, the electrochemical cells used (Fig. 19) are designed to perform *operando*, *in situ* and *ex situ* studies at the electrode-electrolyte interface, hence, they must also fulfill some other requirements.

All the cells shown in Fig. 19 are compatible with hat-shaped single- or poly-crystalline samples used as WE. As RE, a mini-electrode either Ag/AgCl or RHE is used, finally the CE used is a platinum rod or mesh. The electrochemical cell used for *operando* studies (Fig. 19a) is entirely made of an highly inert polymer, polyetheretherketone (PEEK), and it is used for RefleXAFS (**Papers I, II, VII, VIII, X**), surface X-ray diffraction (SXRD) (**Paper V**), and 2D surface optical reflectance (2D-SOR) (**Papers II, V, VI**) studies. An important reason here for using PEEK is its relatively high transparency and high stability under the X-ray beam, as well as its machinability. The cell for *operando* studies allows for electrolyte flowing during measurements, which reduces mass transfer limitations and facilitates the handling of bubbles evolving during water-splitting. From the window placed on top of the cell, 2D-SOR microscopy can be performed, while from the thin walls (200 μm) at the neck of the cell, a focused hard X-ray beam can penetrate through the electrolyte and impinge on the surface at a grazing incidence angle. The cell shown in Fig. 19b is used for *in situ* ambient pressure X-ray photoelectron spectroscopy (AP-XPS) studies (**Papers IV, V, VII, IX**), where the electrodes are attached to a manipulator and the electrolyte is stored in a beaker, all of them kept inside a chamber at a pressure and temperature sufficient to prevent the electrolyte from evaporating. The electrodes can be dipped in the beaker and then withdrawn from the electrolyte to be studied after electrochemical treatment while an electrolyte layer is still present on the surface. In this case, only the sample holder is made of PEEK. Finally, the cell used for *ex situ* studies (Fig. 19c), entirely made of PEEK, is used together with a transfer system to perform ultra-high vacuum (UHV) studies (**Papers III and VII**). The sample is mounted on a manipulator and the surface can be dipped in the electrolyte to form a hanging meniscus. The sample can then be withdrawn from the electrolyte and transferred to a vacuum chamber for *ex situ* studies after the electrochemical treatment.

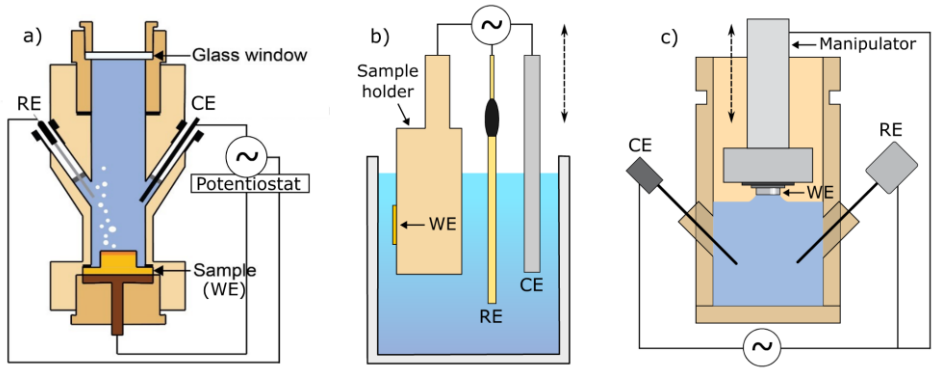

Figure 19
Electrochemical cells used for a) *operando* 2D-SOR, grazing incidence XAFS and XRD studies, b) *in situ* APXPS studies and c) ex *situ* UHV studies.

3.2.2 Chronoamperometry, Linear Sweep Voltammetry and Cyclic Voltammetry

The main electrochemical techniques used and presented in this thesis are chronoamperometry (CA), linear sweep voltammetry (LSV) and cyclic voltammetry (CV). These techniques are widely employed to study interfacial electron transfer kinetics and reaction mechanisms, as well as to assess the stability and reactivity of the electrodes[1]. However, since they only probe the electrical currents produced by electrochemical processes, these methods cannot directly discern between all the processes involved, such as structural and chemical changes of the interface, hence, they require complementary techniques to be fully understood.

CA experiments consist of applying one or more potential steps (Fig. 20a) and measuring the current response over time (Fig. 20b). In the example presented here, the potential is first stepped up from E_0 to E_1 at a time t_1 and a positive current spike is observed, indicating an anodic process. The current exhibits a typical response resulting from a combination of faradaic and non-faradaic processes where it exponentially decreases and reaches a steady state. Traditionally, the term "faradaic" is used to define those processes involving the transfer of electrons across the electrode-electrolyte interface, driving reduction or oxidation reactions[1]. As a counterexample, capacitive charging and discharging of the surface are non-faradaic processes, which do not involve redox reactions. Faradaic and non-faradaic processes cannot be easily distinguished, but usually in the CA response non-faradic processes are mainly associated with current spikes at the time of the potential steps, while faradaic processes dominate the steady state current. When the potential is

stepped down to E_0 at t_2, the current shows the opposite behavior due to cathodic faradaic and non-faradaic processes.

In contrast, typical voltammetry experiments consist of sweeping the potential linearly in one direction (LSV) or cyclically up and down (CV) (Fig. 20c) while measuring the current response (Fig. 20d). In the example presented here, the potential is linearly increased up to an upper potential limit (UPL) E_1 and then decreased back to its starting potential E_0, making a complete CV cycle. In this way it is possible to follow adsorption/desorption or oxidation/reduction processes. An important additional parameter introduced here is the potential scan rate, helpful to investigate the kinetics of a process. The electric current response shown in Fig. 20d may indicate that, during the anodic (upward) scan, an oxidation process could have taken place, as can be seen from the anodic peak. During the cathodic (downward) scan, a negative current peak is observed, suggesting that the oxidized species could now be reduced. The anodic and cathodic peaks observed in the CV can also be related to other processes, like adsorption and desorption, which are typically highly reversible[101]. In general, reversibility of a reaction is associated with how close in potentials are its anodic and the cathodic processes and is once again associated with electrode transfer kinetics, the EDL and the behavior of the surface.

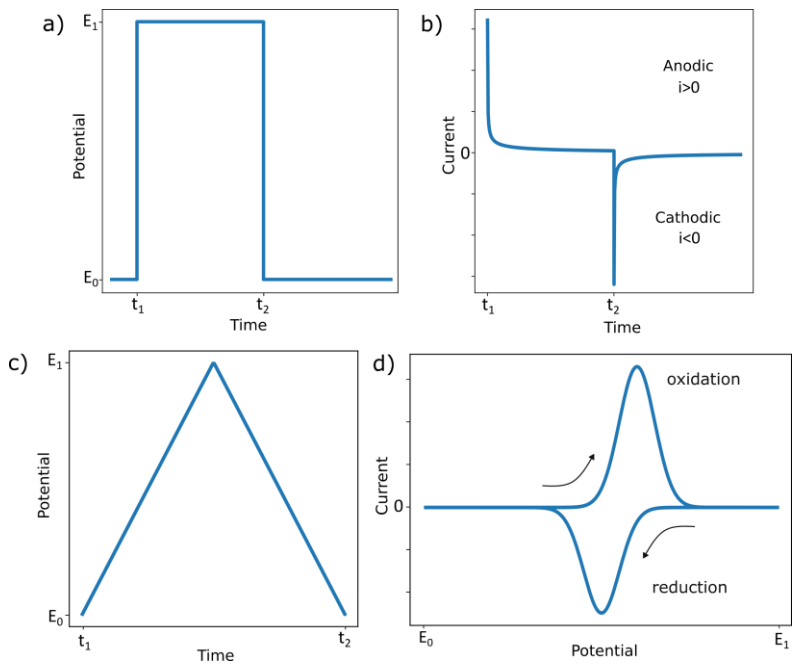

Figure 20
Example of a) an applied potential profile over time and b) current output over time in a chronoamperometry experiment. Example of c) applied potential over time and b) current output over applied potential in a cyclic voltammetry experiment.

3.3 Water electrolysis

The water-splitting reaction requires a large amount of energy to happen. In fact, the Gibbs free energy change (ΔG) for purely thermal water-splitting does not become negative until the temperature is increased to about 4300 K at 1 bar[107]. The advantage of using an electrochemical cell is that a different path is exploited, the molecules are not "heated up" and ΔG is supplied as electrical work[103] according to:

$$\Delta G = -\Delta E_{cell} z \mathcal{F} \qquad (5)$$

Where ΔE_{cell} is the cell potential ($E_{cathode} - E_{anode}$), z is the number of electrons involved in the reaction and F is the Faraday constant.

Thus, instead of requiring extreme thermal conditions, the reaction can be driven at ambient temperature by applying a sufficient potential difference between the electrodes[103]. Under standard conditions, the minimum theoretical cell potential required is 1.23 V, which corresponds to the Gibbs free energy change for the overall water-splitting reaction. This value defines the thermodynamic stability window of liquid water, as illustrated in the Pourbaix diagram (Fig. 21a), bound between the HER at 0 V_{SHE} and the OER at 1.23 V_{SHE}. The sloped boundaries with pH arise from the Nernst equation (eq. 3), which shifts the equilibrium potentials for both half-reactions.

Pourbaix diagrams[108] are widely used to study and predict the equilibrium states of electrochemical reactions for elements in the presence of aqueous solutions on a thermodynamic basis. These diagrams can be used to identify thermodynamically stable phases in certain conditions, however, present some limitations. For example, kinetic factors are not included in these calculations, the data are limited by the reactions which have been considered, the chemical potential of a substance can vary with the crystalline state of a solid compound, the activities of ions may differ from their real concentrations, etc. Experimental factors like defects in a solid, types of ions, temperature, role of electrocatalyst etc. require additional information, for example from DFT calculations, to assist the construction of more accurate Pourbaix diagrams[109].

In practice, real electrochemical water-splitting requires a larger applied voltage than what is shown in Fig. 21a, due to kinetic barriers, as described in Marcus' theory (Fig. 17). These appear as additional energy requirements beyond the thermodynamic minimum, known as overpotentials (η)[1]. As illustrated in Fig. 21b, an "ideal catalyst" at pH 0 would allow HER and OER to proceed exactly at their equilibrium potentials, revealed by a large increase of cathodic current (HER) and anodic current (OER). Real catalysts always present a shift of the onsets to more negative potentials for HER and more positive potentials for OER. The role of a good catalyst is thus to minimize η, but it cannot completely be avoided. The net effect is that the actual operating cell potential is increased by the sum of these

overpotentials, together with ohmic and transport losses. This highlights the central role of electrocatalysts to reduce kinetic barriers and thus bring the operational voltage closer to the thermodynamic minimum.

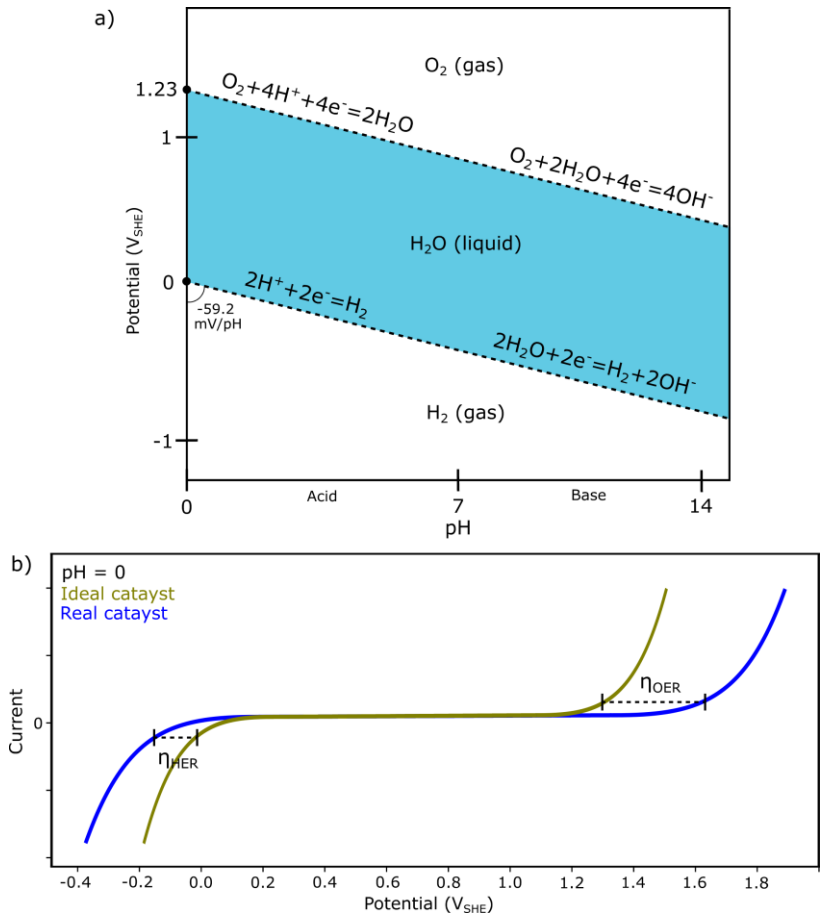

Figure 21
a) Standard Pourbaix diagram of water, adapted from ref. [110], licensed under CC BY-SA 3.0. b) Examples of a voltammogram from a linear sweep between HER to OER potentials expected for an ideal catalyst and a real catalyst in pH 0 solutions.

As can be noticed in Fig. 21a, different half-reactions of HER and OER are expected to take place depending on the pH, which is a scale to express the concentration of H^+ in the solution, inversely proportional to the concentration of OH^-. Table 1 summarizes the half-reactions of HER and OER for acidic and alkaline water-splitting[111].

$2\ H_2O \rightarrow 2\ H_2 + O_2$	HER	OER
Acidic	$2H^+ + 2e^- \rightarrow H_2$	$2\ H_2O \rightarrow 4\ H^+ + 4e^- + O_2$
Alkaline	$2\ H_2O + 2e^- \rightarrow 2\ OH^- + H_2$	$4\ OH^- \rightarrow 2\ H_2O + 4e^- + O_2$

Table 1 Half-reactions of HER and OER for acidic and alkaline water-splitting.

First of all, it can be seen that in both alkaline and acidic solutions, the OER reaction involves $4e^-$ to produce one O_2 molecule, whereas the HER requires only $2e^-$ to produce one H_2 molecule. This makes the OER reaction more complex than the HER, involving multiple intermediate steps. Furthermore, the OER typically exhibits slower kinetics than the HER, requiring higher overpotentials. The electrons used to produce H_2 gas are provided from the anode, hence, the slow OER kinetics in producing O_2 and electrons is often described as the bottleneck to achieving efficient water-splitting. This is, however, not the only issue with OER, which is also found to involve corrosion processes, especially in acidic conditions, where only catalysts based on noble metals are sufficiently stable. Understanding the OER process and its effect on electrocatalyst degradation is at the core of this thesis.

The most widely accepted mechanisms for OER in acidic and alkaline solutions are reported in Table 2[111]. At low pH, where large amounts of H^+ are available in solution, OER starts from the dissociation of water (I): a surface hydroxyl intermediate ($^*OH$) is expected to form upon release of one proton, and one electron is transferred to the anode. Then, another electron is transferred to the anode and another proton is released, leaving behind an adsorbed oxygen atom ($^*O$) (II). Another water molecule is expected to react with adsorbed oxygen (III), producing adsorbed oxyhydroxide species ($^*OOH$) upon release of one proton and transfer of one electron. Finally, the oxyhydroxide species decomposes to release molecular oxygen, one proton, and transfers one electron, restoring the active site (IV). At high pH, instead, there are large amounts of OH^-, which act as main reactants (I): OH adsorbs, while one electron is transferred to the anode. Then, another OH^- is expected to react with the adsorbed $^*OH$ to form adsorbed oxygen ($^*O$), release water, and transfer one electron (II). The adsorbed oxygen will react with another OH^- to form adsorbed oxyhydroxide species ($^*OOH$) and transfer one electron (III). Finally, $^*OOH$ reacts with another OH^-, decomposing and releasing molecular oxygen, water and transferring one electron, while the active site is restored. As a universal rule, according to the Sabatier principle, the best catalyst should not bind too strongly or too weakly with such intermediates[112,113].

Acidic OER	Alkaline OER
(I) $H_2O + * \rightarrow *OH + H^+ + e^-$	(I) $* + OH^- \rightarrow *OH + e^-$
(II) $*OH \rightarrow *O + H^+ + e^-$	(II) $*OH + OH^- \rightarrow *O + H_2O + e^-$
(III) $H_2O + *O \rightarrow *OOH + H^+ + e^-$	(III) $*O + OH^- \rightarrow *OOH + e^-$
(IV) $*OOH \rightarrow * + O_2 + H^+ + e^-$	(IV) $*OOH + OH^- \rightarrow * + O_2 + H_2O + e^-$

Table 2 Proposed mechanisms for OER in acidic and alkaline solutions, "*" represents a metal active site.

In both acidic and alkaline cases, $4e^-$ are involved, and the surface pH is expected to decrease during these reactions due to the release of H^+ in the acidic case, and depletion of OH^- in the alkaline case. The main difference between the proposed mechanisms relies on the proton source: H_2O at low pH and OH^- at high pH, with a hybrid case at neutral pH values. The energy required at each intermediate step to form and break bonds determines the overpotential for OER, with one step typically being the rate-determining step, depending on the electrocatalyst.

Despite these theoretical models are useful to rationalize what is happening at the electrode-electrolyte interface, they may not capture some real-world complexities. For example, these models often do not consider the surface beyond the adsorption sites, assuming it is invariant. In realistic cases, the surface is often undergoing oxidation, reconstruction or dissolution, that might favor different intermediates or pathways. Particularly, it was shown that, for some oxides, molecular oxygen can also be produced directly from the oxygen in the oxide lattice, without following the conventional adsorbate evolution mechanism described above[9,71,114].

So far, the formation of oxygen and hydrogen gas through water electrolysis has been discussed, connected to the production of hydrogen of electrolyzers. In the case of fuel cells, hydrogen and oxygen recombine to form water, as in the following reaction:

$$2H_2 + O_2 \rightarrow 2H_2O \qquad (6)$$

Exactly as the opposite of the water-splitting reaction (reaction 1), H_2 is oxidized at the anode and O_2 is reduced at the cathode. Focusing on the ORR, oxygen can be reduced following a $4e^-$ pathway producing water, or a $2e^-$ pathway where hydrogen peroxide (H_2O_2) is the final product[115]. It is the role of the electrocatalyst to stabilize the intermediate species with the right binding energy to promote one of the two pathways. Platinum is the best elemental electrocatalyst existing for ORR, yet it requires a significant overpotential, which limits the efficiency of fuel cells.

3.3.1 Gold electro-oxidation

The use of single crystals with well-defined surfaces studied in diluted and contaminant-free electrolytes provides a controlled system that allows to relate the surface structure with the voltametric response[12,68,81]. An example of an Ar-saturated, contaminant-free CV of Au(111) measured in 0.05 M H_2SO_4 is shown in Fig. 22. Two clearly visible peaks in Fig. 22a, anodic (positive) and cathodic (negative), show up during the upward and the downward sweep, respectively. The anodic peak around 1.3 $V_{Ag/AgCl}$ is commonly associated to the oxidation of the Au(111) surface. The current does not increase exponentially, but follows a peak-like shape, suggesting that the oxidation stops when one or a few monolayers of Au are oxidized, as investigated in **Papers I-VIII**. The same peak-like shape is observed in the cathodic peak around 0.85 $V_{Ag/AgCl}$ associated to the oxide reduction. It can be noticed that the two peaks are quite well separated in potential, the thermodynamic onset of oxidation and reduction is usually found around the middle point between oxidation and reduction peaks[116]. The large overpotential observed for oxidation and reduction indicates their high irreversibility, which is attributed to slow kinetics of the processes or to the different stabilities of oxidized and reduced species.

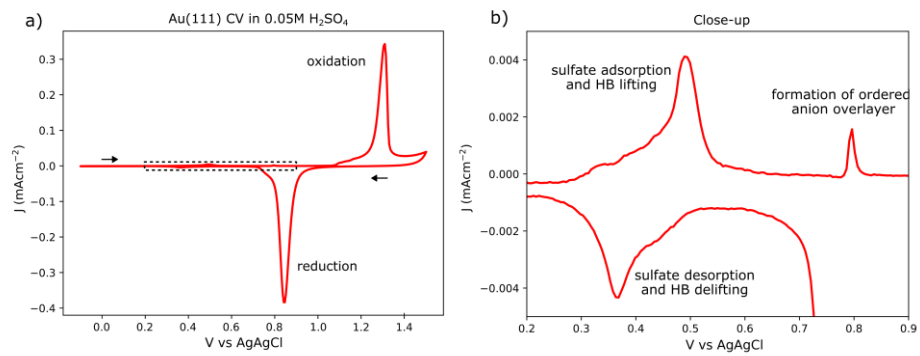

Figure 22
a) Au(111) CV in 0.05 M H_2SO_4 measured between -0.1 $V_{Ag/AgCl}$ and 1.5 $V_{Ag/AgCl}$ at 50 mV/s. b) Zoom in the region between 0.2 and 0.9 $V_{Ag/AgCl}$ defined by the dashed rectangle in (a).

At lower potentials than the oxidation/reduction peaks, almost zero-current is measured, and only small voltametric features are observed. This region is typically characterized by only a small charging of the surface that induce restructuring of the EDL, adsorption and desorption of species, etc. Figure 22b highlights the region in the dashed rectangle of Fig. 22a between 0.2 and 0.9 $V_{Ag/AgCl}$. The small current peaks observed are associated to the adsorption and desorption of sulphate and other anions around 0.5 $V_{Ag/AgCl}$ in the forward (anodic) sweep and around 0.4 $V_{Ag/AgCl}$ in the backward (cathodic) sweep, respectively[69]. During these processes, lifting and de-lifting of the Au(111) reconstruction have been shown to take place, e.g., see

Paper VI. In this case, the reactions appears quite reversible. A sharper peak is also observed around 0.8 $V_{Ag/AgCl}$ in the anodic sweep and it has been associated to the ordering of the adsorbed anions overlayer[69]. The reverse transition from reconstructed to disordered anions overlayer is expected to appear also in the backward sweep, but the cathodic current peak from the reduction of oxidized Au layers is much stronger. As previously highlighted, such details are visible and replicable only in the case of ultrapure electrolytes and well-prepared single-crystalline surfaces.

3.3.2 Platinum electro-oxidation

Figure 23a shows CVs of polycrystalline Pt for increasing UPL in Ar-saturated 0.1 M $HClO_4$ solution at 20 mV/s. Similarly to Au, a CV of polycrystalline Pt exhibits anodic and cathodic peaks around 1 V_{RHE} and 0.75 V_{RHE}, respectively, associated with oxidation and reduction of the Pt surface. The strong cathodic and anodic peaks observed at lower potentials are associated with the adsorption and desorption of hydrogen, respectively[117]. When the electrolyte is saturated with O_2 (Fig. 23b), the voltametric response is completely different. Pt is the most active elemental catalyst for ORR, hence, it will promote the reduction of oxygen dissolved in solution. As a result, the cathodic current observed in the LSV of Fig. 23b is mostly associated with ORR and possibly also to the reduction of the oxidized Pt-layers[118], as investigated in **Paper X**.

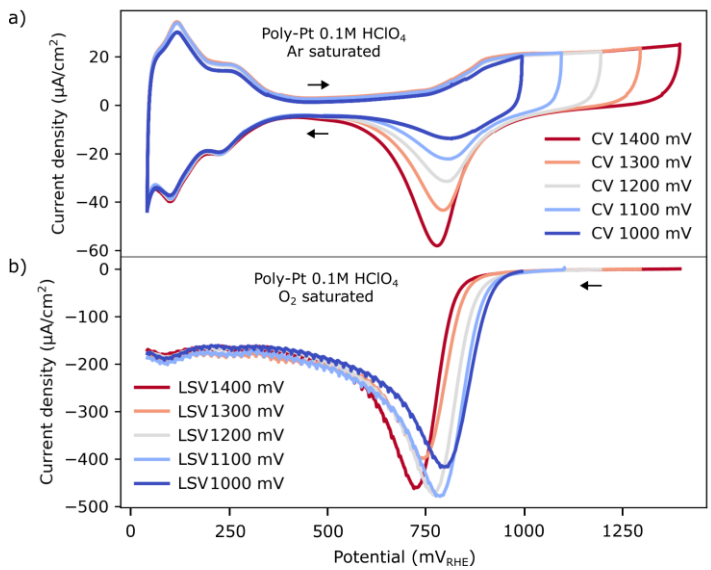

Figure 23
a) Ar-saturated CVs on polycrystalline Pt in 0.1 M $HClO_4$ at 20 mV/s for different upper potential limits. b) O_2-saturated LSV on polycrystalline Pt in the same conditions. From the supplementary material of **Paper X** in this thesis.

3.4 Passivity and corrosion

Corrosion is the main degradation process of metals, caused by chemical or electrochemical reactions with the environment that involve oxidation and dissolution of the metallic surface[104]. The capability of corrosion-resistant materials, like stainless steels or Ni alloys, to resist general corrosion, relies on their surface properties. A protective oxide or hydroxide layer of only a few nm can spontaneously form on the surface once the material is exposed to air, slowing down the oxidation and dissolution process. The so-called passive film acts as a kinetics barrier against corrosion, significantly extending the lifetime of these materials[104].

The stability of corrosion-resistant materials is commonly assessed through LSV studies, an example of LSV on a Ni alloy 59 in 1 M NaCl at pH 2 is shown in Fig. 24. In the cathodic region, the large increase of the current with more negative potentials is associated with HER. At more positive potentials, the current initially increases and then decreases, similar to what has been observed for the anodic oxidation peaks in the CV sweeps of Au and Pt (see **Sections 3.3.1 and 3.3.2**). This is the so-called "activation region", where the surface gets oxidized to form a passive protective layer of a few nm, preventing further oxidation. In fact, the current does not increase with potential for a relatively large potential window, indicating a lack of significant oxidation and dissolution. This is known as the passive region, where the material is rather stable. At sufficiently high potentials, however, a large anodic current is measured, suggesting a trans-passive behavior, typically characterized by metal dissolution and subsequent rust formation. Nevertheless, other reactions may contribute to the current and cannot be excluded *a priori*.

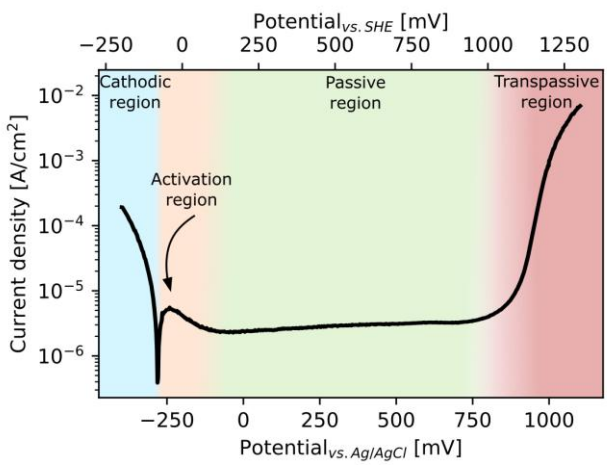

Figure 24
LSV for Ni alloy 59 in 1 M NaCl at pH 2 across the cathodic, passive and trans-passive regions.

The formation and breakdown of the passive film can be described by the point defect model[119] (PDM), which is related to the Cabrera-Mott model described in **Chapter 2.2.3**. In addition to the Cabrera-Mott model, the PDM considers the presence of defects in the oxide layer as well as the possible dissolution of the barrier layer into the electrolyte[120] (Fig. 25b). Oxygen vacancies are created at the metal/oxide interface, while cation vacancies are created at the oxide/electrolyte interface (Fig. 25b). These vacancies can move across the oxide to be filled at the opposite interface. Note that in this case, however, the potential drop across the oxide, which is the main driving force for these vacancies to move, is affected by the applied potential (Fig. 25a).

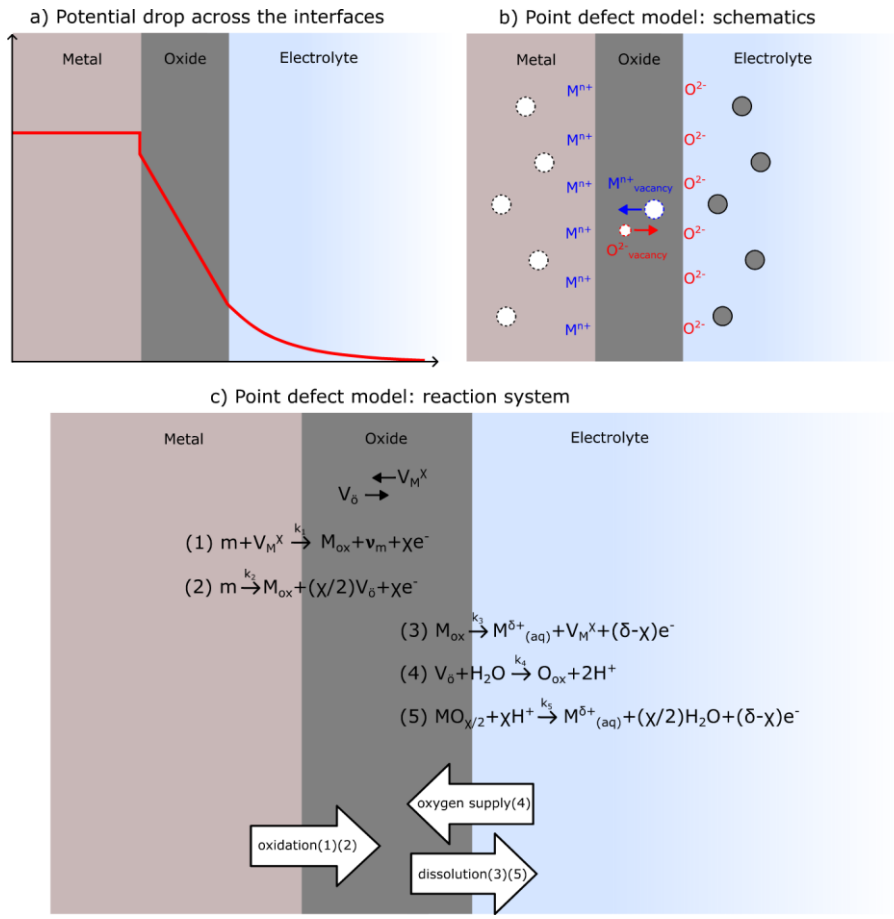

Figure 25
a) Potential drop across the interface in the presence of a surface oxide. b) Schematics of the point defect model. c) Summary of the reactions involved in the point defect model.

The most important reactions (numbered from 1 to 5) involved in this process are summarized in Fig. 25c. At the metal/oxide interface, metal atoms can oxidize and incorporate into the oxide lattice, either by filling cation vacancies (reaction 1) or creating oxygen vacancies (reaction 2). At the oxide/solution interface, oxygen vacancies may be filled by oxygen originating from water molecules, provided that water dissociation occurs at the oxide surface, or oxygen-containing ions (reaction 4). The capability to dissociate water, however, is not explicitly treated in the PDM, but can be crucial for water-splitting applications. If oxygen incorporation depends on water dissociation, the overall oxide growth rate could vary with oxide thickness as well as its catalytic properties, leading to self-limiting films similar to mechanisms proposed for gas-phase oxidation. In aqueous systems, however, self-limiting oxide growth can also result from oxide dissolution at the interface, either through cation ejection into the solution (reaction 3) or proton-induced chemical dissolution (reaction 5), with or without charge transfer.

Under an applied electric field, cation and oxygen vacancy migration across the thin oxide drives further oxidation: oxygen vacancies move outward, while cations migrate inward. A high anodic potential produces a strong field, accelerating oxide growth. As the oxide thickens, the field strength and consequently the growth rate decline, consistent with the Cabrera-Mott mechanism. Experimentally, oxide growth of common corrosion-resistant materials eventually reaches a steady-state thickness, maintained by the balance between electrochemical oxide formation and dissolution. Since chemical oxide dissolution reactions are largely potential-independent, while growth reactions are potential-dependent, the steady-state thickness typically increases with electrode potential and decreases with acidity (lower pH). Even in the passive regime, a finite passive current persists, reflecting the continuous electron transfer required to compensate for slow oxide dissolution.

At a sufficiently high anodic potential, passive film breakdown occurs, consisting of rapid dissolution and subsequent formation of a thick corrosion scale. For traditional Cr-containing corrosion-resistant industrial materials, like stainless steel, the mechanism of trans-passive breakdown is attributed to the oxidation of Cr^{3+} to Cr^{6+} in the passive film, which is unstable and dissolves. However, there can be other mechanisms influencing this behavior, depending on the composition of the passive film. As discussed in **Paper IX**, OER can play an important role in the passivity breakdown of materials that are active towards water-splitting, like Ni-based alloys, used in many industrial applications.

4. Total Reflection X-ray Absorption Spectroscopy

This chapter first briefly introduces the basics of X-ray interactions with matter and the production of synchrotron X-rays. Then, after explaining the principles of X-ray absorption spectroscopy, bulk and surface-sensitive measurement modes are described, with a focus on RefleXAFS measurements and analysis. RefleXAFS experiments can be found in **Papers I, II, VII, VIII, and X,** while traditional XAS measurements can be found in **Paper IX**.

4.1 X-rays and their interaction with matter

When we use the term "light" in everyday conversations, we are often referring to the portion of the electromagnetic spectrum that is visible to our human eyes, something that should be addressed as "visible light". Light is an electromagnetic radiation that has a very broad range of wavelengths. From radio waves to gamma rays, the wavelengths of light span from 10^{3} to 10^{-12} meters, each of them exhibiting different energies and properties (Fig. 26).

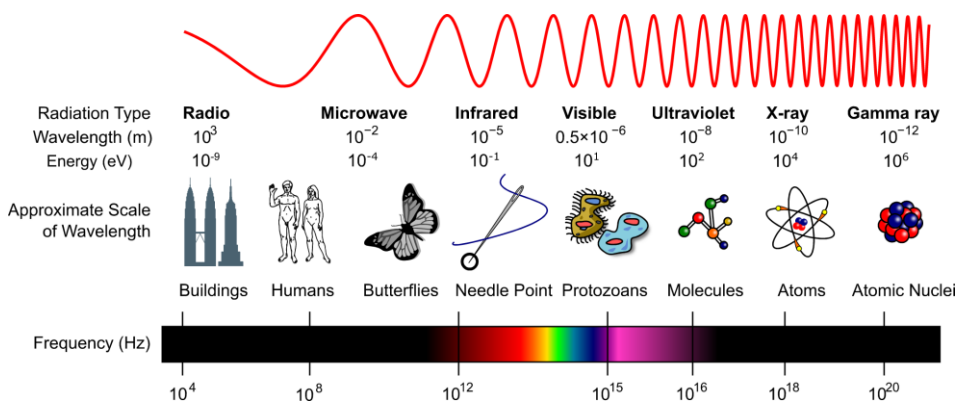

Figure 26
The electromagnetic spectrum, adapted from ref. [121], licensed under CC BY-SA 3.0.

X-rays, discovered in 1895 by the 1901 Nobel Prize winner Wilhelm Röntgen, are a type of light located at the high-energy side of the electromagnetic spectrum, with much higher energy (0.1 - 100 keV) and much smaller wavelength (0.1 Å - 10 nm) than what our eyes can detect. Due to these features, high energy X-rays have specific penetration capabilities that are exploited to reveal hidden objects in e.g. medicine diagnostics or airport security applications. Yet, this is not the only advantage that X-rays can offer; their energy range matches those of core-level electrons in the atoms, while their wavelengths are comparable to that of the interatomic distances within matter. As a result, X-ray spectroscopy methods can be used to ionize atoms and probe their chemical environment, while X-ray scattering methods can be used to determine the atomic structure of a sample through interference phenomena, like in diffraction[122].

The relation between wavelength (λ) and energy (E) of X-rays can be described as:

$$E = \frac{hc}{\lambda} \sim \frac{12.398}{\lambda[\text{Å}]}[keV] \qquad (6)$$

Where *h* it the Plank's constant and *c* is the speed of light in vacuum. X-rays with low energy are typically referred to as "soft" X-rays, while high energy X-rays are generally called "hard", but a clear cut-off energy dividing these two regions is not well-defined. In some cases, the term "tender" X-rays is used to identify a region between soft and hard X-rays. The most important distinction is that soft X-rays have lower penetration power compared to hard X-rays. Therefore, soft X-rays are more suitable to study the surface of a sample, while hard X-rays can be used to probe the bulk of the sample or to reduce attenuation through gases and liquids. As it will be discussed later in this chapter (**Section 4.4**), however, there are some cases where also hard X-rays can be made surface-sensitive, i.e., by adopting a grazing-incidence geometry.

The energy-dependent attenuation of X-rays through matter is determined by the type and likelihood to occur of an interaction between the X-ray photons and the electrons cloud surrounding the atoms[122]. For an individual atom, these interactions can be categorized into four processes: photoelectric absorption, incoherent scattering, coherent scattering and pair production. Since pair production predominantly occurs at photon energies above 1000 keV, much higher than the one used in this thesis (below 100 keV), this process will be neglected in the following discussion. The probabilities of these processes to happen are called "cross-sections" and are not only energy-dependent but also element-specific. As an example, Fig. 27a shows the X-ray attenuation cross-sections for Au calculated at photon energies between 1 keV and 1000 keV. In this energy range and especially at low energies, the total cross-section is dominated by photoelectric absorption, in which an X-ray photon is absorbed by an atom resulting in an excited state. This excited state has a short life-time, quickly relaxing upon emission of either an X-ray

photon (see **Section 4.3.1**) or an Auger electron (see **Section 5.4.3**). The cross-section for the absorption process is approximately proportional to Z^4, where Z is the atomic number, and to $1/E^3$, where E is the photon energy. However, as can be seen in Fig. 27a, sudden "jumps" and additional features in the absorption cross-section can be observed at specific energies, more details about these features and the applications of this process to X-ray absorption spectroscopy will be discussed later in this chapter (**Section 4.3**).

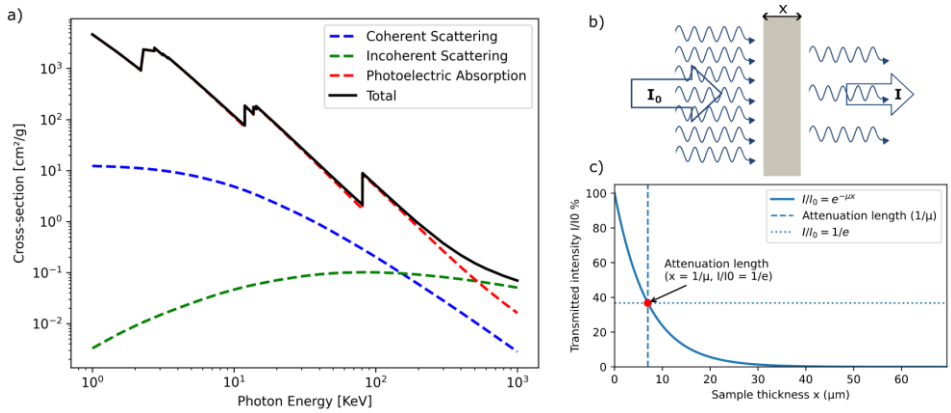

Figure 27
a) Calculated X-ray attenuation cross-section for Au from ref. [123]. b) Attenuation of an X-ray beam through a sample with homogeneous thickness *x* and linear absorption coefficient *μ*. The incident beam intensity is I_0 and the transmitted intensity is *I*. c) The transmitted intensity *I* as a function of sample thickness *x* according to the Beer-Lambert law.

Apart from being absorbed, the X-ray photon can instead be scattered by an atom, i.e., it can change its direction of propagation. In the case of inelastic (incoherent) scattering, the energy of the scattered photon is not conserved, and part of the energy is transferred to the scatterer. In the case of elastic (coherent) scattering, on the other hand, the energy remains unchanged during the process. Up to roughly 100 keV (for Au), coherent scattering is the second largest contribution to the total cross-section, although is lower by several order of magnitudes compared to absorption. Elastic scattering is crucial for diffraction studies, as it will be further discussed in the next chapter (**Section 5.2**).

Given an X-ray beam with fixed energy, travelling through a slab of material with a homogeneous thickness *x* and linear absorption coefficient μ (Fig. 27b). We can use the Beer-Lambert law to describe the intensity decay through the slab due to photoelectric absorption, as follows:

$$I = I_0 e^{-\mu x} \quad (7)$$

This formula shows that the intensity of the X-ray beam decays exponentially as it penetrates through the material, falling to 1/e of its original value ($I/I_0 \sim 37\%$) when the travelling path x equals μ^{-1}, defined as the absorption length (Fig. 27c). The linear absorption coefficient μ is the most important term of this formula and depends on the element or composition of the sample and on the energy E of the X-ray beam, as follows:

$$\mu(E) = 2k(E)\beta(E) \qquad (8)$$

Where $k(E)$ is the wave-vector of the X-ray beam, calculated as:

$$k(E) = \frac{2\pi E}{hc} \qquad (9)$$

And $\beta(E)$ can be calculated as:

$$\beta(E) = -\frac{2\pi r_0 \rho_{at}}{[k(E)]^2} f_2(E) \qquad (10)$$

Where r_0 is the Thomson scattering length and ρ_{at} is the atomic density of the material. $f_2(E)$ belongs to the imaginary part of the atomic scattering factor:

$$f = f_1 + if_2 = f_0 + f' + if'' \qquad (11)$$

Plots of tabulated $f_1(E)$, $f_2(E)$ and of $\mu(E)$ calculated using equation 8 are shown in Fig. 28.

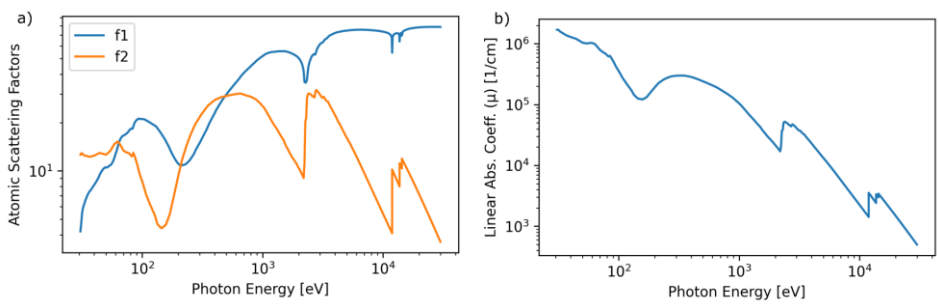

Figure 28
a) Tabulated atomic scattering factors f_1 and f_2 of Au from ref. [124]. b) Calculated linear absorption coefficient of Au according to eq. 8.

From a macroscopic point of view, $i\beta(E)$ represents the imaginary part of the complex refractive index $n(E)$ of the material:

$$n = 1 - \delta + i\beta \qquad (12)$$

The imaginary part $i\beta(E)$ of the complex refractive index is due to photoelectric absorption and inelastic scattering, while the real part $1-\delta$ is due to elastic scattering, where $\delta(E)$ can be calculated as:

$$\delta(E) = \frac{2\pi r_0 \rho_{at}}{[k(E)]^2} f_1(E) \qquad (13)$$

Where $f_1(E)$ is the real part of the atomic scattering factor. Hence, the complex refractive index (eq. 12) describes both dispersion and absorption of X-rays in matter. The real and imaginary components are not independent but are linked through the Kramers-Kronig dispersion relations, consequently, absorption features in $\beta(E)$ produce corresponding dispersive variations in $\delta(E)$, which strongly influence the energy dependence of X-ray reflectivity[27,28].

4.2 Synchrotron radiation and beamlines

In a traditional X-ray laboratory for e.g. diffraction experiments or for computed tomography scans, the X-ray source typically consists of a target component bombarded with electrons, accelerated through an electric field. A small part of the electron beam energy is converted into X-rays via two processes: the deceleration of electrons within the target generating X-rays with a broad and continuous energy range (Bremsstrahlung radiation) and the emission of characteristic X-rays with specific energies, depending on the target material, via the fluorescence process (Fig. 29)[122]. This type of technology has some important limitations regarding the intensity, beam focus and energy resolution that can be achieved. In the 1960s-70s it was realized that the synchrotron radiation emitted from charged particles circulating in a storage ring was potentially much more intense and versatile.

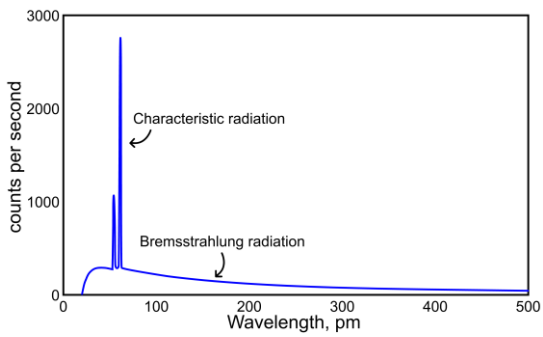

Figure 29
Example of an emission spectrum from a traditional X-ray lab source. The broad background is characterized by the Bremsstrahlung radiation, while the sharp distinct characteristics peaks are emitted via fluorescence process, whose energy depends on the target material. Adapted from ref. [125] licensed under CC0 1.0.

Modern synchrotrons are large-scale facilities where relativistic electrons travel at near-light speed in vacuum and are forced to follow curved trajectories using bending magnets. This process stimulates the generation of X-rays, similarly to the Bremsstrahlung radiation, but with a much higher brilliance. The brilliance is a common figure of merit used to define the quality of an X-ray source[122], as follows:

$$Brilliance = \frac{\Phi(\lambda)}{(2\pi)^2 \varepsilon_h \varepsilon_v} \left[\frac{Photons/second}{(mrad)^2 (mm^2\ source\ area)(0.1\%\ BW)}\right] \quad (14)$$

Where $\Phi(\lambda)$ is the photon flux, ε_h and ε_v are the emittance in the horizontal and vertical directions, respectively, determined by both the beam size and its divergence. This means that the brilliance is proportional to the number of photons per second per square millimeter of area per square milliradian of solid angle within a bandwith of 0.1% of any given energy. A third-generation synchrotron can achieve a brilliance up to 10 orders of magnitude higher than that from a home-lab X-ray source. A schematic illustration of the main components of a synchrotron facility is shown in Fig. 30.

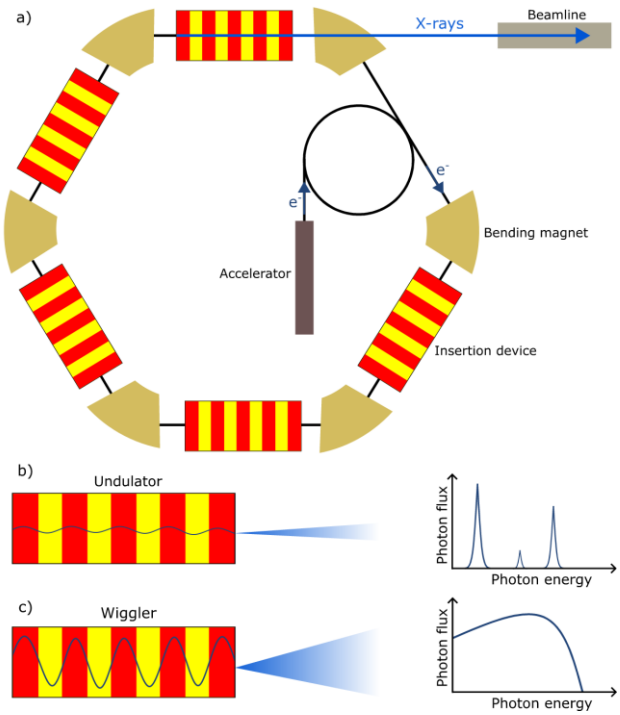

Figure 30
a) Schematic overview of a synchrotron radiation source, with bending magnets and insertion devices. The main difference between b) undulator and c) wiggler insertion devices is highlighted.

As shown in Fig. 30a, electrons are first generated with an electron gun and then accelerated in a linear accelerator to reach a certain energy (a few GeV or more) before being injected into the storage ring. After injection, the electrons travel along a ring-like polygon (storage ring) thanks to bending magnets that accelerate them towards the center of the ring. As a result of the change in acceleration, electrons emit broad-spectrum X-rays that depend on the curvature of the path, i.e. the strength of the magnetic field. The possibility to tune the energy of X-rays is essential to perform X-ray absorption spectroscopy experiments and can make other X-ray based experiments more versatile. A more efficient way than bending magnets to produce broad spectrum X-rays is to use a wiggler, which consists of a series of magnets with opposite polarities placed in a row (Fig. 30c). This device forces the electrons to "wiggle" back and forth producing more X-ray radiation than a bending magnet, significantly enhancing the brilliance. If having a continuous energy spectrum is not what is needed in an X-ray experiment, as for example in X-ray diffraction or X-ray photoelectron spectroscopy, an undulator can be used (Fig. 30b). This device is still composed by rows of magnets with opposite polarities, but the deflections caused by an undulator are small enough that the X-rays emitted from each turn overlap and interfere. At some energies, constructive interference causes a drastic increase in the intensity, while at other energies the intensity is almost cancelled out. For both a wiggler and an undulator, which were introduced with the third generation of synchrotrons, the divergence is much smaller than for bending magnets. Yet, the smallest divergence is provided by undulators, thanks to the smaller magnetic field employed. The beam divergence from the insertion device is very important especially when it comes to achieve a tightly focused beam, but it is always the combination of insertion devices and beamline optics that define the real capabilities of a particular beamline.

A beamline is built tangent to the ring, and it is where the X-rays are conveyed to carry out the experiment. Prior to the endstation, where the sample is finally illuminated by X-rays, a system of optical components is used e.g. to focus the beam (using mirrors), to discard photons not in the desired energy range (using monochromators) or even to be attenuated and slitted down, if needed. As a result, synchrotron beamlines can provide intense monochromatic radiation with tunable energy (from UV to more than 100 keV), focused down to even nano-sized spots. This allows many types of experiments, and each beamline is usually specialized for a few of them. Most of the experiments presented in this thesis were performed at MAX IV[126–128] (Lund, Sweden) (**Papers II, III, IV, V, VII, VIII, IX, X**) and PETRA III, DESY[129,130] (Hamburg, Germany) (**Papers I, V, IX**). MAX IV was the first 4th generation synchrotron facility in the world, characterized by the implementation of a diffraction-limited storage ring[30] (DLSR) for hard X-ray experiments. It employs a multi-bend achromat lattice with a denser array of magnets to better control the size and divergence of the electron beam, directly enhancing the brilliance.

As an example of a beamline configuration, Fig. 31 shows the optics of the Balder beamline[131] at MAX IV, where *operando* time-resolved RefleXAFS experiments were performed. Note that Balder is the only beamline presented in this thesis that uses a wiggler as an injection device.

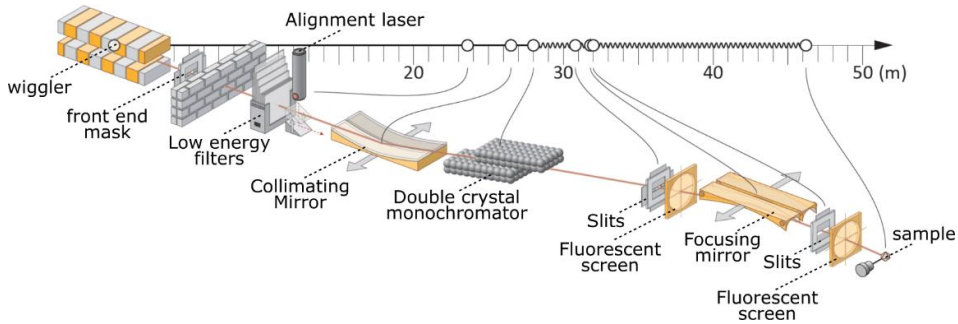

Figure 31
Conceptual optical layout of the Balder beamline at MAX IV, where the beam from the storage ring can be tailored for e.g. RefleXAFS experiments. Adapted from ref. [131].

4.3 Principles of X-ray Absorption Spectroscopy

Before discussing how to measure X-ray absorption spectra experimentally in different modes, a brief introduction to the fundamentals of X-ray absorption spectroscopy (XAS) is given. XAS, also known as X-ray absorption fine structure (XAFS) spectroscopy, is used across many fields, from biology to geology and environmental sciences, to probe the electronic and local atomic structures of different species within a material. XAS can reveal the chemical environment, oxidation state, coordination number and average atomic distances surrounding atoms of a specific element in a sample[132]. This technique is based on the photon absorption process, where an X-ray photon is absorbed by an atom and transfers all its energy to an inner-shell electron, which is excited to a higher energy state below or into the continuum, generating a core-hole (Fig. 32a). For a core electron to be excited and thus to participate in the absorption process, it is necessary that its binding energy is equal or lower than the energy of the incoming photon. Hence, each element will exhibit sudden "jumps" in the absorption cross-section at specific energies where this condition is satisfied (Fig. 32b). These "jumps" in absorption probability are called absorption edges and depend on the specific electronic structure of an element, as well as its chemical environment, oxidation state and coordination geometry. Based on this, X-ray absorption near edge structure (XANES) spectroscopy focuses on the signal, proportional to the absorption

coefficient, measured across a specific absorption edge, as in the yellow region of Fig. 32c. XANES can be used as a chemical and structural fingerprint of the absorbing atoms, often analysed in comparison to reference XANES spectra. This thesis focuses on studying the XANES region of Au, Pt and Ni alloys, in particular to follow their oxidation process and decipher their chemical environment.

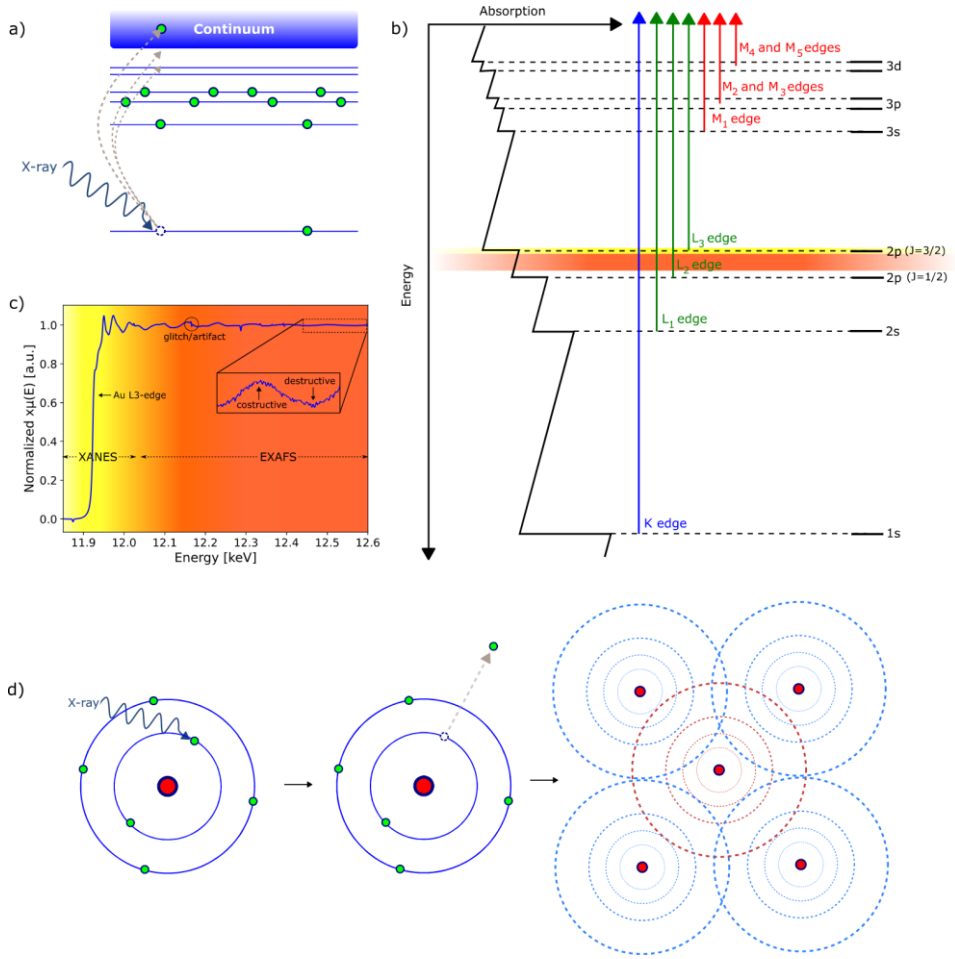

Figure 32
a) A schematic energy level diagram of the photon absorption process. b) Example of transitions and corresponding absorption edges of an atom, adapted from ref. [133], under license CC BY-SA 3.0. This process has a limited lifetime and will relax either through X-ray fluorescence or Auger emission processes, discussed in **Sections 4.3.1 and 5.4.3**, respectively. c) Example of a XAFS spectrum measured from a Au sample at the Au L3-edge. d) Visualization of the EXAFS process.

At higher photon energies, above the absorption edge, the photoelectrons are excited in the continuum through the photoelectric process, as described in more detail in

Section 5.1. In this energy region, the photoelectrons have sufficient energy to be ejected by the ionized atom and to interfere with the surrounding atoms, causing constructive and destructive interference in the absorption signal (red region in Fig. 32c). The study of this region in the XAFS spectrum is called extended X-ray absorption fine structure (EXAFS) spectroscopy and can provide information on the local distances between the absorbing atom and the neighboring scatterers (Fig. 32d). A critical advantage of this method to obtain structural information compared to X-ray diffraction is that there is no requirement for long-range atomic periodicity, since the structural information comes from the local environment surrounding the absorbing atoms.

4.3.1 Traditional measurements

XAS experiments are extremely versatile; they can be performed relatively easily on, e.g., liquid solutions, powders, foils, etc. One of the main advantages of XAFS for *operando* studies is the possibility to perform measurements based on photon-in/photon-out processes. In this way, measuring photoelectrons can be avoided, which have lower energies and undergo higher attenuation through dense media. The XAS experiments performed in this thesis did not require any UHV system, hard X-rays can penetrate air and liquids without undergoing strong attenuation. The energy region of the X-ray photons chosen for the experiment, however, depends on the absorption edge energies of the material, which limits the range of elements that can be studied in this environment. For low-Z elements, where soft X-rays are used, other methods such as total scattering should be explored[134].

Traditionally, XAFS can be measured in transmission or fluorescence mode[132]. In the first case, the transmissivity of the sample as a function of the X-ray energy, i.e. the ratio between transmitted and incident beam intensities, is measured (Fig. 33a). Both incident and transmitted intensities are usually measured with ionization chambers, which consist of gas-filled chambers that measure the electrical charge produced when the X-rays ionize the gas. This is the most straightforward measurement mode, but the sample must be thin enough not to completely attenuate the beam, as indicated by the Beer-Lambert Law.

For thicker samples, the X-ray fluorescence (XRF) signal as a function of incident beam energy can be measured instead. The XRF process is based on the relaxation of the atom from an excited state upon photon absorption. The core-hole generated through photon absorption is filled with an electron from an outer-shell at a higher energy level. The electron loses energy during this relaxation process by emitting a photon (called secondary or fluorescent X-ray) and the energy difference between these two electronic states corresponds to the energy of the emitted photon (Fig. 33b). The XRF intensity as a function of the X-ray energy is proportional to the absorption probability, hence, it can be used to measure the absorption coefficient, although for too thick and dense samples, there can be deviations that complicate

the measurements. Another relaxation process can take place instead of XRF, which is the emission of an Auger electron, discussed in **Chapter 5**. An example of XAS measurements in fluorescence mode can be found in **Paper IX**, where *in situ* XANES was used to probe the chemistry of dissolved products during OER on Ni alloy 59.

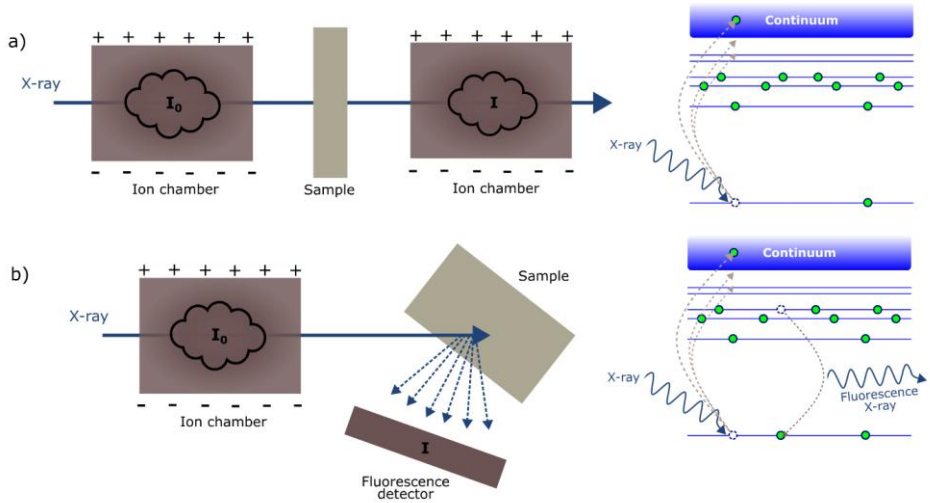

Figure 33
Schematic representations of bulk-sensitive a) transmission mode XAS measurements and the photoelectric absorption process and b) fluorescence mode XAS measurements based on the X-ray fluorescence emitted after photoelectric absorption.

4.4 Surface-sensitive measurements

Transmission mode measurements are inherently bulk sensitive, since the X-ray beam must penetrate the material. Measurements can be made more surface-sensitive by adopting a grazing-incidence (GI) geometry[122], where the X-ray beam impinges on the surface at a shallow angle, and measuring the fluorescence signal or the reflected beam intensity (Fig. 34). As discussed below, for flat, reflective substrates, the surface sensitivity is maximized in the case of total external reflection, at very small incident angles. While the surface sensitivity in total reflection conditions is theoretically the same for both fluorescence-mode GI-XAFS and RefleXAFS, it is challenging from an experimental point of view to avoid bulk fluorescence signal contributions from surface defects or facets of realistic samples and, in the case of thick samples (like single crystals or industrial alloys), from even

a small portion of the incident beam not being focused on the sample surface. Additionally, in *operando* studies, it can sometimes be difficult to find a suitable position for the fluorescence detector next to the surface while using a rather bulky electrochemical cell. An alternative to fluorescence-based GIXAFS in total reflection is to perform RefleXAFS measurements, which consist of measuring the totally reflected beam as a function of the incident beam energy. Through a set of slits that define the angular acceptance, only the photons that are totally reflected from the surface are detected, hence, the surface sensitivity can be maximized, independently on the sample thickness. An example of GI-XANES measurements performed in fluorescence mode can be found in **Paper IX**, while examples of RefleXAFS measurements can be found in **Papers I, II, VII, VIII, and X**.

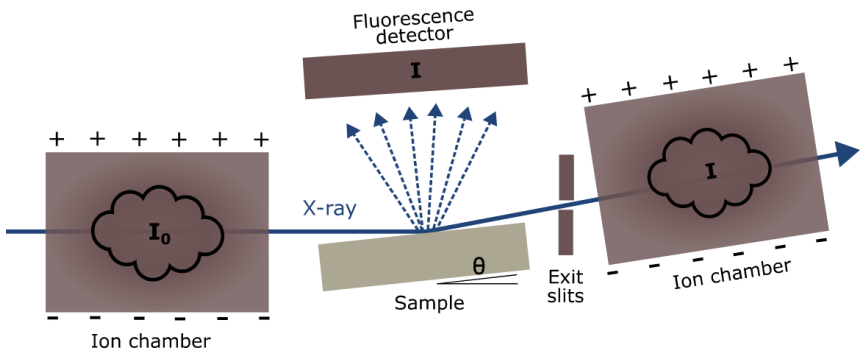

Figure 34
Schematic representation of surface-sensitive GI-XAFS measurements in fluorescence mode or measuring the reflected beam (RefleXAFS). The incident beam impinges on the surface at an angle θ and the fluorescence or reflected beam intensities are measured as a function of the incident beam energy.

The refractive index (eq. 12) links the grazing incidence angle with the X-ray penetration depth, which determines the surface sensitivity. For most materials, δ and β are usually in the order of 10^{-5} and 10^{-6}, respectively, meaning that $n < 1$. As a result, total external reflection conditions can be achieved when X-rays travel from a medium with n closer or equal to 1, e.g. vacuum, air or water, towards any investigated material in this thesis. Total external reflection means that the reflectivity of the surface (the ratio between reflected and incident beam intensities) is ideally 100%, i.e. the beam is completely reflected and only interacts with the topmost atomic layers of the sample surface. However, this phenomenon is only possible for a perfectly flat surface and, most importantly, if the grazing incidence angle of a tightly focused X-ray beam is set below a critical angle of a few mrad. The Snell's law of refraction can be used to calculate the critical angle α_c for total external reflection[122], as follows:

$$\alpha_c \cong \sqrt{2\delta} \qquad (15)$$

As a result of total external reflection, an evanescent wave propagates along the surface and its intensity decays exponentially towards the bulk. The surface sensitivity drastically increases, reaching a penetration depth of a few nm (Fig. 35).

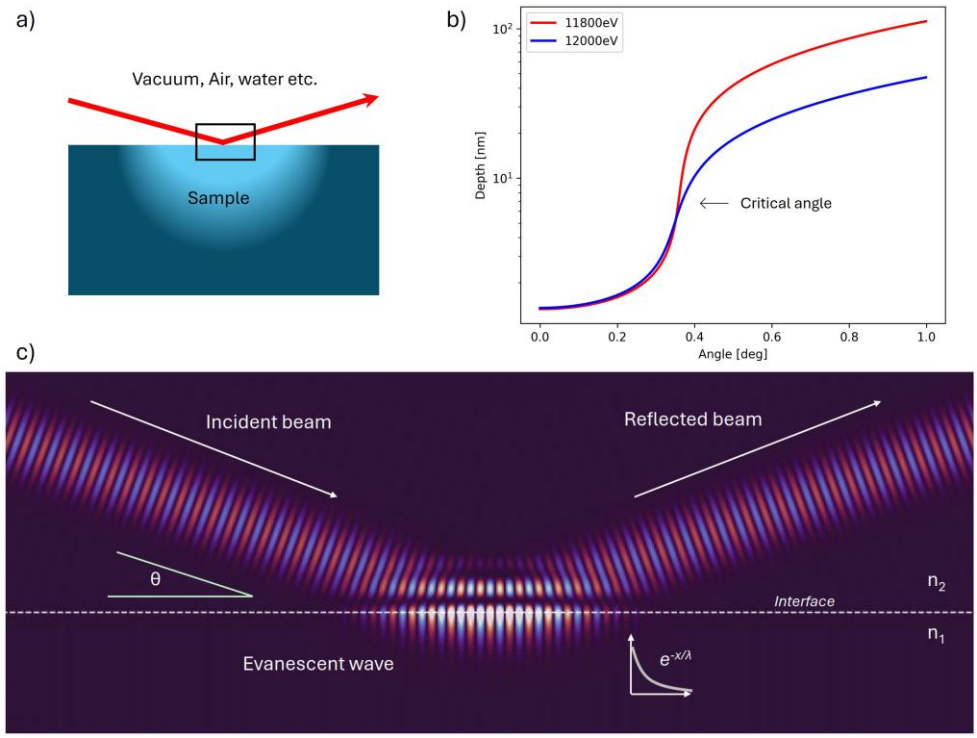

Figure 35
a) An X-ray beam impinging at a grazing incidence angle on a sample. In the case of total external reflection where ideally 100% of the beam is reflected, the black box highlights the interface region where this happens, as shown in (c). b) X-ray penetration depths calculated for a perfectly flat Au substrate at the interface with vacuum for beam energies 11.8 keV and 12 keV, from ref. [135]. The values drop to around 1.36 nm when the angle θ is set below the critical angle (~0.32 deg). c) Schematic of the evanescent wave forming at the surface in total external reflection conditions (Courtesy of L.R. Merte).

In total reflection conditions, when the energy of the X-rays is close to an absorption edge, the contribution of the imaginary part of the refractive index $\beta(E)$ is not negligible due to resonance effects related to photoelectric absorption phenomena[122]. As a result, the intensity changes of the totally reflected beam when the energy varies across an absorption edge primarily reflect XAFS features and can be used as a fingerprint of the chemistry and structure of the surface. An example of *ex situ* raw RefleXAFS measurements on a Pt(111) single crystal for different incident angles is shown in Fig. 36. At high incident angles, surface sensitivity decreases, and major deviations from traditional XAFS features are observed.

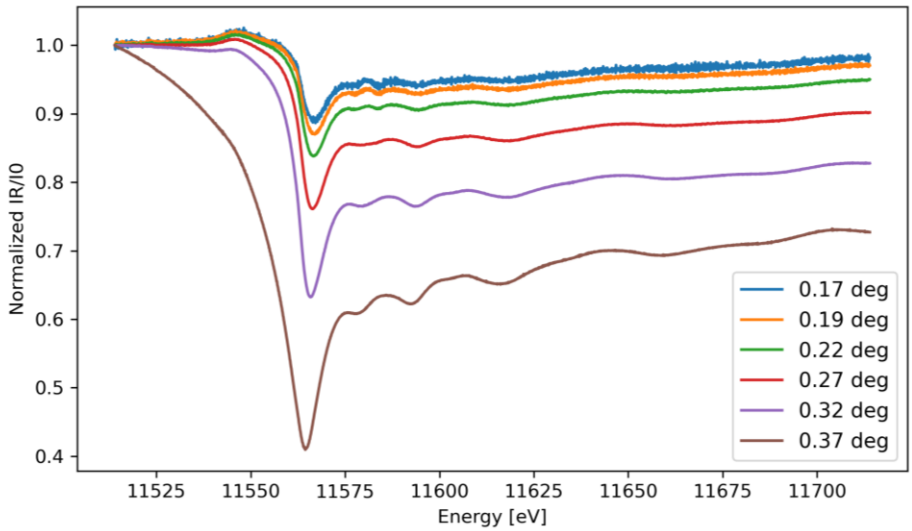

Figure 36
Ex situ raw RefleXAFS spectra measured at Balder for different incident angles on Pt(111).

In this thesis, RefleXAFS is used for a qualitative analysis of the surface chemistry and its oxidation/reduction in *operando* conditions. A detailed quantitative analysis of the RefleXAFS data could provide information on e.g. the surface roughness and thickness of the surface oxides but requires advanced mathematical modelling of the reflectivity[24] that is beyond the scope this thesis, focused on the experimental work. The qualitative analysis of RefleXAFS mainly consists of normalizing the reflectivity with the same procedure used for standard XAFS measurements and comparing it with XAFS references measured in transmission mode. Furthermore, the RefleXAFS results have been combined and compared experimentally with other techniques, in particular AP-XPS, 2D-SOR and SXRD, to support and complement the findings.

An example of a raw spectrum measured on a Au(111) single crystal using our *operando* setup is shown in Fig. 37a. The measured reflectivity (I_R/I_0) exhibits a dip and additional resonance features across the Au L_3-edge, with a background that increases with energy due to the increasing penetration of the X-rays through the electrolyte. As for traditional transmission-mode XAS data analysis, the pre-edge and post-edge backgrounds are subtracted from the $\ln(I_0/I_R)$ (Fig. 37b) and finally the edge-step is normalized to 1 (Fig. 37c). Normalized RefleXAFS spectra are called μ' to make a distinction with the actual absorption coefficient μ. Examples of normalized RefleXAFS spectra measured *operando* on Au(111) during CV are shown Fig. 37d, showing a "whiteline" increase around 11925 eV and additional XAFS changes at higher energies, associated with surface oxidation, e.g., see **Paper VII**. These spectra changes can be highlighted by plotting the difference-spectra

(Fig. 37e), used for a comparison with reference XANES spectra or to follow the relative changes between spectra at different potentials.

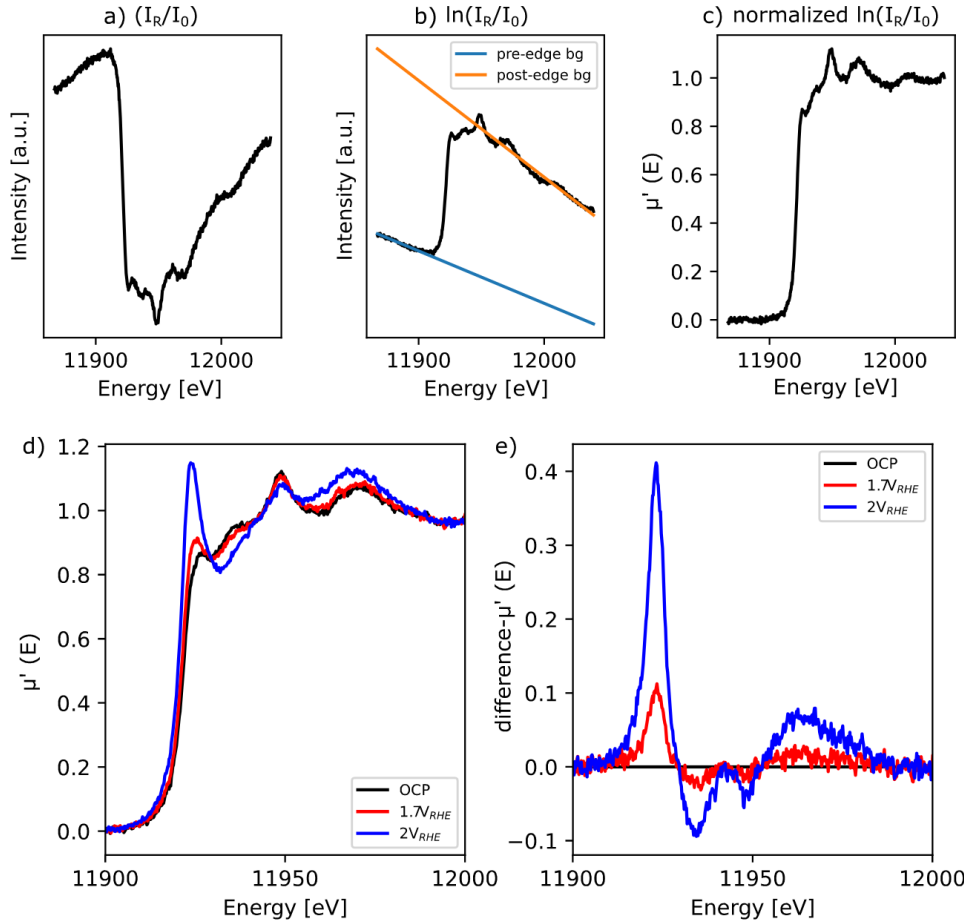

Figure 37
a) Examples of a raw RefleXAFS spectrum measured in *operando* conditions on Au(111). b) The background subtraction procedure consists of taking the logarithm of the raw data and subtract the post- and pre-edge background, followed by a normalization of the absorption edge step to one. c) normalized RefleXAFS spectrum. d) Example of normalized RefleXAFS spectra measured on gold during electrochemical oxidation in 0.05 M H_2SO_4, from **Paper VII**. e) Difference RefleXAFS spectra where the spectrum measured at OCP in (d) is subtracted from the remaining spectra shown in (d).

At Balder, *operando* RefleXAFS was used to perform surface-sensitive absorption spectroscopy while the sample was completely submerged in the electrolyte and under electrochemical potential control. In particular, surface oxidation and reduction dynamics of a Au(111) single-crystal (**Papers II, VII, VIII**) and Pt polycrystal (**Paper X**) electrodes during sweep voltammetry were monitored. The

results from the electro-oxidation of Au(111) were also compared with 2D-SOR (**Papers II and VI**), AP-XPS (**Papers IV and VII**) and SXRD (**Paper VI**). A photo of the Balder setup for RefleXAFS is shown in Fig. 38a, where the electrochemical cell shown in Fig. 19a was used. During the experiment, the incident beam was focused on the sample in a way that the beam footprint was smaller than the sample size. This configuration enables us to maximize the totally reflected beam intensity, while the angular acceptance was set by motorized vertical slits placed between the sample and a tilted ionization chamber, which was used to measure the totally reflected beam intensity.

Operando RefleXAFS was also performed at the P64 beamline of PETRAIII, DESY using the same electrochemical cell of Balder, but in this case the experiment was always performed at a fixed potential and with a de-focused beam, and the totally reflected beam was measured with a photodiode and slits taped in front of it with a fixed gap (**Paper I**). Here, the electro-oxidation of a Au polycrystal and the corrosion of a Ni alloys during OER were investigated, a photo of the P64 setup for RefleXAFS is shown in Fig. 38b. The RefleXAFS results of Ni alloy 59 were compared with AP-XPS results in **Paper IX**. Furthermore, at P64, XAS experiments in fluorescence modes through the electrolyte and at grazing incidence on the corroded samples were also performed on Ni alloy 59, to detect the dissolved species and corrosion products (**Paper IX**).

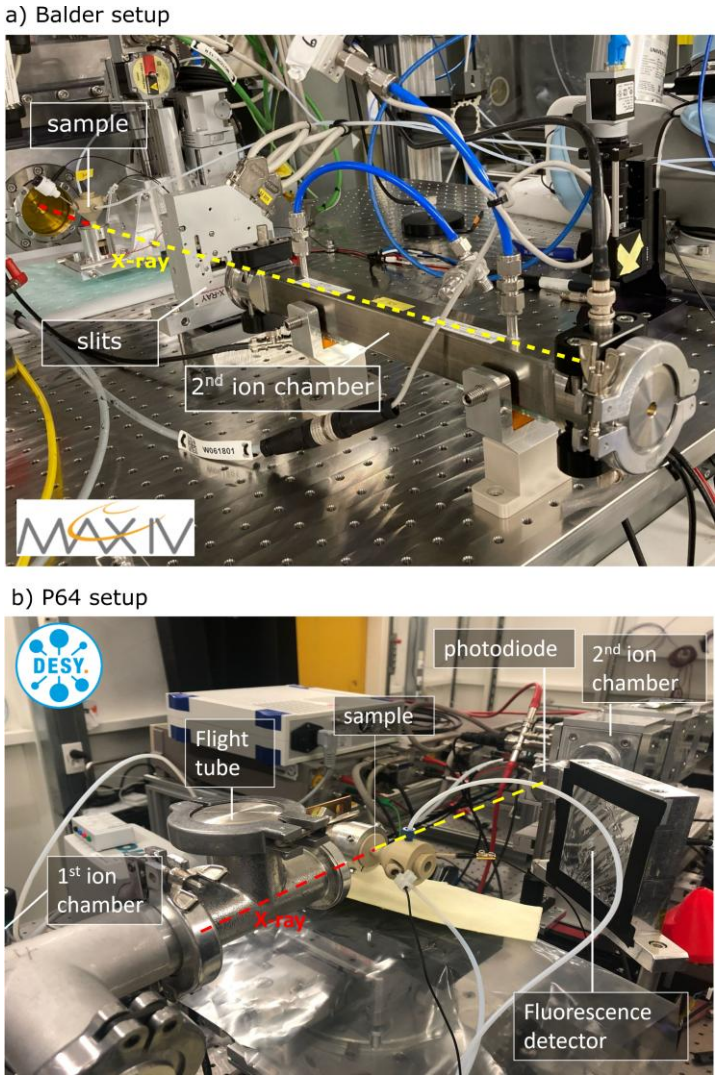

Figure 38
Photos of the RefleXAFS setups at a) the Balder beamline of MAX IV (Lund, Sweden) and b) the P64 beamline of PETRAIII, DESY (Hamburg, Germany).

4.4.1 Beam-induced effects during RefleXAFS measurements

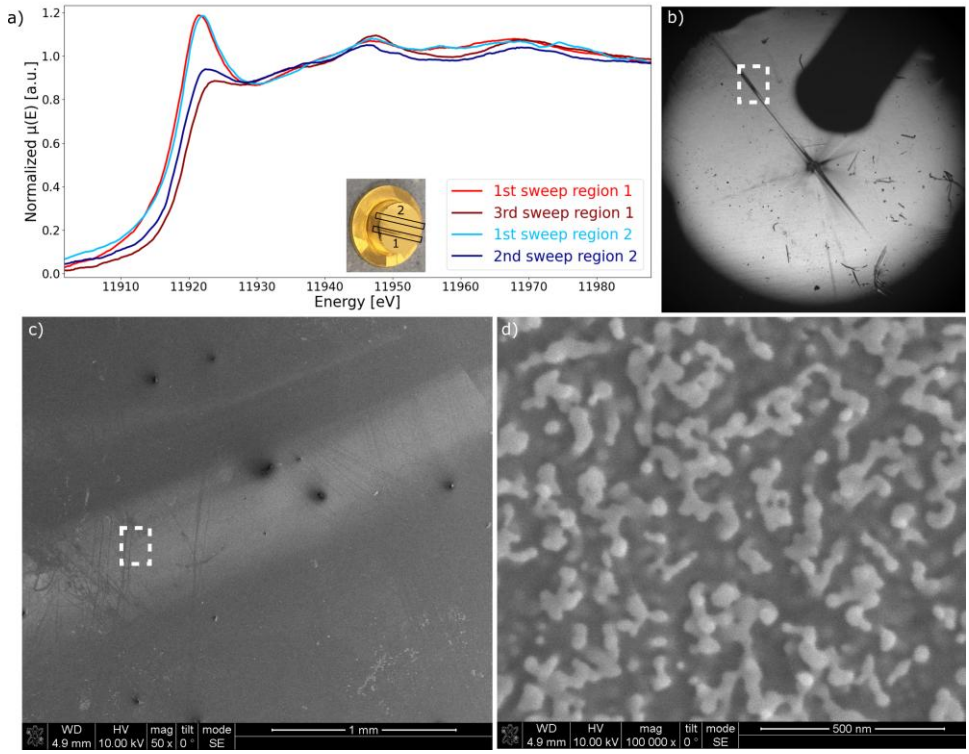

Figure39
a) Consecutive RefleXAFS Au L3-edge spectra measured on two surface regions of a polycrystalline gold sample during electrochemical polarization at ~2.3 V_{RHE} in 0.05 M H_2SO_4. b) Example of a 2D-SOR image of the sample surface (~7.5 cm in diameter) where beam damage is visible along the beam footprint (e.g. dashed white square). b) SEM image of the sample surface and c) Zoomed in SEM image of the damaged area, indicatively from the dashed white square in (c). From **Paper I**.

During the RefleXAFS measurements at P64 (DESY) (**Paper I**), beam-induced effects were observed while studying the electrochemical oxidation of Au during OER at electrochemical potentials above 2.2 V_{RHE}. In these conditions, the surface (hydr)oxide signal was decreasing over time (Fig. 39a) and a black stripe along the beam footprint was visible with 2D-SOR (Fig. 39b). To further prove that this was an effect of long exposure under the beam, a fresh region of the sample surface was measured, showing that the (hydr)oxide signal was restored. Continuous exposure of the new region to the beam produced the same effect again; this process was not observed at lower potentials. After the experiment, scanning electron microscopy (SEM)[136] showed that the damaged region (along the beam footprint Fig. 39c) had a completely different morphology (Fig. 39d). One explanation for this phenomenon

is that the X-ray beam was directly photo-reducing the (hydr)oxide, evidence of X-ray induced photo-reduction of ions has also been reported in previous literature[137]. If the sample cannot be moved continuously across the beam, it might help to spread the beam over a larger surface area to reduce the exposure of a given region. (Hydr)oxide reduction might also be induced by the secondary electrons emitted from the electrolyte and the sample upon ionization, enhanced by a cascade effect[138]. In this case, minimizing the volume of irradiated electrolyte can help decreasing beam-induced effects.

5. Complementary techniques

In this chapter, the basic principles and implementations of additional techniques used besides RefleXAFS are briefly described, i.e., *operando* 2D-SOR (**Papers II, V, VI**) and SXRD (**Paper V**), *in situ* AP-XPS (**Papers IV, V, VII, IX**) and finally *ex situ* XPS, STM, Auger Electron Spectroscopy (AES) and Low Energy Electron Diffraction (LEED) using an electrochemistry-to-UHV transfer system (**Paper III and VII**). Using complementary techniques was important for validating and comparing RefleXAFS measurements with more established quantitative methods and for providing further insights into the electrochemical properties of the model electrodes.

5.1 X-ray Photoelectron Spectroscopy

XPS is a powerful technique used in surface science to study the chemical composition, oxidation states and electronic properties of a surface. This technique is based on the photoelectric absorption process, introduced in **Chapter 4**, and focuses on the detection of the photoelectrons ejected from a core-shell into the continuum upon photon absorption (Fig. 40a). The kinetic energy E_k of the photoelectrons is measured using an hemispherical electron analyzer and depends on the binding energy (BE) E_b of the core-level, the incoming photon energy (PE) $h\nu$ and the workfunction of the surface Φ[139], i.e., the energy to remove an electron from a solid surface into vacuum:

$$E_k = E_b - h\nu - \Phi \qquad (16)$$

The photoelectric principle was introduced by Albert Einstein in 1905[140], for which he received the Nobel Prize in 1921. After calibrating the BE by measuring the Fermi level or a well-defined core-level, a plot of the intensity of the signal versus the BE can be obtained (Fig. 40b). From these spectra, it is possible to identify the elements present in the near-surface region of the sample, since the core-level BEs are element-specific. Binding energies are also sensitive to the chemical environment of the photo-electron emitting atom[141]. This means that we can observe a shift in BE due to e.g. the changes in the chemical surroundings of the photo-electron emitting atom. A careful analysis of these spectra can also provide quantitative information on the amount and composition of these phases[142].

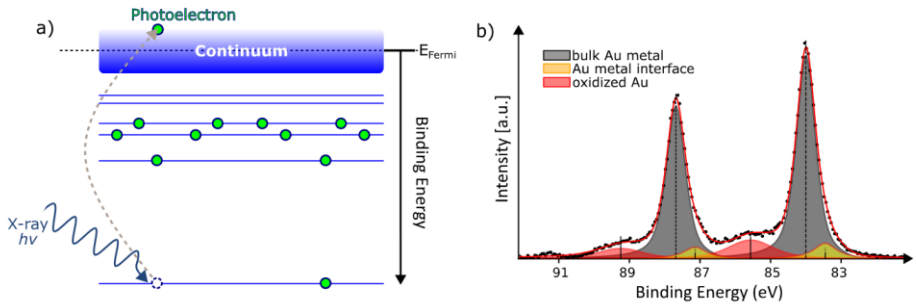

Figure 40
a) Energy level diagram representing the ejection of a photoelectron into the continuum and creation of a core-hole due to absorption of an X-ray photon. The zero of the BE is set to the Fermi Level (E_{Fermi}). b) An example of a normalized, background-subtracted and fitted Au 4f AP-XPS spectrum from **Paper VII** measured at ~13 mbar of water vapor on gold after dipping it into a 0.05 M H_2SO_4 electrolyte. The Au 4f components are assigned to metallic gold, oxidized gold and undercoordinated metallic atoms at the metal/(hydr)oxide interface.

Electrons interact more strongly with matter compared to photons and, especially at low energy, they cannot travel far through a solid. The high surface sensitivity of XPS is given by the short inelastic mean free path (IMFP) of electrons[143]. The IMFP (λ), indicates the average distance an electron can travel through a solid before being inelastically scattered. The empirical universal curve for the IMFP of electrons is shown in Fig. 41 and is used as an approximation of the real IMFP.

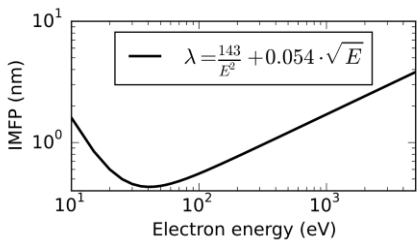

Figure 41
Universal curve of the IMFP (λ) of electrons as a function of their kinetic energy. At these values, the signal has already decayed to ~37% of its original intensity and at 3λ the signal has decayed to just ~5%, which provides a good estimation of the information depth of XPS. From ref. [144], under license CC BY-SA 3.0.

As an example of the capabilities of XPS and the relation between information depth and photon energy, Fig. 42a shows spectra of Au $4f_{7/2}$ measured at the FlexPES beamline of MAX IV (Lund, Sweden) in UHV conditions (~10^{-11}-10^{-10} mbar) for increasing X-ray photon energy. The spectra are normalized to the main peak at BE 84 eV, attributed to the Au $4f_{7/2}$ core level from bulk gold. An additional component

can be observed around 83.75 eV and originates from the surface layer. The shift is due to the differently coordinated surface atoms as compared to bulk atoms. The surface component is more visible at low photon energies, e.g. 170 eV and 220 eV, due to the low kinetic energy of the photoelectrons and the high surface sensitivity. With higher photon energies, the kinetic energy of the photoelectrons increases, hence, photoelectrons from increasing depth can escape the material and reach the analyzer. As a result, the bulk to surface ratio increases with the photon energy as shown in figure 42b.

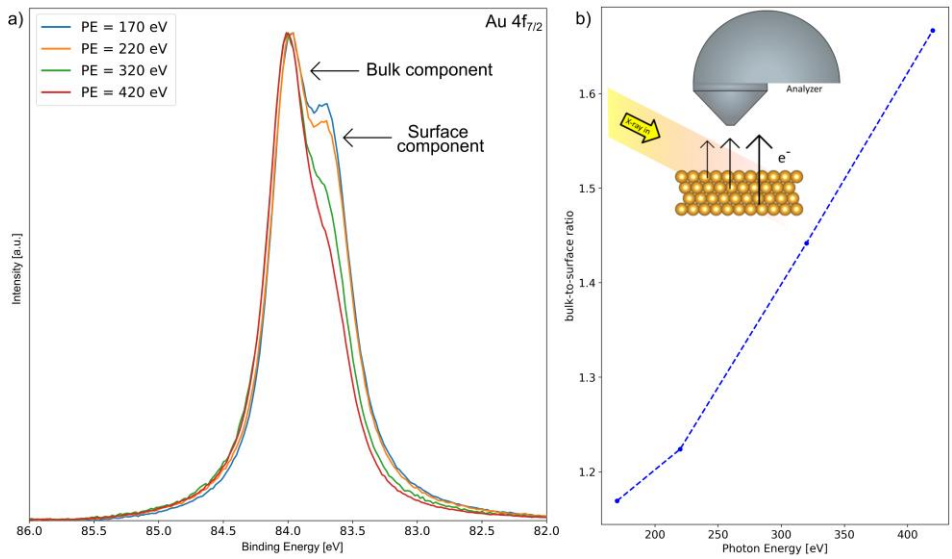

Figure 42
a) XPS measurements in UHV of the Au $4f_{7/2}$ core level at different photon energies (PE). The spectra are normalized to the maximum of the spectrum. The component shifted to lower binding energies is attributed to the surface core level, which becomes less pronounced at higher photon energies. b) Qualitative estimation of the peak-to-peak ratio of bulk vs surface components as a function of PE. The kinetic energy of the electrons increases with PE, thus the information depth increases.

Without UHV conditions, it would be much harder to detect photoelectrons at such low kinetic energies, due to the strong attenuation of the signal through the gaseous environment between sample and analyzer. However, liquids are unstable at such low pressures, limiting the study of electrochemical interfaces with traditional UHV XPS to *ex situ* conditions, as performed in **Paper III**. The next section (**5.1.1**) will show how XPS measurements at near-ambient pressure (NAP-XPS or AP-XPS) can be performed to study electrochemical systems *in situ*, as performed in **Papers IV, V, VII and IX**.

5.1.1 From vacuum to ambient pressure to electrochemistry

There are two main problems that need to be overcome to perform XPS at non-vacuum conditions[139]. First, as previously discussed, the short IMFP limits the distance that the photoelectrons can travel to reach the analyzer without being scattered by the gas molecules. The use of higher photon energies would increase the IMFP of photoelectrons, but at the expense of surface sensitivity, while the cross-section for photoelectric absorption would decrease. A significant improvement can be achieved by maximizing the photon flux and using the most advanced synchrotron radiation facilities. Nevertheless, it is also necessary to place the sample surface close enough to the analyzer cone. For gas pressures around 1 atm (~10^3 mbar), which is relatively high for common AP-XPS setups, electrons at ~100 eV can only travel for around 1 μm through the gas. To avoid pressure inhomogeneities at the sample surface, the entrance aperture diameter of the analyzer cone (nozzle) must be in the same order of magnitude of the distance from the sample. Furthermore, in these extreme conditions, a focused X-ray beam must come at shallow angles to not hit the analyzer cone. More commonly, AP-XPS experiments are performed at pressures of 10s of mbar, with sample-nozzle distances of 0.1-1 mm[139].

Second, the hemispherical analyzer must be kept in a low-pressure environment (<10^{-5} mbar) due to the high voltage differences in the electron detector. Otherwise, discharging through the gas may occur. Additionally, the electrons would also scatter significantly before reaching the detector if the pressure is too high. The most successful approach to avoid these issues was developed in the past three decades and consists in decreasing the pressure sequentially by differential pumping before the electrons can reach the hemispherical analyzer (Fig. 43). A series of pumping stages with decreasing pressure are mounted between the cone and the hemispherical analyzer. An aperture between each stage allows the electrons to travel through, and they are focused using electrostatic lenses to maximize the signal.

A similar setup is used at the HIPPIE beamline[145,146] of MAX IV (Fig. 44), where the electrochemical *in situ* experiments on the electrochemical oxidation of gold and the corrosion of Ni alloys discussed in this thesis were performed (**Papers IV, V, VII and IX**). The electrochemical cell was introduced in Fig. 17b. An electrolyte beaker could be placed directly in the chamber at 10-20 mbar water vapor, and kept at around 10 °C using a copper cooling plate, maintaining equilibrium between gas and liquid and thus preventing evaporation. The electrodes are mounted on a manipulator that allows for x-y-z axis movements and for connection to an external potentiostat. First, the electrodes are dipped in the electrolyte and the electrochemical treatment is performed. Then, the electrodes are fully withdrawn

from the beaker and brought close to the analyzer for AP-XPS measurements, while an electrolyte layer remains on the surface.

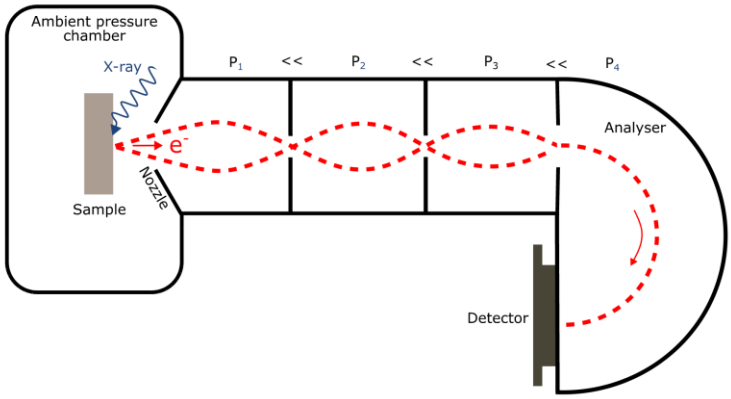

Figure 43
Schematic of an AP-XPS setup based on differential-pumping and electrostatic lenses.

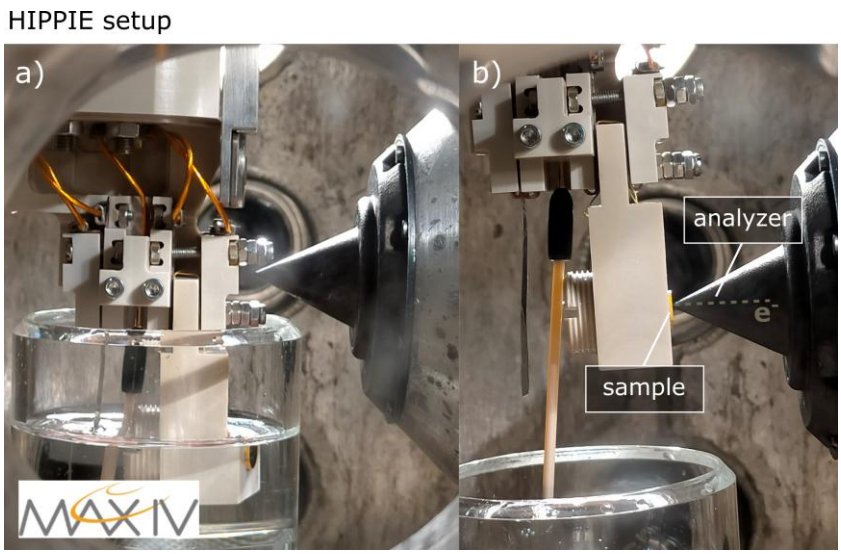

Figure 44
Photos of the AP-XPS setup at the HIPPIE beamline of MAX IV using a dip-and-pull approach where a) the sample is first dipped and polarized and b) the sample is then withdrawn from the electrolyte and brought close to the analyzer for AP-XPS measurements.

5.1.2 Beam-induced effects during AP-XPS measurements

A similar beam-induced effect to the one observed with RefleXAFS (Fig. 39) was observed during AP-XPS experiments on the electrochemical oxidation of gold (described in **Paper IV**). In this case, however, reduction of the gold (hydr)oxide under the beam was observed already at lower potentials. An example of the disappearance of the (hydr)oxide signal is shown in Fig. 44a, where the sample was first oxidized and then exposed under the beam, always probing the same surface region. This effect could be mitigated by moving the sample across the beam during the AP-XPS measurements (Fig. 45b,c).

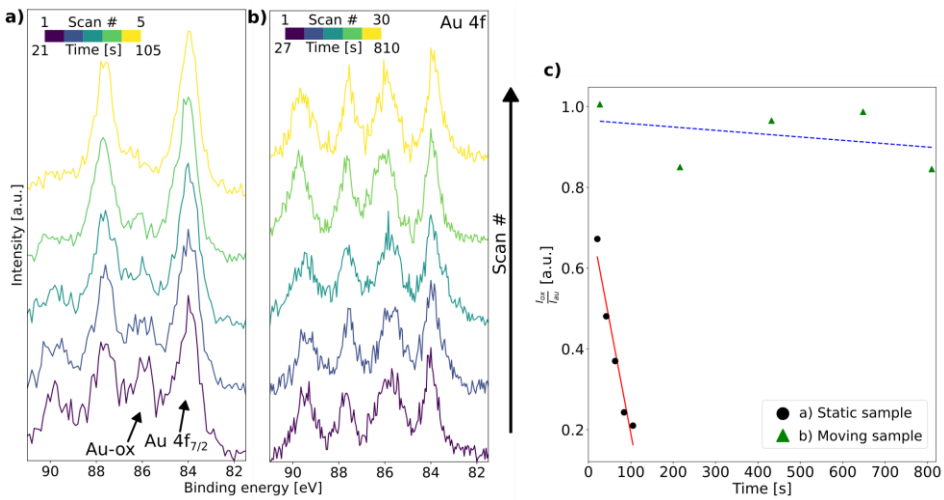

Figure 45
AP-XPS scans measured after electrochemical oxidation of gold at ~2V_{RHE} in 0.05 M H_2SO_4 while a) the sample was kept a fixed position and b) the sample was moved across the beam. c) ratio between (hydr)oxide and metallic signal over time for the two measurements. From **Paper IV**.

An explanation for the stronger beam-induced effect observed during AP-XPS compared to RefleXAFS could be attributed to the higher absorption cross-section at lower photon energies (Fig. 46). Another factor that can play an important role is the lower penetration through the material in case of total reflection during RefleXAFS, producing less secondary electrons.

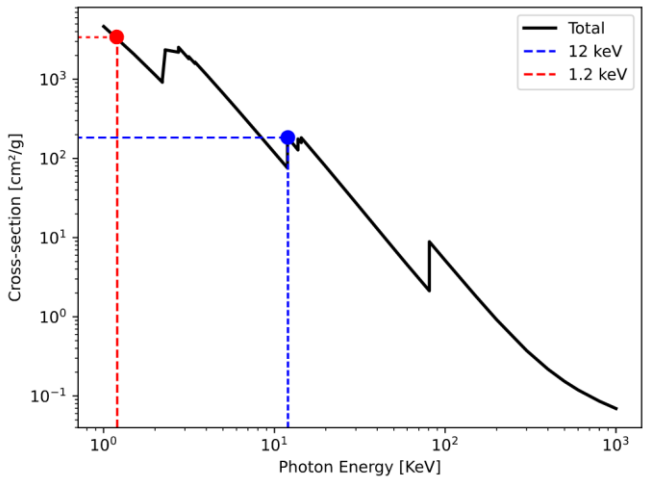

Figure 46
a) Cross-section of Au at different energies as shown in Fig. 27a, the cross-sections at the energies used for the RefleXAFS experiment at Balder (12 keV) and for the AP-XPS experiment at HIPPIE (1.2 keV) are highlighted in blue and red, respectively.

5.2 X-ray Diffraction

XRD is a powerful tool to reveal the atomic structure, phases and crystallinity of a sample. The mechanism of XRD relies on the elastic scattering of an incoming plane wave by a periodic crystal lattice, where each scattering atom in the solid becomes a source of secondary radiation, emitting a spherical wave. These waves can interfere constructively or destructively along certain directions. If the crystal lattice is well-ordered, a three-dimensional interference pattern will be produced, providing information about the crystal structure. The relation between this interference pattern and the crystal structure was derived by Max Von Laue, for which he was awarded the Nobel Prize in 1914, and by William Henry Bragg and his son William Lawrence Bragg, who were awarded the Nobel Prize in 1915. These formulas are briefly described in this chapter; a detailed derivation can be found in the relevant literature[33].

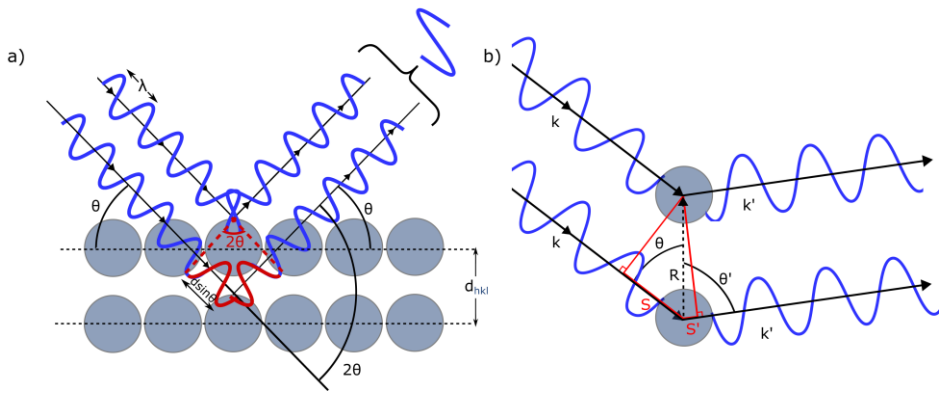

Figure 47
a) Schematic repesentation of elastic scattering from two crystal planes, visualized according to the Bragg diffraction principles. b) Schematic representaion of eleastic scattering from two atoms, according to the Laue formulation.

Bragg's law is derived considering the elastic scattering of a monochromatic wave impinging and reflecting at the same angle θ on two infinite crystal planes separated by a distance d, as shown in Fig. 47a. In the case of elastic scattering, the X-rays do not lose energy during scattering, i.e. the wavelength λ remains constant. The X-ray scattered by the second plane travels a longer path compared to the one scattered by the first plane. This path difference is equal to $2dsin(\theta)$, and determines if the scattered outgoing waves are in phase or out of phase. If the path difference is equal to an integer multiple of the wavelength $n\lambda$, the outgoing waves are in phase and interfere constructively, forming one wave with twice the amplitude and same frequency. If instead the waves are out of phase, they interfere destructively and cancel each other out. As a result, Bragg's law is the condition that needs to be satisfied for constructive interference:

$$2dsin(\theta) = n\lambda \qquad (17)$$

From this condition it can be seen that for a family of planes (hkl) and a fixed λ there are infinite but discrete θ values that can produce constructive interference and thus define a diffraction pattern. Note that in an XRD experiment, the detector measures 2θ which is the angle between the direct beam and the diffracted beam. Another important conclusion from (17) is that if $d < \lambda/2$ there would not be any diffraction, highlighting the importance of using sufficiently small wavelengths to study atomic structures.

Von Laue's formulation can be derived by considering monochromatic electromagnetic radiation with wavevector $\vec{k}$ ($|\vec{k}| = 2\pi/\lambda$) incident at an angle θ on two scatterers separated by a vector $\vec{R}$ ($|\vec{R}|$=R), as shown in Fig. 47b. For elastic scattering events the energy is conserved, hence, the scattered wavevector $\vec{k}'$

intensity remains the same ($|\vec{k'}| = |\vec{k}| = 2\pi/\lambda$). In the general case where the outgoing wavevector can have a different direction (θ'), the path difference (S+S') is equal to $R\cos(\theta)+R\cos(\theta')$, giving the following condition for constructive interference:

$$R\cos(\theta) + R\cos(\theta') = n\lambda \quad (18)$$

Using the wavevectors this equation can be rewritten as:

$$\frac{\vec{R}\cdot\vec{k'}}{|\vec{k'}|} - \frac{\vec{R}\cdot\vec{k}}{|\vec{k}|} = n\lambda \quad (19)$$

Since $|\vec{k'}| = |\vec{k}| = 2\pi/\lambda$, it follows that:

$$\vec{R}\cdot\vec{Q} = 2\pi n \quad (20)$$

Where $\vec{Q} = \vec{k'} - \vec{k}$ is the change in momentum during scattering.

To further discuss this, it is necessary to briefly introduce the reciprocal lattice, which is the Fourier transform of the real atomic lattice. An infinite and perfectly periodic atomic lattice can be described by a set of 3D vectors $\vec{R} = u\vec{a_1} + v\vec{a_2} + w\vec{a_3}$ where *u,v,w* are integer numbers and $\vec{a_1}, \vec{a_2}, \vec{a_3}$ are the real basis vectors. $\vec{R}$ can be seen as an extension to the 3D space of $\vec{R}$ in Fig. 47b and eq. 20. From the real lattice, we can define its reciprocal lattice with a set of 3D vectors $\vec{K} = h\vec{b_1} + k\vec{b_2} + l\vec{b_3}$ where *h,k,l* are integer numbers and $\vec{b_1}, \vec{b_2}, \vec{b_3}$ are the basis vectors. The reciprocal lattice must fulfill the condition:

$$e^{i\vec{K}\cdot\vec{R}} = 1 \quad (21)$$

Equation 21 is fulfilled only if $\vec{K}\cdot\vec{R} = 2\pi n$, from which is possible to derive the relationships between real space and reciprocal space basis vectors:

$$b_1 = 2\pi\frac{\vec{a_2}\times\vec{a_3}}{a_1\cdot(\vec{a_2}\times\vec{a_3})} \qquad b_2 = 2\pi\frac{\vec{a_3}\times\vec{a_1}}{a_1\cdot(\vec{a_2}\times\vec{a_3})} \qquad b_3 = 2\pi\frac{\vec{a_1}\times\vec{a_2}}{a_1\cdot(\vec{a_2}\times\vec{a_3})}$$

From $\vec{K}\cdot\vec{R} = 2\pi n$ it can also be derived that to have constructive interference and thus satisfy eq. 20 $\vec{Q}$ has to be a vector of the reciprocal lattice of $\vec{R}$, i.e. $\vec{Q}=\vec{K}$.

To visualize which points in reciprocal space can be reached by $\vec{Q}$, for a specific length and direction of $\vec{k}$ and any possible direction of $\vec{k'}$, it is common to use the Ewald sphere. An example of a section of the Ewald sphere is shown in Fig. 48a, where the radius of the circle is given by $\vec{k}$. For a given direction of $\vec{k'}$, the Laue condition will be fulfilled when the sample is rotated such that a reciprocal lattice point intersects the circle (Fig. 48b).

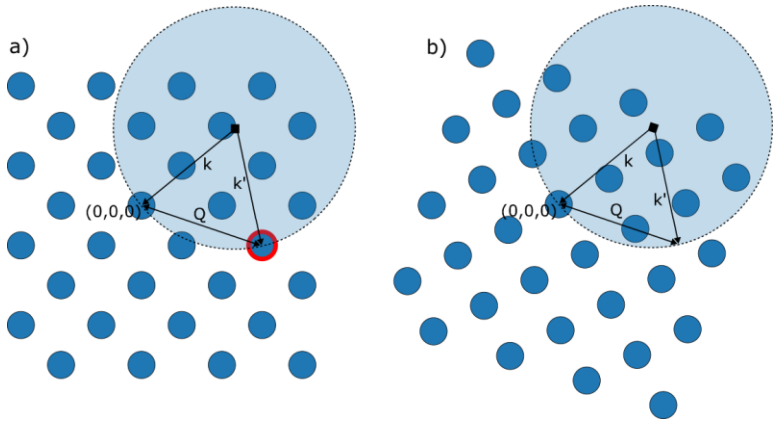

Figure 48
a) 2D representation of the Ewald sphere where the Laue's condition is fulfilled for a specific scattering angle. The visible reflection is highlighted by the red circle. b) If the sample is rotated azimuthally around its origin (0,0,0) to another angle, the same reflection disappears.

5.2.1 Surface X-ray Diffraction

The diffraction pattern observed on the detector, is related to the crystal's reciprocal lattice. In the case of bulk diffraction from a single crystal (Fig. 49a), the crystal acts as a 3D grating for the X-rays producing a pattern of intense and well-defined Bragg spots (Fig. 49b,c). In the case of SXRD, the beam is focused on the surface at shallow incident angles (Fig. 49d). In this case, the signal from the surface is enhanced and new features can be observed[147]. The reciprocal lattice of an ideal 2D surface does not consist of Bragg spots, it is made of diffraction rods, because it is a periodic structure in a 2D space, lacking structural periodicity in the out of plane direction (normal to the surface). As a result of the scattering from a semi-infinite crystal, the SXRD pattern is characterized by the so-called crystal truncation rods (CTRs) (Fig. 49e,f). If the surface presents an ordered adlayer of adsorbate species, or a well-defined surface reconstruction, or an ultra-thin oxide or similar, new diffraction rods appear in the diffraction pattern, with a different periodicity. These are called superlattice rods (SLRs). Note that the diffraction patterns shown in Fig. 49c,f are measured at high energies (several tens of keV) to increase the portion of the reciprocal lattice ($\vec{Q}$-range).

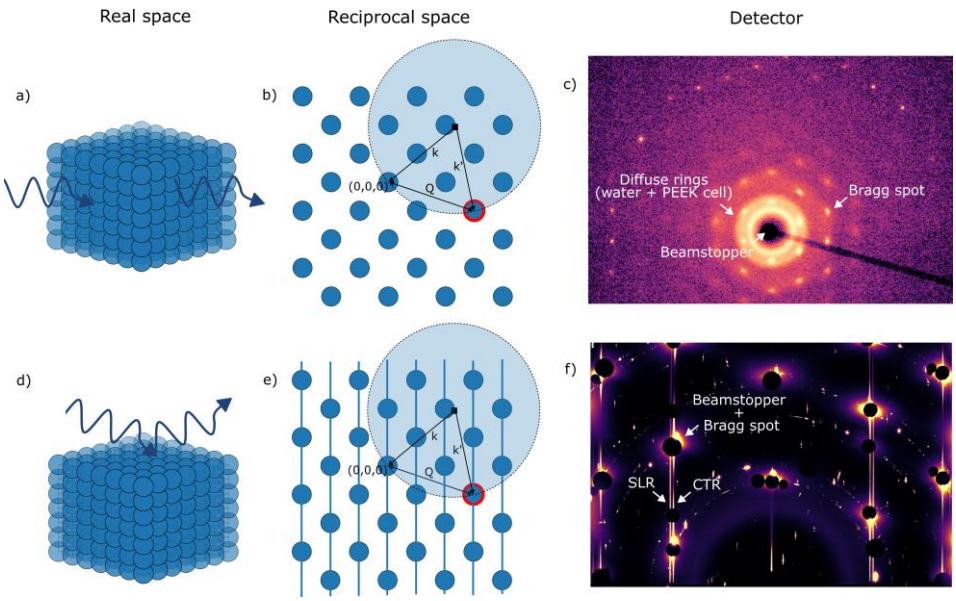

Figure 49
a,b,c) Concept of bulk diffraction from a single crystal and example of its diffraction pattern from an experiment at P21.1 (DESY) on Al(111), where also the electrochemical cell and water contribute to the total scattering. A beam stopper is placed to attenuate the direct beam, which would increase the background and also damage the detector due its very strong intensity. d,e,f) Concept of surface diffraction from a single crystal and example of its diffraction pattern from experiments at P21.2 (DESY) on Au(111). Beam stoppers are placed to attenuate both the direct beam and the Bragg spots. In this way the background is reduced and it becomes possible to see the CTRs and SLRs.

A limitation of diffraction-based methods is that only crystalline structures can produce a well-defined pattern. RefleXAFS is a good alternative to probe the chemistry and structure of the surface in case of amorphous species, but the energy used for RefleXAFS measurements is limited to the absorption edge energies of the sample, while SXRD can be used at high energies on any material, which is useful to penetrate the electrolyte and thus perform *operando* or *in situ* experiments.

In addition to *operando* X-ray absorption spectroscopy studies, the same electrochemical cell shown in Fig. 19a was used for *operando* 2D-SOR and for tomographic SXRD (TSXRD) at the P21.2 beamline of PETRAIII, DESY. A photo of the setup is shown in Fig. 50. TSXRD[148] is a new method developed by J. Gustafson and H. Sjö at Lund University to investigate polycrystalline surfaces in *operando* conditions. Through this collaboration, we studied the orientation-dependent electro-oxidation of a polycrystalline gold sample and demonstrated the feasibility of TSXRD in electrochemical environments (**Paper V**).

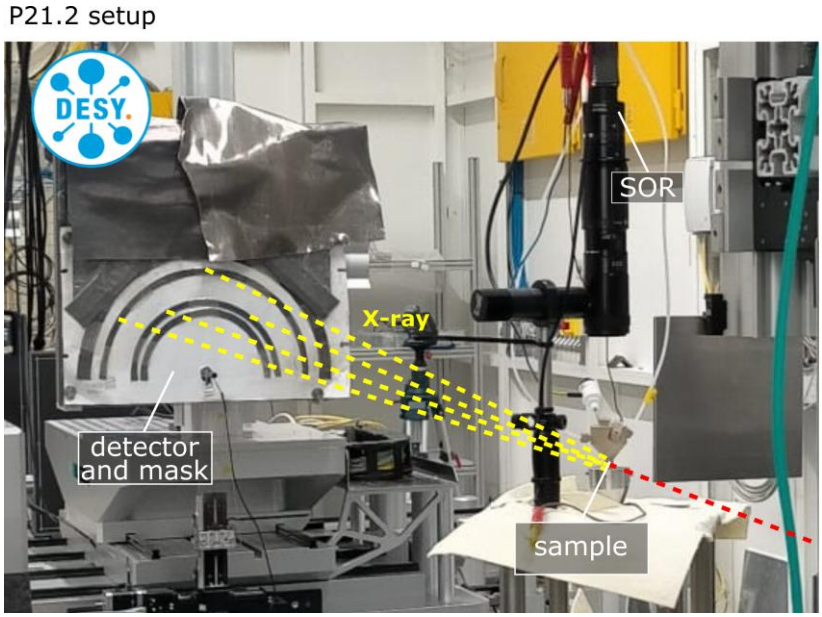

Figure 50
Photo of the TSXRD and 2D-SOR setup at the P21.2 beamline of PETRAIII, DESY (Hamburg, Germany).

5.3 2D Surface Optical Reflectance Microscopy

Over the past decade, 2D-SOR has emerged as a simple yet powerful and relatively inexpensive tool for investigating reactive surfaces in gas-phase and electrochemical environments[149], as well summarized in **Paper VI**. The basic principle of 2D-SOR is to measure the change in reflectance of a surface during a reaction, in our case using a 660 nm LED light (red) (Fig. 51b). Thanks to a transparent glass window mounted on top of the *operando* cell, 2D-SOR can be easily combined with electrochemical measurements and grazing incidence hard X-ray methods like RefleXAFS or TSXRD (Fig. 51a). As a result, complementary information can be obtained and the surface can be monitored during measurements, for example to check for beam-induced effects. Understanding the changes in reflectance, however, is not trivial, since they can be due to roughening, changes in surface refractive index and optical properties or interference effects arising from a layered structure. Several of these features are discussed in **Papers II, V and VI**, where Fresnel's equations were used to relate the (hydr)oxide thickness to the change in optical reflectance. An example of normalized 2D-SOR images of a

Au(111) single crystal acquired during cyclic voltammetry before and after oxidation is shown in Fig. 51c and 51d, respectively.

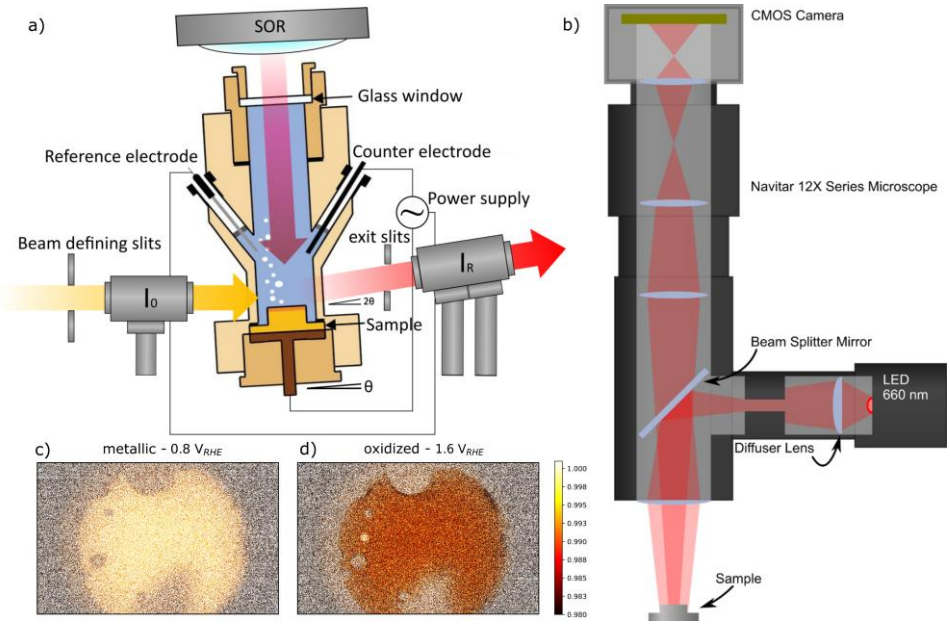

Figure 51
a) Schematic of the electrochemical setup for 2D-SOR combined with RefleXAFS. b) Components of the 2D-SOR microscope. c,d) Normalized 2D-SOR image of Au(111) during CV in 0.05 M H_2SO_4 before and after electrochemical oxidation. From **Paper II and VI**.

5.4 Ultra-High Vacuum methods

Due to the short IMFP, many electron-based methods require a UHV system. Furthermore, in *ex situ* studies, the presence of contaminants can alter the surface after the electrochemical treatment or even make it impossible to probe the surface due to excessive electron attenuation through the contaminant layer. To this end, a transfer system that avoids exposure of the sample to air and thus minimizes the presence of contaminants after an electrochemical treatment can be used[150]. The portable transfer system presented in this thesis (**Paper III**) was used at Lund University and at the FlexPES beamline of MAX IV to study the electrochemical oxidation and surface restructuring of Au(111) after CV. A schematic drawing of the setup used at Lund University is shown in Fig. 52.

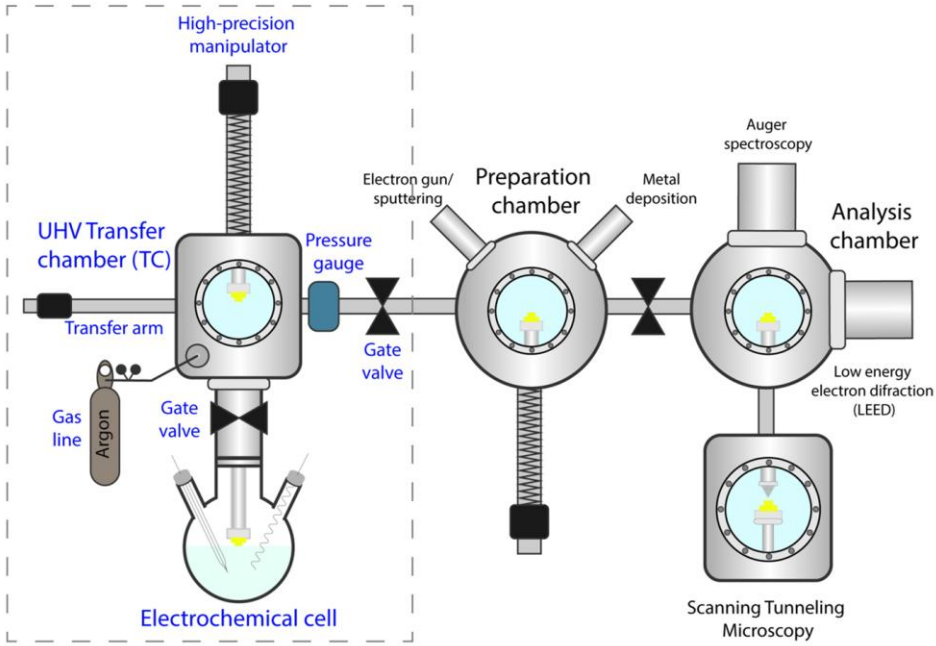

Figure 52
A schematic drawing of the transfer system attached to the UHV system at Lund University. From **Paper III**.

A photo of the setup at Lund University is shown in Fig. 53, where a preparation chamber allows for single crystal preparation using a sputter gun and electron-beam annealing, as well as for thin films deposition using molecular beam epitaxy (Fig. 53a). Furthermore, the system is equipped with STM, LEED and AES for surface analysis (Fig. 53b). In addition, at FlexPES, *ex situ* XPS was performed. The procedure consists of transferring the as-prepared sample, from the preparation chamber to a transfer chamber filled with Argon and then to the electrochemical cell, where the surface is dipped and then carefully retracted by a few mm to form a hanging meniscus (Fig. 53c). This configuration allows to expose only the (111) surface to the electrolyte. Once the electrochemical treatment is performed, the sample is withdrawn from the electrolyte and rinsed with ultrapure water. The treated sample is then moved to the transfer chamber, separated from the UHV system and the electrochemical cells through gate valves, and then pumped down to UHV. Then, the sample can be transferred to the UHV system for surface analysis.

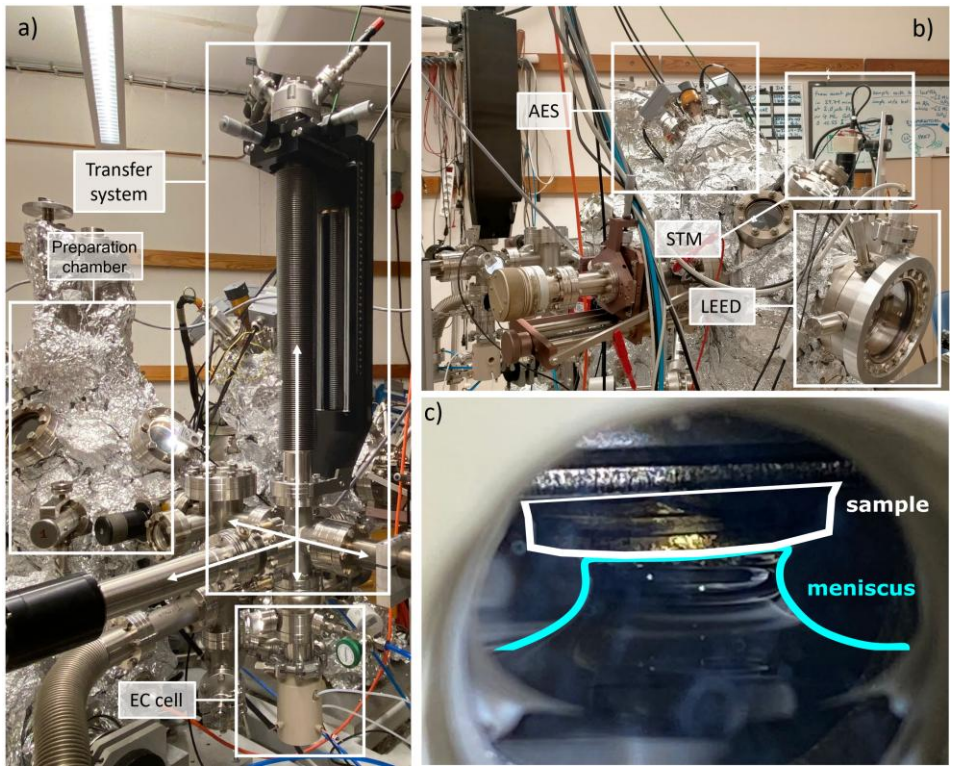

Figure 53
a) A photo of the transfer system connected to the preparation chamber at Lund University. b) A photo of the analysis chamber attached to the preparation chamber, equipped with AES, STM, and LEED. c) A photo of the meniscus formed in the electrochemical cell after dipping the sample in the electrolyte and then retracting it by a few mm.

5.4.1 Scanning Tunnelling Microscopy

STM was developed in the early 80s by the 1986 Nobel Prize winners Gerd Binnig and Heinrich Rohrer[151]. Thanks to the possibility to probe single atoms of conductive (or semi-conductive) surfaces, this technique revolutionized the field of surface science. STM measures the tunnelling current between the surface and a sharp metallic tip, the current decreases exponentially with increasing sample-tip distance and thus provides extremely high sensitivity. The tip is ideally terminated by a single atom (Fig. 54), which is essential to achieve the best atomic resolution. Tunnelling current is measured while a bias voltage is applied between tip and sample and the tip must be very close to the surface (down to a few Å), which is possible thanks to piezoelectric actuators that precisely control the tip and the

sample positions. The tip is then scanned across the surface, measurements can be traditionally performed either in constant current mode or constant height mode. In constant current mode, the height of the tip is adjusted through a feedback system to keep the current fixed to a setpoint, hence, the z-position of the tip is mapped across the surface. This mode safer when measuring large non-flat surfaces, where the tip can crash into islands and other defects. In this thesis, surface roughening of Au(111) due to oxidation-reduction was studied, thus the constant current mode was always used. An example of an STM image of the reconstructed Au(111) surface is shown in Fig. 54, where a herringbone reconstruction is clearly visible on the atomic terraces.

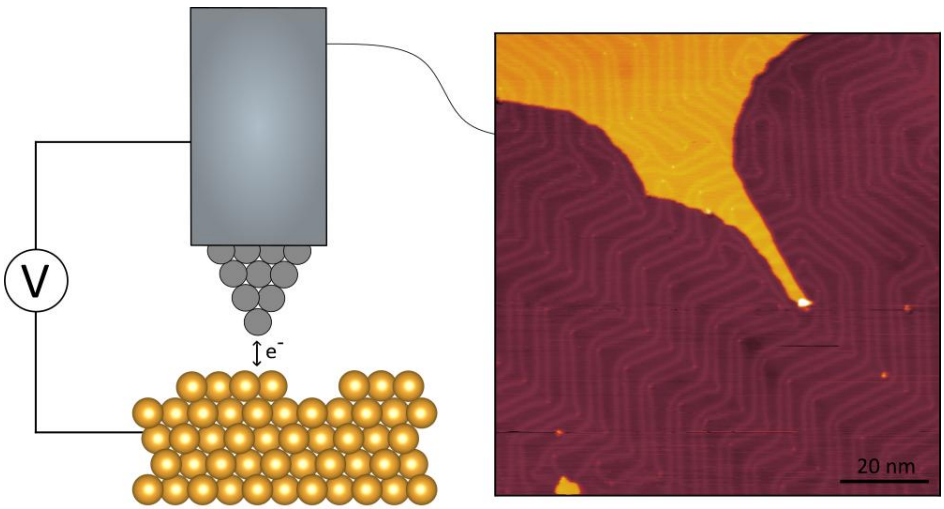

Figure 54
A simple schematic of the STM tip measuring tunneling current from a metallic surface and an example of a pristine Au(111) surface measured with STM at Lund University.

All the STM measurements shown in this thesis were performed at ~10^{-11} mbar, which greatly helps to improve the quality of the measurements and especially minimizes the presence of contaminants on the surface and on the tip during measurements. Note that STM does not necessarily need a UHV environment, for example, there are setups where STM can be directly performed in liquids[22], although it is difficult to achieve reasonable image quality under electrocatalytic and corrosive conditions, due to high currents, dissolution, bubbles evolution, etc.

5.4.2 Low Energy Electron Diffraction

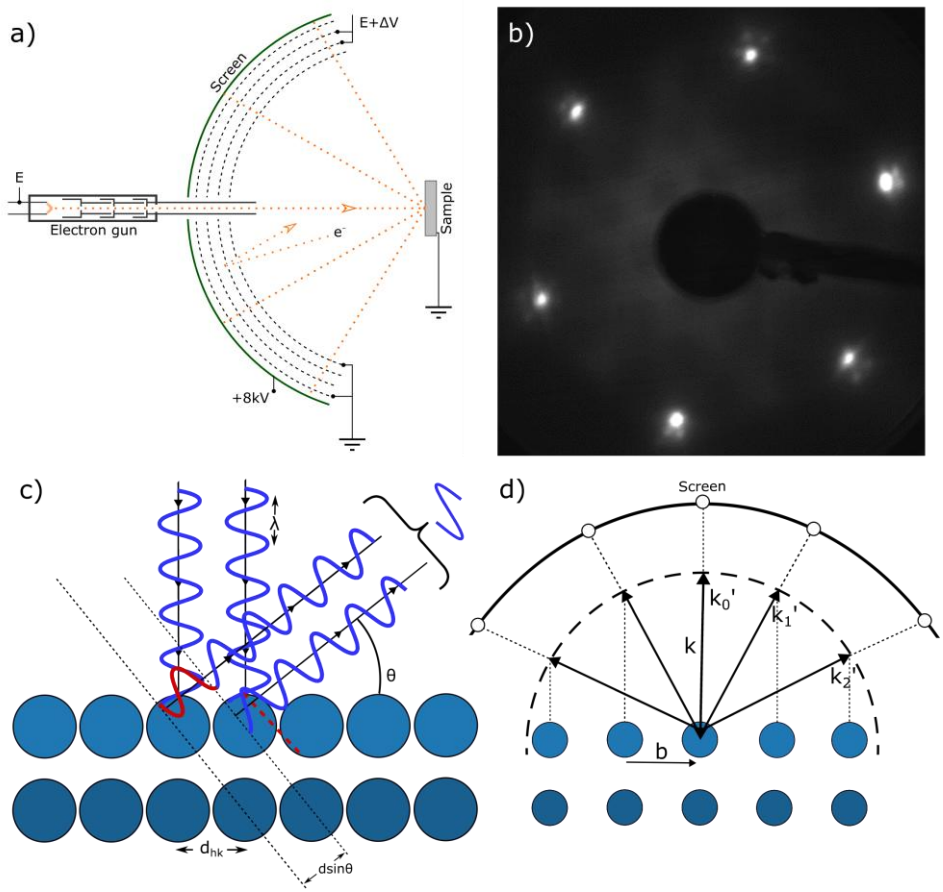

Figure 55
a) Schematic of a LEED apparatus, from ref. [152], licensed under CC BY-SA 4.0. b) A LEED pattern from a pristine Au(111). c) LEED diffraction based on Bragg's law and d) on Von Laue's formulation.

LEED[153] is based on the diffraction of an electron beam (typically in a range of 50-200 eV) incident at 90° on the sample surface, the back-scattered electrons are collected on a fluorescent screen where a diffraction pattern can be observed (Fig. 55a). Since it is a diffraction-based technique, LEED can provide information on ordered surface structures, for example in Fig. 55b it is possible to see the typical pattern of the reconstructed Au(111) surface characterized by an hexagonal reciprocal lattice where each Bragg spot exhibits a star-shape due to the 3 domains of the reconstructed surface, with a larger surface unit cell (22x√3) and rotated by

120º against each other. The basics of X-ray diffraction previously explained still hold for electron diffraction (Fig. 55c,d), with $\lambda=h/\sqrt{2mE}$.

5.4.3 Auger Electron Spectroscopy

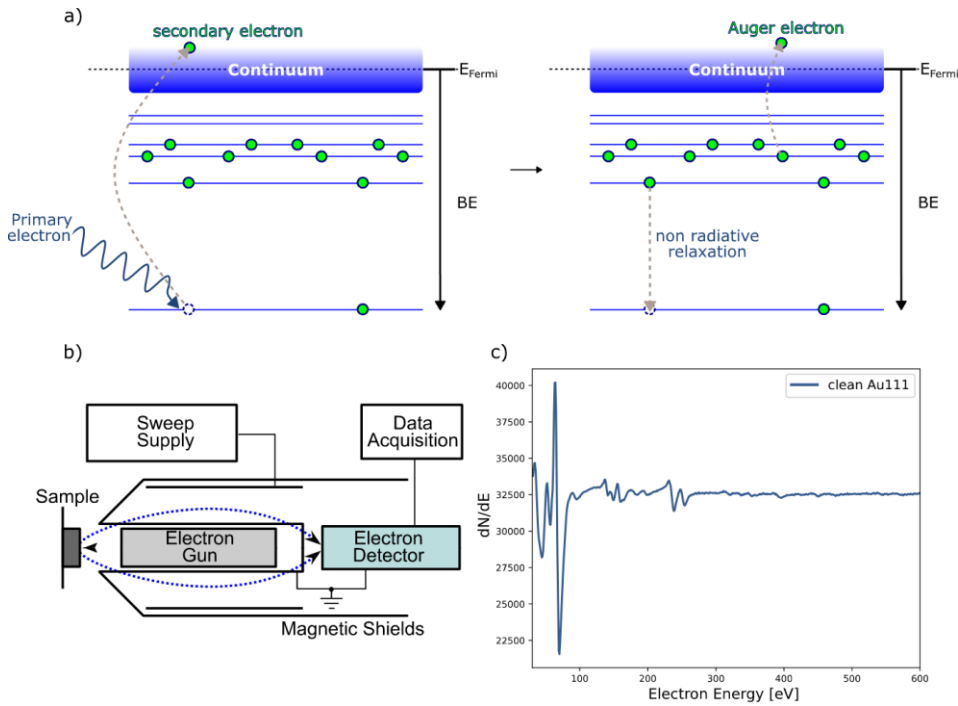

Figure 56
a) Schematic energy level diagram of the Auger electron emission process. b) AES apparatus, adapted from ref. [154], licensed under CC0 1.0. c) Example of an AES spectrum measured on a pristine Au(111).

AES[42] was used in the works presented in this thesis to detect contaminants and surface oxides on Au(111). Auger electrons are secondary electrons emitted from an outer-shell when an excited atom relaxes by filling a core-hole level (Fig. 56a). An alternative mechanism of relaxation to the AES process is XRF, described in the previous chapter (**Section 4.3.1**). The characteristic kinetic energies of the Auger electrons can be used as a fingerprint technique to identify the species present on the surface. A schematic of the AES apparatus and an example of an AES measured from a pristine Au(111) surface is shown in Fig 56b and 56c, respectively.

6. Summary of papers

A substantial portion of the work presented in this thesis is centered on the development and application of RefleXAFS (**Papers I, II, VII, VIII, X**), using gold electro-oxidation as main model system. More broadly, the thesis encompasses two overarching research directions. The first is primarily dedicated to the use of methods for investigating model electrode surfaces under *ex situ*, *in situ*, and *operando* conditions, including 2D-SOR (**Papers II, V, and VI**), AP-XPS (**Papers IV, V, VII, and IX**), STM (**Papers III and VII**), and SXRD (**Paper V**). The second addresses the stability and electrochemical properties of Au (**Papers I-VIII**), Pt (**Paper X**), and a Ni alloy 59 (**Papers I and IX**) under reactive conditions.

Paper I

Probing the electrode-liquid interface using total-reflection X-ray absorption spectroscopy

In this work, we demonstrate the ability of RefleXAFS at the P64 beamline to detect nanoscale surface oxides on model electrodes under constant electrochemical polarization. RefleXAFS was developed in the 1980s and mainly applied to sputtered thin films. Here, we employ a versatile *operando* electrochemical cell to study more realistic samples (polycrystalline Au and Ni alloy 59), independent of sample thickness. Polycrystalline Au in 0.05 M H_2SO_4 forms a relatively thick Au^{3+} oxide/hydroxide layer during OER, with indications of a thin layer of Au^{3+} species already present before the OER onset. Ni alloy 59 undergoes passivity breakdown during OER, but exhibits a different surface chemistry in alkaline and acidic conditions. A higher Ni^{2+} content is observed at low potentials in alkaline (pH 12) compared to neutral (pH 7) conditions, whilst in both electrolytes a thick MoO_3-rich corrosion scale forms at higher potentials during OER. Results at pH 7 agree with AP-XPS data (**Paper IX**), confirming comparable surface sensitivity of RefleXAFS. Measurements were performed with a de-focused beam at energies as low as 8 keV and acquisition times of several minutes per spectrum, averaging 2-3 scans to achieve a good signal-to-noise ratio.

Paper II

Following the electrochemical oxidation of Au(111) in real-time using surface optical reflectance and total-reflection X-ray absorption spectroscopy

In this work, we combine 2D-SOR and RefleXAFS to follow the electrochemical oxidation and reduction of Au(111) during CV in 0.05 M H_2SO_4. By leveraging the capabilities of the Balder beamline and a 4th generation synchrotron source (MAX IV), RefleXAFS spectra were measured in a few seconds and there was no need to average several spectra to achieve a good signal-to-noise ratio. As opposed to High Energy SXRD, which was previously combined with 2D-SOR and CV in real-time (reported in **Paper VI**), RefleXAFS can be used to directly disentangle the contribution of surface oxidation to the changes in optical reflectance. As a result, the thickness of a self-limiting Au^{3+} oxide/hydroxide layer forming prior to the OER onset was calculated using the Fresnell equation. The thickness was estimated to be ~5 Å, in good agreement with previous studies and with the charge integrated from the reduction current peak in the CV.

Paper III

A transfer cell for ultra-high vacuum surface analysis of samples exposed to electrochemical environments

In this work, we developed a transfer system to study *ex situ* in UHV the surface chemistry and structure of Au(111) after electrochemical treatments, with STM, LEED and AES in the home-lab UHV system, and with XPS at the FlexPES beamline of MAX IV. First, roughening of the surface was investigated as a function of electrochemical oxidation-reduction cycles in 0.05 M H_2SO_4, then the stability of the electro-oxidized surface in UHV conditions was studied. In agreement with previous studies, the progressive roughening follows a linear trend within the first 10 oxidation-reduction cycles. Additionally, we show that the thin (hydr)oxide formed prior to OER is unstable in UHV conditions, instead a thick Au_2O_3 phase formed during OER at high potential can be detected.

Paper IV

Thickness and chemistry of electrochemically formed oxide films on Au(111) probed with ambient pressure X-ray photoelectron spectroscopy

In this work, we study the electrochemical oxidation of Au(111) in 0.05 M H_2SO_4 using AP-XPS with a dip-and-pull approach. The experiment follows the same procedure described in **Paper IX** for Ni alloy 59, where the sample is dipped in the electrolyte, electrochemically polarized and then fully withdrawn from the electrolyte for quantitative AP-XPS measurements. This simplified approach enables to adopt better mitigation strategies of beam-induced effects as well as to

perform electrochemical measurements at high current densities, e.g. during OER. In agreement with 2D-SOR and RefleXAFS from **Papers II and VII**, the Au(111) surface is shown to form a self-limiting $Au(OH)_3$ film of ~5 Å, while at higher potentials, during OER, a thicker mixed-phase of $Au(OH)_3/Au_2O_3$ is proposed to grow, following a Stranski-Krastanov mode.

Paper V

Surface orientation-dependent electro-oxidation of a polycrystalline gold electrode
In this work, we combine 2D-SOR, AP-XPS and Tomographic SXRD to follow the electrochemical oxidation of different grains of a polycrystalline Au model electrode in 0.05 M H_2SO_4. Previous 2D-SOR studies (reported in **Paper VI**), suggest that the changes in optical reflectance associated to surface oxidation of different grains take place at different potentials during CV depending on the surface orientation. By performing *in situ* AP-XPS measurements on three different grains separately, this trend is confirmed. Furthermore, TSXRD is used to follow this behavior in real-time under *operando* conditions and compared to 2D-SOR and AP-XPS. Although TSXRD cannot clarify the structure of the amorphous (hydr)oxide layer detected with AP-XPS, it can be used to follow the interfacial roughening, showing a similar trend to 2D-SOR and providing additional information.

Paper VI

2D-surface optical reflectance for use in harsh reactive environments
This review paper summarizes the recent use of 2D-SOR in harsh reactive environments, from gas-phase catalysis to corrosion and electrocatalysis studies. 2D-SOR is shown to be a powerful, cheap and easy-to-use method to follow the surface changes, like surface oxidation and beam-damage, with extremely high sensitivity. To understand these changes, 2D-SOR is combined with a range of complementary techniques, such as RefleXAFS. In the case of gold, both techniques indicate a thickening of the (hydr)oxide layer during OER, in agreement with **Papers IV and VII**.

Paper VII

An ultrathin hydroxide film governs the stability and reactivity of gold for the oxygen evolution reaction
In this work, we combined time-resolved *operando* RefleXAFS and Inductively-Coupled Plasma Mass Spectrometry with *in situ* AP-XPS and *ex situ* STM to gain a comprehensive view on the electrochemical behavior of Au(111) in 0.05 M H_2SO_4 before, during and after OER. We show that Au(111) forms a self-limiting hydroxide layer prior to the onset of OER, which behaves in a similar way to passive

films on corrosion-resistant alloys. This passive film serves as the catalytically active surface and controls electrode dissolution and restructuring during potential cycling. Under OER conditions, the surface undergoes rapid oxidation and dissolution, suggesting a de-passivation mechanism linked to OER, similar to the passivity breakdown of Ni alloys described in **Paper IX**. Although AP-XPS reveals a transition from a pure Au^{3+} hydroxide to a thicker, mixed Au^{3+} oxide/hydroxide phase during the OER, RefleXAFS indicates that the local structure remains indistinguishable between thin and thick (hydr)oxide films, consistent with the persistence of a square-planar coordination.

Paper VIII

Linking surface chemistry and dissolution of Au(111) in H_2SO_4 and NaOH electrolytes: pH and scan rate effects

In this work, we combine *operando* RefleXAFS with Inductively-Coupled Plasma Mass Spectrometry to follow surface oxidation and dissolution during CV for different scan rates and upper potential limits in 0.05 M H_2SO_4 (pH 1.3) and 0.05 M NaOH (pH 12.6). We show that in both media an ultrathin, self-limiting $Au(OH)_3$ film forms prior to the onset of the OER. However, the hydroxide film thickness, stability, and dissolution dynamics differ in the two electrolytes. In NaOH, oxidation initiates at lower potentials but proceeds slowly, yielding a thinner, more stable film that remains passive at high potentials. In contrast, in H_2SO_4, the film rapidly grows thicker, and undergoes de-passivation near the OER onset, leading to a sharp increase in dissolution. During film reduction in NaOH, significantly higher dissolution is observed, despite a thinner film being reduced, compared to H_2SO_4. Potential scan-rate variations show that dissolution during the reduction step in NaOH and the de-passivation step in OER are the most sensitive to the scan rate during the CV cycle.

Paper IX

The oxygen evolution reaction drives passivity breakdown for Ni-Cr-Mo alloys

In this work, we combine *in situ* APXPS, XANES, XRF, GI-XRD and XRR to study the passive film growth and breakdown of a Ni alloy 59 under static anodic polarization at increasing potentials. The material remains stable and passive up to the OER onset, where surface enrichment of Mo^{6+} oxide and Cr^{3+} hydroxide is observed, accompanied by severe alloy dissolution. *In situ* XANES measurements from the electrolyte suggest the absence of Cr^{6+} as a dissolution product, indicating that the observed passivity breakdown mechanism differs from the typical transpassive dissolution behavior of Cr-containing alloys.

Paper X

Platinum surface oxides govern the cathodic overpotential of the oxygen reduction reaction

In this work, we used *operando* RefleXAFS supported by DFT calculations and microkinetic modelling to resolve the structure of surface oxides on a polycrystalline platinum electrode and their impact on the ORR activity. We identify the formation of surface oxide motifs with both 4-fold and 6-fold oxygen coordination and show that platinum spontaneously oxidizes at the OCP under O_2 saturation. Furthermore, we show that the oxide coverage increases with upper vertex potential, slower scan rates, and extended hold times at OCP. Crucially, we demonstrate that ORR onset is delayed until these oxides are reduced, following an inverse relationship between oxide amount and ORR activity.

7. Conclusion and Outlook

This thesis focused on the development and application of RefleXAFS combined with additional *ex situ*, *in situ* and *operando* methods to investigate the surface evolution of model electrodes (Au, Pt and Ni alloy 59) in electrocatalytic environments. Au single- and poly- crystals were the main model systems used to benchmark RefleXAFS for electrocatalysis applications, especially thanks to their popularity, ease of surface preparation and well-established electrochemical response. On the other hand, Ni alloy 59 served as a secondary benchmark material for corrosion applications, where previous *in situ* studies were used for comparison. In contrast to Au, Ni alloy 59 is an industrial material presenting several alloying elements and different surface chemistry, enabling further exploration of the capabilities of RefleXAFS. Besides method development, Au and Pt were used as model systems to understand the surface processes involved on noble metals during the OER and the ORR, respectively. These mechanisms are important to design more efficient electrocatalysts for electrolyzers and fuel cells applications, where sluggish reaction kinetics and electrocatalysts degradation are crucially limiting their commercialization. Ni alloy 59, on the other hand, is a highly corrosion-resistant alloy that is catalytically active towards the OER, which complicates the interpretation of its electrochemical response, as the measured current can arise from both passivity breakdown and OER.

Among the main findings of this thesis work, it is shown that, even for noble metals, surface oxidation occurs rather easily in electrochemical environments and crucially affects the electrochemical properties, including reactivity and stability. The presence of a distinct surface (hydr)oxide of a few atomic layers during the OER on Au and during the ORR on Pt, exacerbates the complexity of these dynamic interfacial processes. The surface does not necessarily follow the bulk behavior, hence, it requires dedicated surface-sensitive methods to fundamentally understand its chemistry and structure at the atomic-scale. Although studies on Au and Pt electrochemical oxidation and on Ni alloy 59 corrosion may appear to belong to two distinct fields of electrochemistry, i.e. electrocatalysis and corrosion science, respectively, these materials can show similar behaviors. These surfaces form a passive film under certain conditions, which can undergo de-passivation during OER, leading to substantial dissolution and further oxidation. I believe this evidence highlights that surface oxidation, electrocatalytic activity, and metal dissolution are strongly linked.

As shown by the *ex situ* studies in UHV on Au, the phases formed during the electrochemical treatments are highly unstable upon withdrawal from their electrochemical environment, highlighting the importance of adopting *in situ* and *operando* approaches. Yet, performing real *operando* studies under electrochemical polarization control is extremely challenging, since the sample must be buried beneath a thick, dense electrolyte. Furthermore, these (hydr)oxide layers are typically amorphous, complicating the use of diffraction-based methods. AP-XPS provided excellent surface sensitivity and chemical sensitivity, but the low mean free path of photoelectrons limits the electrolyte film thickness in the analyzed area to a few nanometers. This limitation can introduce mass-transfer issues and a significant potential drop such that the actual electrochemical potential at the point measured with AP-XPS might not be the true electrochemical potential applied with the potentiostat. As a result, we adopted a dip-and-pull approach where the sample was first exposed to the electrochemical environment and then studied in ~13 mbar water vapor, which was sufficient to keep the electrolyte layer stable on the electrode surface. This *in situ* approach allowed also to mitigate beam-induced effects and was useful for a quantitative and detailed analysis of the chemical species at the surface, but it simply cannot catch the dynamic transformations taking place during reaction and under potential sweeps.

To address this gap, we employed RefleXAFS to monitor the chemical environment at the surface of model electrodes during static and dynamic electrochemical polarization. RefleXAFS was first developed in the 1980s, but it remains underexplored for these types of applications, especially with more recent and powerful X-ray sources like 4th generation synchrotrons. The experiment consists of measuring the totally reflected beam as a function of the incident beam energy. This is a hard X-ray technique based on a photon-in photon-out process, therefore the limitations posed by electrolyte attenuation can be more easily mitigated. Adopting a total-reflection geometry is crucial to achieve a comparable surface sensitivity to AP-XPS. By leveraging the capabilities of a 4th generation synchrotron and the recent technological advances in beamline instrumentation and spectro-electrochemical cells design, we achieved an unprecedented signal-to-noise ratio, enabling us to detect sub-nanoscale (hydr)oxides with beam energies as low as 8 keV and spectral acquisition rates as low as 1 Hz. Further advancement in this direction can be achieved by e.g. designing electrochemical cells that reduce the path of the beam through the electrolyte, hence reducing the attenuation of the beam. Otherwise, an alternative to RefleXAFS for low-Z elements with low absorption-edge energies is grazing-incidence total-scattering measurements, but this needs to be further explored. Quantitative analysis of RefleXAFS data is less trivial compared to other well-developed methods, but combining RefleXAFS with other techniques, such as 2D-SOR and AP-XPS, is a powerful approach to tackle this problem and gain additional insights. Performing multimodal studies was indeed necessary to gain a comprehensive understanding of these electrochemical processes.

I believe that these experimental methods and multimodal studies can help to increase our fundamental understanding of electrochemical interfacial processes. Furthermore, these insights can contribute to the development of more efficient and cost-effective electrocatalysts for green technologies, such as electrolyzers and fuel cells, as well as to the development of better corrosion-resistant materials. Moreover, these approaches have the potential to be expanded to other relevant material systems and research fields in electrochemistry, important for the progress towards a more sustainable society.

References

(1) Bard, A. J.; Faulkner, L. R.; White, H. S. Electrochemical Methods: Fundamentals and Applications; *John Wiley & Sons*, **2022,** ISBN 9781118312803.

(2) Chu, S.; Majumdar, A. Opportunities and Challenges for a Sustainable Energy Future. *Nature* **2012**, *488* (7411), 294–303.

(3) Seh, Z. W.; Kibsgaard, J.; Dickens, C. F.; Chorkendorff, I.; Nørskov, J. K.; Jaramillo, T. F. Combining Theory and Experiment in Electrocatalysis: Insights into Materials Design. *Science* **2017**, *355* (6321), eaad4998.

(4) Wang, S.; Lu, A.; Zhong, C.-J. Hydrogen Production from Water Electrolysis: Role of Catalysts. *Nano Converg.* **2021**, *8* (1), 4.

(5) Jiao, K.; Xuan, J.; Du, Q.; Bao, Z.; Xie, B.; Wang, B.; Zhao, Y.; Fan, L.; Wang, H.; Hou, Z.; Huo, S.; Brandon, N. P.; Yin, Y.; Guiver, M. D. Designing the next Generation of Proton-Exchange Membrane Fuel Cells. *Nature* **2021**, *595* (7867), 361–369.

(6) Escudero-Escribano, M.; Malacrida, P.; Hansen, M. H.; Vej-Hansen, U. G.; Velázquez-Palenzuela, A.; Tripkovic, V.; Schiøtz, J.; Rossmeisl, J.; Stephens, I. E. L.; Chorkendorff, I. Tuning the Activity of Pt Alloy Electrocatalysts by Means of the Lanthanide Contraction. *Science* **2016**, *352* (6281), 73–76.

(7) Wang, H.; Yan, Z.; Cheng, F.; Chen, J. Advances in Noble Metal Electrocatalysts for Acidic Oxygen Evolution Reaction: Construction of Under-Coordinated Active Sites. *Adv. Sci.* **2024**, *11* (32), 2401652.

(8) Rong, C.; Dastafkan, K.; Wang, Y.; Zhao, C. Breaking the Activity and Stability Bottlenecks of Electrocatalysts for Oxygen Evolution Reactions in Acids. *Adv. Mater.* **2023**, *35* (49), 2211884.

(9) Over, H. Fundamental Studies of Planar Single-Crystalline Oxide Model Electrodes (RuO2, IrO2) for Acidic Water Splitting. *ACS Catal.* **2021**, *11* (14), 8848–8871.

(10) Cherevko, S.; Keeley, G. P.; Geiger, S.; Zeradjanin, A. R.; Hodnik, N.; Kulyk, N.; Mayrhofer, K. J. J. Dissolution of Platinum in the Operational Range of Fuel Cells. *ChemElectroChem* **2015**, *2* (10), 1471–1478.

(11) Cherevko, S.; Topalov, A. A.; Zeradjanin, A. R.; Katsounaros, I.; Mayrhofer, K. J. J. Gold Dissolution: Towards Understanding of Noble Metal Corrosion. *RSC Adv.* **2013**, *3* (37), 16516–16527.

(12) Conway, B. E. Electrochemical Oxide Film Formation at Noble Metals as a Surface-Chemical Process. *Prog. Surf. Sci.* **1995**, *49* (4), 331–452.

(13) Hultman, L.; Mazur, S.; Ankarcrona, C.; Palmqvist, A.; Abrahamsson, M.; Antti, M.-L.; Baltzar, M.; Bergström, L.; de Laval, P.; Edman, L.; Erhart, P.; Kloo, L.; Lundberg, M. W.; Mikkelsen, A.; Moons, E.; Persson, C.; Rensmo, H.; Rosén, J.; Rudén, C.; Selleby, M.; Sundgren, J.-E.; Dick Thelander, K.; Tybrandt, K.; Weihed, P.; Zou, X.; Åstrand, M.; Björkman, C. P.; Schneider, J. M.; Eriksson, O.; Berggren, M. Advanced Materials Provide Solutions towards a Sustainable World. *Nat. Mater.* **2024**, *23* (2), 160–161.
(14) Magnussen, O. M.; Groß, A. Toward an Atomic-Scale Understanding of Electrochemical Interface Structure and Dynamics. *J. Am. Chem. Soc.* **2019**, *141* (12), 4777–4790.
(15) Fernández-Vidal, J.; Koper, M. T. M. The Role of Surface Science in Electrocatalysis. *ACS Catal.* **2026**, *16* (4), 2925–2934.
(16) Zhang, W.; Paolella, A.; Titirici, M.-M.; Tsuchiya, T. Advanced Architectures of Electrochemical Interfaces. *Commun. Chem.* **2025**, *8* (1), 235.
(17) Pastor, E.; Lian, Z.; Xia, L.; Ecija, D.; Galán-Mascarós, J. R.; Barja, S.; Giménez, S.; Arbiol, J.; López, N.; García de Arquer, F. P. Complementary Probes for the Electrochemical Interface. *Nat. Rev. Chem.* **2024**, *8* (3), 159–178.
(18) Magnussen, O. M.; Drnec, J.; Qiu, C.; Martens, I.; Huang, J. J.; Chattot, R.; Singer, A. In Situ and Operando X-Ray Scattering Methods in Electrochemistry and Electrocatalysis. *Chem. Rev.* **2024**, *124* (3), 629–721.
(19) Lundgren, E.; Zhang, C.; Merte, L. R.; Shipilin, M.; Blomberg, S.; Hejral, U.; Zhou, J.; Zetterberg, J.; Gustafson, J. Novel in Situ Techniques for Studies of Model Catalysts. *Acc. Chem. Res.* **2017**, *50* (9), 2326–2333.
(20) Magnussen, O. M. The Rise of Electrochemical Surface Science: From *in Situ* Interface Structure to Operando Dynamics. *Surf. Sci.* **2024**, *749*, 122574.
(21) Briega-Martos, V.; Yang, Y. Single-Crystal Metals and Oxides as Atomically Precise Energy Materials Platforms for Fundamental Electrocatalysis. *Acc. Mater. Res.* **2024**, *5* (5), 518–522.
(22) Auer, A.; Giessibl, F. J.; Kunze-Liebhäuser, J. Combining Electrochemical Scanning Tunneling Microscopy with Force Microscopy. *ACS Nano* **2025**, *19* (9), 8401–8410.
(23) d'Acapito, F.; Emelianov, I.; Relini, A.; Cavatorta, P.; Gliozzi, A.; Minicozzi, V.; Morante, S.; Solari, P. L.; Rolandi, R. Total External Reflection X-Ray Absorption Spectroscopy Reveals a Zinc Coordination Shell in Phospholipid Langmuir−Blodgett Films. *Langmuir* **2002**, *18* (13), 5277–5282.
(24) Lützenkirchen-Hecht, D.; Stötzel, J.; Just, J.; Müller, O.; Bornmann, B.; Frahm, R. Time-Resolved Grazing Incidence X-Ray Absorption Spectroscopy for the In Situ Investigation of the Initial Stages of Sputter-Deposited Copper Thin Films. *Phys. Status Solidi A* **2022**, *219* (9), 2100514.
(25) Kawai, J.; Hayakawa, S.; Kitajima, Y.; Gohshi, Y. X–Ray Absorption Fine Structure (XAFS) of Si Wafer Measured Using Total Reflection X–Rays. *Spectrochim. Acta Part B At. Spectrosc.* **1999**, *54* (1), 215–222.

(26) Abe, H.; Niwa, Y.; Takeichi, Y.; Kimura, M. In Situ TREXS Observation of Surface Reduction Reaction of NiO Film with ∼2 Nm Surface Sensitivity. *Chem. Rec.* **2019**, *19* (7), 1457–1461.
(27) Martens, G.; Rabe, P. EXAFS Studies on Superficial Regions by Means of Total Reflection. *Phys. Status Solidi A* **1980**, *58* (2), 415–424.
(28) Martens, G.; Rabe, P. EXAFS of a Thin Film of Cu Measured by Total Reflection. *Phys. Status Solidi A* **1980**, *57* (1), K31–K34.
(29) Hecht, D.; Borthen, P.; Strehblow, H.-H. In Situ Examination of Anodic Silver Oxide Films by EXAFS in the Reflection Mode. *J. Electroanal. Chem.* **1995**, *381* (1–2), 113–121.
(30) Eriksson, M.; Veen, J. F. van der; Quitmann, C. Diffraction-Limited Storage Rings – a Window to the Science of Tomorrow. *J. Synchrotron Radiat.* **2014**, *21* (5), 837–842.
(31) Foresti, M. L.; Pozzi, A.; Innocenti, M.; Pezzatini, G.; Loglio, F.; Salvietti, E.; Giusti, A.; D'Anca, F.; Felici, R.; Borgatti, F. In Situ X-Ray Analysis under Controlled Potential Conditions: An Innovative Setup and Its Application to the Investigation of Ultrathin Films Electrodeposited on Ag(111). *Electrochimica Acta* **2006**, *51* (25), 5532–5539.
(32) Oxtoby, D. W.; Gillis, H. P.; Butler, L. J. Principles of Modern Chemistry; *Cengage Learning*, **2016**, ISBN 1305079116.
(33) Kittel, C. Introduction to Solid State Physics, 8. ed.; *John Wiley & Sons*, 20, **2004**, ISBN: 978-0-471-41526-8.
(34) Marcus, P.; Maurice, V. Passivation of Metals and Semiconductors, and Properties of Thin Oxide Layers; *Elsevier*, **2006**, ISBN: 978-0-444-52224-5.
(35) Crick, C. R.; Parkin, I. P. Preparation and Characterisation of Super-Hydrophobic Surfaces. *Chem. – Eur. J.* **2010**, *16* (12), 3568–3588.
(36) Xue, J.; Yin, X.; Xue, L.; Zhang, C.; Dong, S.; Yang, L.; Fang, Y.; Li, Y.; Li, L.; Cui, J. Self-Growing Photonic Composites with Programmable Colors and Mechanical Properties. *Nat. Commun.* **2022**, *13* (1), 7823.
(37) Aliofkhazraei, M.; Walsh, F. C.; Zangari, G.; Köçkar, H.; Alper, M.; Rizal, C.; Magagnin, L.; Protsenko, V.; Arunachalam, R.; Rezvanian, A.; Moein, A.; Assareh, S.; Allahyarzadeh, M. H. Development of Electrodeposited Multilayer Coatings: A Review of Fabrication, Microstructure, Properties and Applications. *Appl. Surf. Sci. Adv.* **2021**, *6*, 100141.
(38) Han, T.; Cao, W.; Xu, Z.; Adibnia, V.; Olgiati, M.; Valtiner, M.; Ma, L.; Zhang, C.; Ma, M.; Luo, J.; Banquy, X. Hydration Layer Structure Modulates Superlubrication by Trivalent La3+ Electrolytes. *Sci. Adv.* **2023**, *9* (28), eadf3902.
(39) van der Vliet, D. F.; Wang, C.; Tripkovic, D.; Strmcnik, D.; Zhang, X. F.; Debe, M. K.; Atanasoski, R. T.; Markovic, N. M.; Stamenkovic, V. R. Mesostructured Thin Films as Electrocatalysts with Tunable Composition and Surface Morphology. *Nat. Mater.* **2012**, *11* (12), 1051–1058.
(40) Munger, C. G. Corrosion Prevention by Protective Coatings; *National Association of Corrosion Engineers,* **1985**, ISBN: 978-0915567041.

(41) Shan, J.; Zheng, Y.; Shi, B.; Davey, K.; Qiao, S.-Z. Regulating Electrocatalysts via Surface and Interface Engineering for Acidic Water Electrooxidation. *ACS Energy Lett.* **2019**, *4* (11), 2719–2730.
(42) Ibach, H. Physics of Surfaces and Interfaces; *Springer*, **2006**, ISBN: 978-3-540-34710-1.
(43) Kepler, J. The Six-Cornered Snowflake; *Paul Dry Books*, **2010**, ISBN: 978-1589880535.
(44) Hales, T. A Proof of the Kepler Conjecture. *Ann. Math.* **2005**, *162* (3), 1065–1185.
(45) Groß, A. Theoretical Surface Science: A Microscopic Perspective; Advanced Texts in Physics; *Springer*, **2003**, ISBN: 978-3-662-05041-5.
(46) Li, P.; Ding, F. Origin of the Herringbone Reconstruction of Au(111) Surface at the Atomic Scale. *Sci. Adv.* **2022**, *8* (40), eabq2900.
(47) Momma, K.; Izumi, F. VESTA: A Three-Dimensional Visualization System for Electronic and Structural Analysis. *J. Appl. Crystallogr.* **2008**, *41*, 653–658.
(48) Lundgren, E.; Gustafson, J.; Resta, A.; Weissenrieder, J.; Mikkelsen, A.; Andersen, J. N.; Köhler, L.; Kresse, G.; Klikovits, J.; Biederman, A.; Schmid, M.; Varga, P. The Surface Oxide as a Source of Oxygen on Rh(111). *J. Electron Spectrosc. Relat. Phenom.* **2005**, *144–147*, 367–372.
(49) Lundgren, E.; Kresse, G.; Klein, C.; Borg, M.; Andersen, J. N.; De Santis, M.; Gauthier, Y.; Konvicka, C.; Schmid, M.; Varga, P. Two-Dimensional Oxide on Pd(111). *Phys. Rev. Lett.* **2002**, *88* (24), 246103.
(50) Klikovits, J.; Schmid, M.; Gustafson, J.; Mikkelsen, A.; Resta, A.; Lundgren, E.; Andersen, J. N.; Varga, P. Kinetics of the Reduction of the Rh(111) Surface Oxide: Linking Spectroscopy and Atomic-Scale Information. *J. Phys. Chem. B* **2006**, *110* (20), 9966–9975.
(51) Fuchs, T. In Situ X-Ray Scattering Studies of the Electrooxidation of Platinum Single Crystal Electrodes, PhD Thesis, *Christian-Albrechts-Universität zu Kiel*, **2024,** URN: urn:nbn:de:gbv:8:3-2024-00918-1.
(52) Cabrera, N.; Mott, N. F. Theory of the Oxidation of Metals. *Rep. Prog. Phys.* **1949**, *12* (1), 163.
(53) Fehlner, F. P.; Mott, N. F. Low-Temperature Oxidation. *Oxid. Met.* **1970**, *2* (1), 59–99.
(54) Ramírez, L. P.; Bournel, F.; Gallet, J.-J.; Dudy, L.; Rochet, F. Testing the Cabrera–Mott Oxidation Model for Aluminum under Realistic Conditions with Near-Ambient Pressure Photoemission. *J. Phys. Chem. C* **2022**, *126* (5), 2517–2530.
(55) Larsson, A.; Gericke, S.; Grespi, A.; Koller, V.; Eidhagen, J.; Yue, X.; Frampton, E.; Appelfeller, S.; Generalov, A.; Preobrajenski, A.; Pan, J.; Over, H.; Lundgren, E. Dynamics of Early-Stage Oxide Formation on a Ni-Cr-Mo Alloy. *Npj Mater. Degrad.* **2024**, *8* (1), 39.
(56) Lundgren, E.; Gustafson, J.; Mikkelsen, A.; Andersen, J. N.; Stierle, A.; Dosch, H.; Todorova, M.; Rogal, J.; Reuter, K.; Scheffler, M. Kinetic

Hindrance during the Initial Oxidation of Pd(100) at Ambient Pressures. *Phys. Rev. Lett.* **2004**, *92* (4), 046101.
(57) Evertsson, J.; Bertram, F.; Zhang, F.; Rullik, L.; Merte, L. R.; Shipilin, M.; Soldemo, M.; Ahmadi, S.; Vinogradov, N.; Carlà, F.; Weissenrieder, J.; Göthelid, M.; Pan, J.; Mikkelsen, A.; Nilsson, J.-O.; Lundgren, E. The Thickness of Native Oxides on Aluminum Alloys and Single Crystals. *Appl. Surf. Sci.* **2015**, *349*, 826–832.
(58) Baran, J. D.; Grönbeck, H.; Hellman, A. Mechanism for Limiting Thickness of Thin Oxide Films on Aluminum. *Phys. Rev. Lett.* **2014**, *112* (14), 146103.
(59) Hammer, B.; Norskov, J. K. Why Gold Is the Noblest of All the Metals. *Nature* **1995**, *376* (6537), 238–240.
(60) Rodriguez, P.; Koper, M. T. M. Electrocatalysis on Gold. *Phys. Chem. Chem. Phys.* **2014**, *16* (27), 13583–13594.
(61) Gonçalves, J.; Kumar, A.; Da Silva, M.; Toma, H.; Martins, P.; Araki, K.; Bertotti, M.; Angnes, L. Nanoporous Gold-Based Materials for Electrochemical Energy Storage and Conversion. *Energy Technol.* **2021**, *9*.
(62) Rodriguez, P.; Plana, D.; Fermin, D. J.; Koper, M. T. M. New Insights into the Catalytic Activity of Gold Nanoparticles for CO Oxidation in Electrochemical Media. *J. Catal.* **2014**, *311*, 182–189.
(63) Graf, M.; Haensch, M.; Carstens, J.; Wittstock, G.; Weissmüller, J. Electrocatalytic Methanol Oxidation with Nanoporous Gold: Microstructure and Selectivity. *Nanoscale* **2017**, *9* (45), 17839–17848.
(64) Pasta, M.; La Mantia, F.; Cui, Y. Mechanism of Glucose Electrochemical Oxidation on Gold Surface. *Electrochimica Acta* **2010**, *55* (20), 5561–5568.
(65) Xie, X.; Briega-Martos, V.; Alemany, P.; Mohandas Sandhya, A. L.; Skála, T.; Rodríguez, M. G.; Nováková, J.; Dopita, M.; Vorochta, M.; Bruix, A.; Cherevko, S.; Neyman, K. M.; Matolínová, I.; Khalakhan, I. Balancing Activity and Stability through Compositional Engineering of Ternary PtNi–Au Alloy ORR Catalysts. *ACS Catal.* **2025**, *15* (1), 234–245.
(66) Wang, D.; Liu, S.; Wang, J.; Lin, R.; Kawasaki, M.; Rus, E.; Silberstein, K. E.; Lowe, M. A.; Lin, F.; Nordlund, D.; Liu, H.; Muller, D. A.; Xin, H. L.; Abruña, H. D. Spontaneous Incorporation of Gold in Palladium-Based Ternary Nanoparticles Makes Durable Electrocatalysts for Oxygen Reduction Reaction. *Nat. Commun.* **2016**, *7* (1), 11941.
(67) Li, C.-Y.; Dong, J.-C.; Jin, X.; Chen, S.; Panneerselvam, R.; Rudnev, A. V.; Yang, Z.-L.; Li, J.-F.; Wandlowski, T.; Tian, Z.-Q. In Situ Monitoring of Electrooxidation Processes at Gold Single Crystal Surfaces Using Shell-Isolated Nanoparticle-Enhanced Raman Spectroscopy. *J. Am. Chem. Soc.* **2015**, *137* (24), 7648–7651.
(68) Hamelin, A. Cyclic Voltammetry at Gold Single-Crystal Surfaces. Part 1. Behaviour at Low-Index Faces. *J. Electroanal. Chem.* **1996**, *407* (1), 1–11.
(69) Magnussen, O. M. Ordered Anion Adlayers on Metal Electrode Surfaces. *Chem. Rev.* **2002**, *102* (3), 679–726.

(70) Stojanovski, K.; Briega-Martos, V.; Zlatar, M.; Göllner, C.; Cherevko, S. pH Dependence of Noble Metals Dissolution: Gold. *ChemElectroChem* **2024**, *11* (18), e202400373.
(71) Diaz-Morales, O.; Calle-Vallejo, F.; Munck, C. de; Koper, M. T. M. Electrochemical Water Splitting by Gold: Evidence for an Oxide Decomposition Mechanism. *Chem. Sci.* **2013**, *4* (6), 2334–2343.
(72) Yang, S.; Hetterscheid, D. G. H. Redefinition of the Active Species and the Mechanism of the Oxygen Evolution Reaction on Gold Oxide. *ACS Catal.* **2020**, *10* (21), 12582–12589.
(73) Redondo, J.; Etxebarria, A.; Samal, P. K.; Albons, L.; Climent, R. F.; Auras, S.; Šmíd, B.; Ju, X.; Matvija, P.; Schiller, F.; Setvín, M.; Mysliveček, J.; Barja, S. Direct Experimental Evidence of Transient Auδ+ Oxide in Au Electrooxidation. *J. Am. Chem. Soc.* **2026**.
(74) Chico-Mesa, L.; Rodes, A.; Arán-Ais, R. M.; Herrero, E. Insights into Catalytic Activity and Selectivity of 5-Hydroxymethylfurfural Oxidation on Gold Single-Crystal Electrodes. *Nat. Commun.* **2025**, *16* (1), 3349.
(75) Kwon, Y.; Lai, S. C. S.; Rodriguez, P.; Koper, M. T. M. Electrocatalytic Oxidation of Alcohols on Gold in Alkaline Media: Base or Gold Catalysis? *J. Am. Chem. Soc.* **2011**, *133* (18), 6914–6917.
(76) Materials Data on HAuO2 by Materials Project; mp-996998; *LBNL Materials Project*; Lawrence Berkeley National Laboratory (LBNL), Berkeley, CA (United States), **2020**.
(77) Materials Data on Au2O3 by Materials Project; mp-27253; *LBNL Materials Project*; Lawrence Berkeley National Laboratory (LBNL), Berkeley, CA (United States), **2020**.
(78) Shi, H.; Asahi, R.; Stampfl, C. Properties of the Gold Oxides Au2O3 and Au2O: First-Principles Investigation. *Phys. Rev. B* **2007**, *75* (20), 205125.
(79) Weiher, N.; Willneff, E. A.; Figulla-Kroschel, C.; Jansen, M.; Schroeder, S. L. M. Extended X-Ray Absorption Fine-Structure (EXAFS) of a Complex Oxide Structure: A Full Multiple Scattering Analysis of the Au L3-Edge EXAFS of Au2O3. *Solid State Commun.* **2003**, *125* (6), 317–322.
(80) Xia, S. J.; Birss, V. I. A Multi-Technique Study of Compact and Hydrous Au Oxide Growth in 0.1 M Sulfuric Acid Solutions. *J. Electroanal. Chem.* **2001**, *500* (1), 562–573.
(81) Burke, L. D.; Nugent, P. F. The Electrochemistry of Gold: I the Redox Behaviour of the Metal in Aqueous Media. *Gold Bull.* **1997**, *30* (2), 43–53.
(82) Kawamoto, D.; Ando, H.; Ohashi, H.; Kobayashi, Y.; Honma, T.; Ishida, T.; Tokunaga, M.; Okaue, Y.; Utsunomiya, S.; Yokoyama, T. Structure of a Gold(III) Hydroxide and Determination of Its Solubility. *Bull. Chem. Soc. Jpn.* **2016**, *89* (11), 1385–1390.
(83) Griesser, C.; Winkler, D.; Moser, T.; Haug, L.; Thaler, M.; Portenkirchner, E.; Klötzer, B.; Diaz-Coello, S.; Pastor, E.; Kunze-Liebhäuser, J. Lab-Based Electrochemical X-Ray Photoelectron Spectroscopy for in-Situ Probing of Redox Processes at the Electrified Solid/Liquid Interface. *Electrochem. Sci. Adv.* **2024**, *4* (3), e2300007.

(84) Rocchigiani, L. and Bochmann M. Recent Advances in Gold(III) Chemistry: Structure, Bonding, Reactivity, and Role in Homogeneous Catalysis. *Chemical Reviews*. **2021,** *121* (14), 8364-8451.
(85) Gänzler, A. M.; Casapu, M.; Vernoux, P.; Loridant, S.; Cadete Santos Aires, F. J.; Epicier, T.; Betz, B.; Hoyer, R.; Grunwaldt, J.-D. Tuning the Structure of Platinum Particles on Ceria In Situ for Enhancing the Catalytic Performance of Exhaust Gas Catalysts. *Angew. Chem. Int. Ed.* **2017**, *56* (42), 13078–13082.
(86) Somorjai, G. A. The Surface Structure of and Catalysis by Platinum Single Crystal Surfaces. *Catal. Rev.* **1972**, *7* (1), 87–120.
(87) Fairhurst, A. R.; Lim, C.; Jun, M.; Ransom, B. J.; Mackowicz, F.; Haering, D.; Stamenkovic, V. R. Surface Science: The Foundation of Electrocatalysis. *J. Am. Chem. Soc.* **2025**, *147* (44), 40035–40044.
(88) Hansen, J. N.; Prats, H.; Toudahl, K. K.; Mørch Secher, N.; Chan, K.; Kibsgaard, J.; Chorkendorff, I. Is There Anything Better than Pt for HER? *ACS Energy Lett.* **2021**, *6* (4), 1175–1180.
(89) Galloni, E. E.; Busch, R. H. The Structure of Platinum Oxides. *J. Chem. Phys.* **1952**, *20* (1), 198–199.
(90) Seriani, N.; Jin, Z.; Pompe, W.; Ciacchi, L. C. Density Functional Theory Study of Platinum Oxides: From Infinite Crystals to Nanoscopic Particles. *Phys. Rev. B* **2007**, *76* (15), 155421.
(91) Materials Data on PtO2 by Materials Project; mp-1285; *LBNL Materials Project*; Lawrence Berkeley National Laboratory (LBNL), Berkeley, CA (United States), **2020**.
(92) Materials Data on PtO by Materials Project; mp-7947; *LBNL Materials Project*; Lawrence Berkeley National Laboratory (LBNL), Berkeley, CA (United States), **2020**.
(93) Darolia, R. Development of Strong, Oxidation and Corrosion Resistant Nickel-Based Superalloys: Critical Review of Challenges, Progress and Prospects. *Int. Mater. Rev.* **2019**, *64* (6), 355–380.
(94) Klapper, H. S.; Zadorozne, N. S.; Rebak, R. B. Localized Corrosion Characteristics of Nickel Alloys: A Review. *Acta Metall. Sin. Engl. Lett.* **2017**, *30* (4), 296–305.
(95) Patel, N. S.; Pavlík, V.; Boča, M. High-Temperature Corrosion Behavior of Superalloys in Molten Salts – A Review. *Crit. Rev. Solid State Mater. Sci.* **2017**, *42* (1), 83–97.
(96) Materials Data on NiO by Materials Project; mp-19009; *LBNL Materials Project*; Lawrence Berkeley National Laboratory (LBNL), Berkeley, CA (United States), **2017**.
(97) Materials Data on Ni(OH)2 by Materials Project; (Mp-27912) *LBNL Materials Project*; Lawrence Berkeley National Laboratory (LBNL), Berkeley, CA (United States), **2013**.
(98) Materials Data on Cr2O3 by Materials Project; mp-19399; *LBNL Materials Project*; Lawrence Berkeley National Laboratory (LBNL), Berkeley, CA (United States), **2020**.

(99) Materials Data on MoO2 by Materials Project; mp-510536; *LBNL Materials Project*; Lawrence Berkeley National Laboratory (LBNL), Berkeley, CA (United States), **2020**.
(100) Materials Data on MoO3 by Materials Project; mp-18856; *LBNL Materials Project*; Lawrence Berkeley National Laboratory (LBNL), Berkeley, CA (United States), **2020**.
(101) Compton, R.; Banks, C. Understanding Voltammetry; *World Scientific,* **2018**, ISBN: 978-1-78634-528-8.
(102) Zoski, C. G. Handbook of Electrochemistry; *Elsevier*, **2007**, ISBN: 9780080469300.
(103) Ragone, D. V. Thermodynamics of Materials; *Wiley*, **1995**, ISBN: 978-88-08-08663-1.
(104) Pedeferri, P. Corrosion Science and Engineering; Engineering materials, *Springer*, **2018**, ISBN: 9783319976259.
(105) Marcus, R. On the Theory of Oxidation-Reduction Reactions Involving Electron Transfer. I. *J. Chem. Phys.* **1956**, *24*, 966–978.
(106) Marcus, R. Chemical and Electrochemical Electron-Transfer Theory. *Annu Rev Phys Chem* **2003**, *15*, 155–196.
(107) Kodama, T.; Gokon, N. Thermochemical Cycles for High-Temperature Solar Hydrogen Production. *Chem. Rev.* **2007**, *107* (10), 4048–4077.
(108) Parsons, R. Atlas of Electrochemical Equilibria in Aqueous Solutions. *J. Electroanal. Chem. Interfacial Electrochem.* **1967**, *13* (4), 471.
(109) Chen, D.; Zhou, W.; Ji, Y.; Dong, C. Applications of Density Functional Theory to Corrosion and Corrosion Prevention of Metals: A Review. *Mater. Genome Eng. Adv.* **2025**, *3* (1), e83.
(110) Tem5psu. PourbaixWater.Png. *Wikimedia Commons*. **2017**.
(111) Suen, N.-T.; Hung, S.-F.; Quan, Q.; Zhang, N.; Xu, Y.-J.; Chen, H. M. Electrocatalysis for the Oxygen Evolution Reaction: Recent Development and Future Perspectives. *Chem. Soc. Rev.* **2017**, *46* (2), 337–365.
(112) Nørskov, J. K.; Bligaard, T.; Logadottir, A.; Kitchin, J. R.; Chen, J. G.; Pandelov, S.; Stimming, U. Trends in the Exchange Current for Hydrogen Evolution. *J. Electrochem. Soc.* **2005**, *152* (3), J23.
(113) Nørskov, J. K.; Bligaard, T.; Logadottir, A.; Bahn, S.; Hansen, L. B.; Bollinger, M.; Bengaard, H.; Hammer, B.; Sljivancanin, Z.; Mavrikakis, M.; Xu, Y.; Dahl, S.; Jacobsen, C. J. H. Universality in Heterogeneous Catalysis. *J. Catal.* **2002**, *209* (2), 275–278.
(114) Grimaud, A.; Diaz-Morales, O.; Han, B.; Hong, W. T.; Lee, Y.-L.; Giordano, L.; Stoerzinger, K. A.; Koper, M. T. M.; Shao-Horn, Y. Activating Lattice Oxygen Redox Reactions in Metal Oxides to Catalyse Oxygen Evolution. *Nat. Chem.* **2017**, *9* (5), 457–465.
(115) Nørskov, J. K.; Rossmeisl, J.; Logadottir, A.; Lindqvist, L.; Kitchin, J. R.; Bligaard, T.; Jónsson, H. Origin of the Overpotential for Oxygen Reduction at a Fuel-Cell Cathode. *J. Phys. Chem. B* **2004**, *108* (46), 17886–17892.

(116) Elgrishi, N.; Rountree, K. J.; McCarthy, B. D.; Rountree, E. S.; Eisenhart, T. T.; Dempsey, J. L. A Practical Beginner's Guide to Cyclic Voltammetry. *J. Chem. Educ.* **2018**, *95* (2), 197–206.
(117) Doña Rodríguez, J. M.; Herrera Melián, J. A.; Pérez Peña, J. Determination of the Real Surface Area of Pt Electrodes by Hydrogen Adsorption Using Cyclic Voltammetry. *J. Chem. Educ.* **2000**, *77* (9), 1195.
(118) Wu, Z.; Yang, G.; Zhang, Q.; Liu, Z.; Peng, F. Deciphering the High Overpotential of the Oxygen Reduction Reaction via Comprehensively Elucidating the Open Circuit Potential. *Energy Environ. Sci.* **2024**, *17* (10), 3338–3346.
(119) Macdonald, D. D. The Point Defect Model for the Passive State. *J. Electrochem. Soc.* **1992**, *139* (12), 3434.
(120) Seyeux, A.; Maurice, V.; Marcus, P. Oxide Film Growth Kinetics on Metals and Alloys: I. Physical Model. *J. Electrochem. Soc.* **2013**, *160* (6), C189.
(121) Inductiveload. EM Spectrum Properties Edit.Svg. *Wikimedia Commons*. **2007**.
(122) Als-Nielsen, J.; McMorrow, D. Elements of Modern X-Ray Physics. 2nd ed. *Wiley,* **2011**, ISBN: 978-1-119-99731-3
(123) XCOM: Photon Cross Sections Database. *NIST* **2009**.
(124) B.L. Henke, E.M. Gullikson, and J.C. Davis. X-Ray Interactions: Photoabsorption, Scattering, Transmission, and Reflection at E=50-30000 eV, Z=1-92, Atomic Data and Nuclear Data Tables Vol. 54 (No.2), 181-342. **1993**.
(125) Ilyin, D. TubeSpectrum-En.Svg. *Wikimedia Commons.* **2024**.
(126) Martensson, N.; Eriksson, M. The Saga of MAX IV, the First Multi-Bend Achromat Synchrotron Light Source. *Nucl. Instrum. Methods Phys. Res. Sect. Accel. Spectrometers Detect. Assoc. Equip.* **2018**, *907*, 97–104.
(127) Tavares, P. F.; Leemann, S. C.; Sjöström, M.; Andersson, Å. The MAX IV Storage Ring Project. *J. Synchrotron Radiat.* **2014**, *21* (5), 862–877.
(128) Tavares, P. F.; Al-Dmour, E.; Andersson, Å.; Cullinan, F.; Jensen, B. N.; Olsson, D.; Olsson, D. K.; Sjöström, M.; Tarawneh, H.; Thorin, S.; Vorozhtsov, A. Commissioning and First-Year Operational Results of the MAX IV 3 GeV Ring. *J. Synchrotron Radiat.* **2018**, *25* (5), 1291–1316.
(129) Balewski, K. Comissioning of PETRA III. *IPAC'10 - Proceedings*, **2010**.
(130) Drube, W.; Bieler, M.; Caliebe, W. A.; Schulte-Schrepping, H.; Spengler, J.; Tischer, M.; Wanzenberg, R. The PETRA III Extension. *AIP Conf. Proc.* **2016**, *1741* (1), 020035.
(131) Klementiev, K.; Norén, K.; Carlson, S.; Clauss, K. G. V. S.; Persson, I. The BALDER Beamline at the MAX IV Laboratory. *J. Phys. Conf. Ser.* **2016**, *712* (1), 012023.
(132) Calvin, S. XAFS for Everyone; *CRC Press*, **2013**, ISBN: 978-1-4398-7863-7
(133) Atenderholt. XASEdges.Svg. *Wikimedia Commons.* **2009**.
(134) Magnard, N. P. L.; Abbondanza, G.; Junkers, L. S.; Glatthaar, L.; Grespi, A.; Spriewald Luciano, A.; Igoa Saldaña, F.; Dippel, A.-C.; Vinogradov, N.; Over, H.; Jensen, K. M. Ø.; Lundgren, E. In Situ Grazing Incidence X-Ray

Total Scattering Reveals the Effect of the “Two-Step” Method for the Anodization of Aluminum Surfaces. *ACS Appl. Mater. Interfaces* **2025**, *17* (33), 46887–46898.
(135) TU Wien, Atominstitut. X-Ray Penetration Depth Calculator.
(136) McMullan, D. Scanning Electron Microscopy 1928–1965. *Scanning* **1995**, *17* (3), 175–185.
(137) Süzer, Ş. XPS Investigation of X-Ray-Induced Reduction of Metal Ions. *Appl. Spectrosc.* **2000**, *54* (11), 1716–1718.
(138) Black, A. P.; Escudero, C.; Fauth, F.; Fehse, M.; Agostini, G.; Reynaud, M.; Houdeville, R. G.; Chatzogiannakis, D.; Orive, J.; Ramo-Irurre, A.; Casas-Cabanas, M.; Palacin, M. R. Beam Effects in Synchrotron Radiation *Operando* Characterization of Battery Materials: X-Ray Diffraction and Absorption Study of $LiNi_{0.33}$ $Mn_{0.33}$ $Co_{0.33}$ O_2 and $LiFePO_4$ Electrodes. *Chem. Mater.* **2024**, *36* (11), 5596–5610.
(139) Karslıoğlu, O.; Bluhm, H. Ambient-Pressure X-Ray Photoelectron Spectroscopy (APXPS). In Operando Research in Heterogeneous Catalysis; Frenken, J., Groot, I., Eds.; *Springer*, **2017**; pp 31–57, vol 114. ISBN: 978-3-319-44439-0.
(140) Einstein, A. Über Einen Die Erzeugung Und Verwandlung Des Lichtes Betreffenden Heuristischen Gesichtspunkt. *Ann. Phys.* **1905**, *322* (6), 132–148.
(141) Travnikova, O.; Borve, K. J.; Patanen, M.; Söderström, J.; Miron, C.; Saethre, L. J.; Mårtensson, N.; Svensson, S. The ESCA Molecule-Historical Remarks and New Results. *J. Electron Spectrosc. Relat. Phenom.* **2012**, *185* (8–9), 191–197.
(142) Larsson, A.; Simonov, K.; Eidhagen, J.; Grespi, A.; Yue, X.; Tang, H.; Delblanc, A.; Scardamaglia, M.; Shavorskiy, A.; Pan, J.; Lundgren, E. *In Situ* Quantitative Analysis of Electrochemical Oxide Film Development on Metal Surfaces Using Ambient Pressure X-Ray Photoelectron Spectroscopy: Industrial Alloys. *Appl. Surf. Sci.* **2023**, *611*, 155714.
(143) Zangwill, A. Physics at Surfaces; *Cambridge University Press*, **1988**, ISBN: 9780511622564.
(144) G. E-IMFP Universal-En.Svg. *Wikimedia Commons.* **2015**.
(145) Zhu, S.; Scardamaglia, M.; Kundsen, J.; Sankari, R.; Tarawneh, H.; Temperton, R.; Pickworth, L.; Cavalca, F.; Wang, C.; Tissot, H.; Weissenrieder, J.; Hagman, B.; Gustafson, J.; Kaya, S.; Lindgren, F.; Källquist, I.; Maibach, J.; Hahlin, M.; Boix, V.; Gallo, T.; Rehman, F.; D’Acunto, G.; Schnadt, J.; Shavorskiy, A. HIPPIE: A New Platform for Ambient-Pressure X-Ray Photoelectron Spectroscopy at the MAX IV Laboratory. *J. Synchrotron Radiat.* **2021**, *28* (2), 624–636.
(146) Jones, R.; Garcia-Martinez, F.; Wang, Y.; Rämisch, L.; Yaroslavtsev, A.; Scardamaglia, M.; Mehar, V.; Ghosalya, M. K.; Pfaff, S.; Gericke, S.; Ryder, C.; Küst, U. K.; Zareen, S.; Urpelainen, S.; O’Shea, J. N.; Zetterberg, J.; Knudsen, J.; Temperton, R. H.; Shavorskiy, A. Multimodal Ambient

Pressure Sample Environment for the HIPPIE Solid-Gas Endstation at MAX IV Laboratory. *Photon Sci.* **2026**. 1 (2), 111-120.
(147) Feidenhans'l, R. Surface Structure Determination by X-Ray Diffraction. *Surf. Sci. Rep.* **1989**, *10* (3), 105–188.
(148) Sjö, H.; Shabalin, A.; Lienert, U.; Hektor, J.; Schaefer, A.; Carlsson, P.-A.; Alwmark, C.; Gustafson, J. Surface Grain Orientation Mapping Using Grazing Incidence X-Ray Diffraction. *Surf. Sci.* **2025**, *754*, 122693.
(149) Onderwaater, W. G.; Taranovskyy, A.; Bremmer, G. M.; van Baarle, G. C.; Frenken, J. W. M.; Groot, I. M. N. From Dull to Shiny: A Novel Setup for Reflectance Difference Analysis under Catalytic Conditions. *Rev. Sci. Instrum.* **2017**, *88* (2), 023704.
(150) Schnaidt, J.; Beckord, S.; Engstfeld, A. K.; Klein, J.; Brimaud, S.; Behm, R. J. A Combined UHV-STM-Flow Cell Set-up for Electrochemical/Electrocatalytic Studies of Structurally Well-Defined UHV Prepared Model Electrodes. *Phys. Chem. Chem. Phys.* **2017**, *19* (6), 4166–4178.
(151) Binnig, G.; Rohrer, H. Scanning Tunneling Microscopy. *Surf. Sci.* **1983**, *126* (1), 236–244.
(152) Ponor. Low-Energy Electron Diffraction (LEED) Instrument – Schematic Diagram.svg. *Wikimedia Commons.* **2020**.
(153) Van Hove, M. A. (Michael A.). Low-Energy Electron Diffraction : Experiment, Theory, and Surface Structure Determination; *Springer-Verlag*, **1986**. ISBN: 978-3-642-82721-1.
(154) Acarlso3. AES Setup2-En.Svg. *Wikimedia Commons.* **2007**.

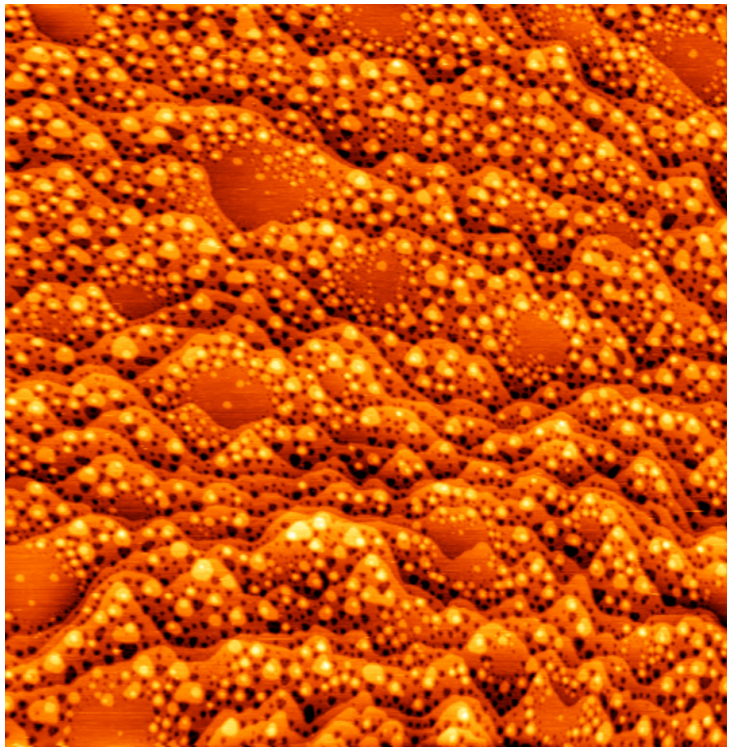

Printed by Media-Tryck, Lund 2026
NORDIC SWAN ECOLABEL 3041 0903

LUND UNIVERSITY

Department of Physics
Faculty of Science
Lund University
ISBN 978-91-8104-963-3